# ABSTRACT

Title of Dissertation: FORCED CONVECTIVE BOILING VIA INFRARED THERMOMETRY

Eric M Kommer, Doctor of Philosophy, 2013

Directed By: Professor Jungho Kim
Department of Mechanical Engineering

Multiphase heat transfer is an important mechanism across wide variety of engineering disciplines. The prediction of the heat transfer rate as a function of flow conditions and temperature has been based almost exclusively on experimentally derived correlations. The quality of these correlations depends on the accuracy and resolution of the measurement technique. In addition to the complexities of flow boiling phenomenon in earth gravity, engineering design of space systems requires knowledge of any gravity dependence for heat transfer characteristics.

Current research has shown significant variation in the heat transfer characteristics during pool boiling as a function of gravity magnitude. Research into flow boiling in variable gravity environments is extremely limited at this time, but necessary before multiphase systems can be designed for space.

The objective of this study is to develop, validate, and use a unique infrared thermometry method to quantify the heat transfer characteristics of flow boiling in earth gravity, prior to use of the apparatus in variable gravity environments. This new method allows high spatial and temporal resolution measurements, while simultaneously visualizing the flow phenomenon. Validation of this technique will be demonstrated by comparison to accepted correlations for single and multi-phase heat transfer in earth gravity environments.

# FORCED CONVECTIVE BOILING VIA INFRARED THERMOGRAPHY

by

Eric M Kommer

Dissertation submitted to the Faculty of the Graduate School of the
University of Maryland, College Park, in partial fulfillment
of the requirements for the degree of
Doctor of Philosophy
2013

Advisory Committee:

Professor Jungho Kim, Chair

Professor Marino di Marzo

Professor Gregory Jackson

Professor Kenneth Kiger

Professor Richard Calabrese (Dean's Representative)

# Table of Contents

# Index of Figures

# Index of Tables

# Nomenclature

| | | |
|---|---|---|
| Bo | - | boiling number |
| c | - | speed of light in vacuum (m/sec) |
| Co | - | convection number |
| $c_p$ | - | specific heat capacity (joules/kg-K) |
| e | - | Euler's number – natural logarithm base |
| E | - | radiative emissive power (W/m2) |
| F | - | band emission factor |
| $F_l$ | - | Kandlikar's fluid parameter |
| Fr | - | Froude number |
| h | - | heat transfer coefficient ($W/m^2K$) |
| hc | - | Plank's constant (joules – sec) |
| I | - | radiation intensity |
| k | - | thermal conductivity (W/m-K) |
| $k_b$ | - | Boltzmann's constant (joules/K) |
| L | - | length |
| n | - | real index of refraction |
| q | - | heat transfer rate (W) |
| q" | - | heat flux (w/m2) |
| $\dot{q}$ | - | heat generation rate (W/m3) |
| R | - | reflectivity |
| Re | - | Reynolds number |
| r | - | coordinate in the radial direction |
| t | - | time (seconds) |
| T | - | temperature (C or K) |
| x | - | quality |
| X | - | coordinate through the multilayer |
| $X_{tt}$ | - | Martinelli parameter |
| Y | - | coordinate across the multilayer |
| Z | - | coordinate along the length of the multilayer |
| | - | axial distance along the tube |
| $\alpha$ | - | optical absorption coefficient ($m^{-1}$) |
| $\varepsilon$ | - | emissivity of a surface |
| $\lambda$ | - | wavelength (microns) |
| $\rho$ | - | density ($kg/m^3$) |
| $\sigma$ | - | Stephan-Boltzmann constant ($W/m^2K^4$) |
| $\theta$ | - | angle |
| $\tau$ | - | transmissivity |

Subscripts

| | | |
|---|---|---|
| a | - | adhesive |
| c | - | camera |
| $\infty$ | - | infinity |

nb - nucleate boiling
s1 - surface 1
s2 - surface 2
sat - saturation
si - silicon
t - tape – polyimide + adhesive
0 - initial

# 1. Introduction

Multiphase heat transfer is an important engineering phenomenon across a wide variety of disciplines. The ability to transfer large amounts of energy through the change in phase of a fluid is important in everything from nuclear power cycles to the cooling of high power density micro electronics. Generally, boiling heat transfer can be separated into either pool or flow geometries. Flow boiling occurs when there is a bulk movement of fluid through the system, and is generally able to transfer much larger amounts of energy than stationary pool boiling assuming all other parameters are constant. It is for this reason that flow boiling is characteristically found in very high power engineering applications.

As solid state electronic devices become smaller and more powerful, the limiting design factor often becomes the maximum operating temperature. Consumer grade electronics are reaching energy densities today that surpass the heat transfer ability of passive thermal management. For high performance devices heat transfer via active means, whether forced convective or multiphase heat transfer, is needed today and in the future.

Because flow boiling heat transfer is a complicated phenomenon that is a function of many parameters, nearly all engineering designs are based on experimental correlations. Analytical or exact relationships for these phenomenon can only be acquired in the most simplified of cases. Generally, flow boiling research attempts to parameterize the heat transfer coefficient, $h$, as a function of fluid, system, and flow variables. For boiling in a simple circular pipe, $h$ could be a function of density, heat capacity, enthalpy of vaporization, thermal conductivity, velocity, diameter, length, gravity orientation, surface tension and viscosity. In addition, boiling processes are nonlinear with respect to most of these variables, and the physical phenomenon shift from one characteristic regime to another. To adequately develop experimental correlations, experimental data must be able to measure all of these variables with a high degree of spatial and temporal resolution, and ideally visualize the type of boiling regime occurring in the system.

A further complication to the already difficult task of predicting heat transfer performance of flow boiling occurs when the gravity force is removed or altered. In earth gravity, boiling phenomena depend on the buoyant force to remove the bubble and aid heat transfer. Boiling in zero gravity environments can have very different characteristics. As space systems use higher energy density components, there is a desire to use multiphase systems for cooling. Without accurate experimental data and correlations, design of zero gravity multiphase systems is not possible.

## 1.1 Objective

Because accurate engineering correlations depend on reliable experimental data, the objective of this research is to develop and validate a method to accurately measure parametric flow boiling data over a range of gravity values. Research to date as outlined in Section 2 has relied on point measurements to determine the heat transfer. Researchers focused on visualization of the boiling phenomena generally cannot accurately measure temperature and heat flux. In addition, the total number of researchers investigating flow boiling in zero gravity is very small, so this work serves to provide better quality data in an area that has been limited thus far.

The primary objectives of this work are to characterize the test apparatus, obtain reliable flow boiling data and evaluate against accepted correlations in earth gravity.

## 2. Literature Review

Forced convective flow boiling has been studied for over 50 years, primarily by mechanical engineers and chemical engineers. Pressurized water nuclear reactor design often depends on preventing or minimizing boiling in the fuel core region through a high degree of subcooling. Research started in the 1950's and ongoing today focuses on these heat transfer mechanisms, and especially determining the onset point of nucleate boiling and the critical heat flux point. Conversely, modern refrigeration system design depends on efficient phase change near saturation conditions with a minimum amount of subcooling and superheat. The proposed experimental technique will give insight into both of these design areas. Many researchers, e.g. Hewitt [1] have emphasized the importance of the flow regime on the heat transfer characteristics. Flow boiling is generally broken into separate regimes of nucleate, bubbly, slug, annular and dryout boiling corresponding to flow of increasing quality. Each of these regimes has separate experimental correlations associated to them and the transition from one to another is usually not well defined.

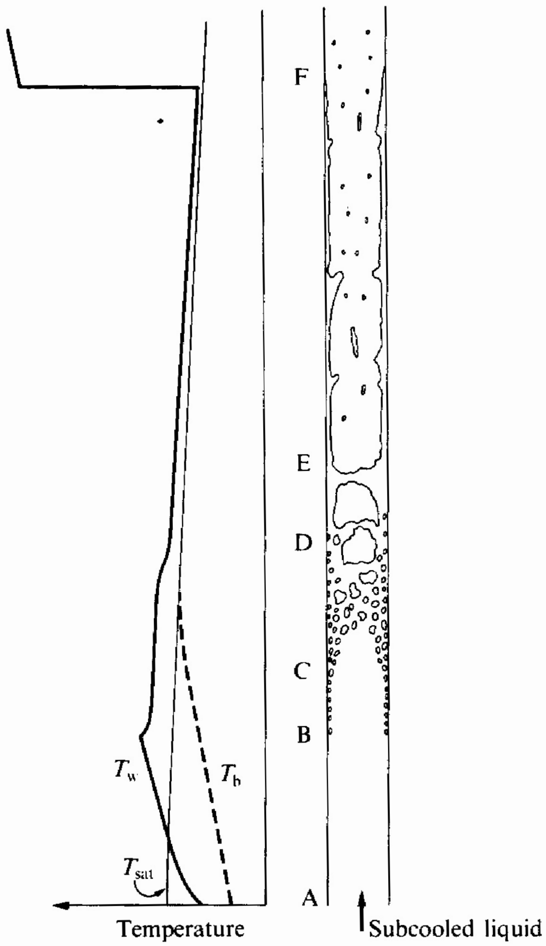

**Figure 2.1: Flow Boiling Regime Visualization. (From: Butterworth and Hewitt, "Two Phase Flow and Heat Transfer" [6])**

Nucleate boiling is observed at low vapor qualities (x < 0.1) and is often correlated using a combination of forced convection and boiling mechanisms. Rohsenhow [2] was the first to suggest calculating the total heat flux as a superposition of the single phase convection component and the two phase component, where

$$q''_{NB} = q''_{1phase} + q''_{2phase} \qquad [2.1]$$

Many researchers have utilized this simple idea and expanded it to fit experimental data [3, 4, 5, 20].

Determining the point of onset of nuclear boiling (ONB) is not as easy as determining where the fluid reaches the saturation temperature. Due to the nature of phase change, some degree of superheat is necessary even when the system is at saturation. Sato and Matsumura [4] suggest that ONB can be calculated assuming there are zero nucleation sites associated with a perfectly smooth surface using:

$$\Delta T = \frac{4\sigma T_{sat} v_{fg} h_f}{k_f h_{fg}} \left( 1 + \sqrt{1 + \frac{k_f h_{fg} \Delta T_{sub}}{2\sigma T_{sat} v_{fg} h_f}} \right) \qquad [2.2]$$

Kandlikar [5] and other researchers modified Sato's original relationship to determine ONB conditions for a variety of fluids and conditions.

A common representation of the flow boiling phenomenon is the boiling curve, shown in Figure 2.2 where the heat flux is plotted verses the wall superheat, $T_{wall}$-$T_{sat}$. The transition from forced convection to nucleate boiling is always at some wall temperature greater than the saturation temperature. The exact point where the boiling curve transitions from single phase to two phase is dependent upon the amount of subcooling, mass flow rate, number and size of nucleation sites, and the fluid parameters. Most expressions for prediction of ONB are derived by first determining the intersection of the forced convection (line 1-2) and fully developed boiling portions (line 3a-3b) of the curve. If the heat transfer characteristics are desired during transition to fully developed boiling, some type of interpolation is suggested[5, 6].

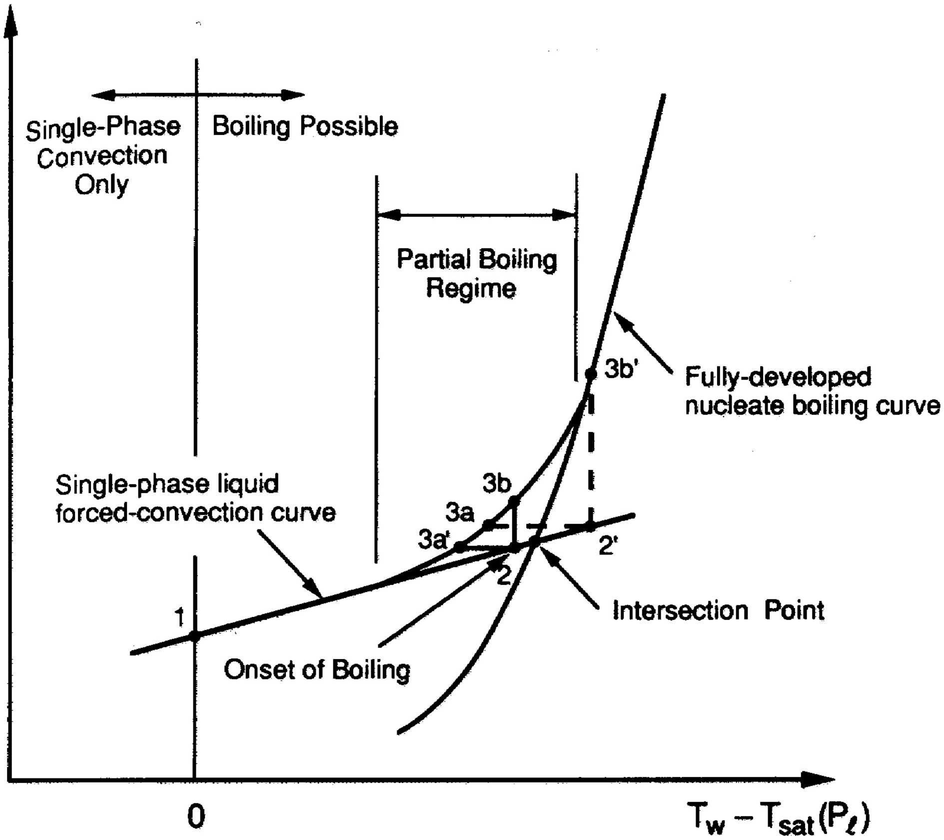

**Figure 2.2: Boiling Curve at Onset of Nucleate Boiling. (From: Van P Carey, "Liquid-Vapor Phase-Change Phenomena" [29])**

After the transition to fully developed nucleate boiling experimental curve fits can somewhat accurately predict heat transfer characteristics. One of the earliest correlations was recommended by Jenns and Lottes [3]

$$\Delta T_{wall} - T_{sat} = {0.022q''^{0.25}} \Big/ {\exp\left(\frac{P}{6.2}\right)} \qquad [2.3]$$

This relationship is valid only for water in upward vertical flow, but a more general form that is used by many researchers is

$$q'' = \gamma(T_w - T_{sat})^m \qquad [2.4]$$

where γ and m are chosen to fit experimental data based on fluid parameters [6, 7, 8]. Some early research neglected the effect of mass flow rate during fully developed boiling [3, 6], but more recent correlations include this variable [8, 9]. Correlations that include the effects of flow rate are normally a power law correlation of the form:

$$\mathrm{Nu} = \mathrm{C} \cdot \mathrm{Re}^{\mathrm{m}} \cdot \mathrm{Pr}^{\mathrm{n}} \qquad [2.5]$$

where m, n, and C are chosen to fit the experimental data. An example of a power law correlation is from Lazarek's work [30] using R-22 as a working fluid over mass and heat fluxes similar to those used in our study. Lazerak predicts the local Nusselt number using:

$$\mathrm{Nu} = 30\ \mathrm{Re}^{0.857}\mathrm{Bo}^{0.714} \qquad [2.6]$$

where the Boiling number, Bo, is:

$$\mathrm{Bo} = {q''}/{G\,h_{fg}} \qquad [2.7]$$

A second group of researchers use a superposition correlation, where the total heat transfer is a combination of the heat transfer due to the latent heat of vaporization, and that due to single phase convection. These correlations take the general form of:

$$h = C_1 h_{liquid} + C_2 h_{twophase} \tag{2.8}$$

The constants $C_1$ and $C_2$ can be simple or quite complicated, and $h_{twophase}$ is usually calculated using a forced convection correlations such as the Dittus-Boelter correlation. An example of a superposition correlation is that of Gungor [32]:

$$h = Eh_{liq} + Sh_{pool} \tag{2.9}$$

$$h_l = 0.023 Re_f^{0.8} Pr_f^{0.4} \frac{k_f}{d} \tag{2.10}$$

where:

$$E = 1 + 24000 Bo^{1.16} + 1.37 \left(\frac{1}{X_{tt}}\right)^{0.86} \tag{2.11}$$

$$S = \frac{1}{1 + 1.15 \times 10^{-6} E^2 Re_f^{1.17}} \tag{2.12}$$

and $h_{pool}$ is any applicable pool boiling correlation, Bo is the boiling number, and $X_{tt}$ is the Martinelli parameter.

Kandlikar attempted to fit a correlation for any fluid across the boiling curve from ONB to fully developed boiling. He relates the heat transfer coefficient compared to single phase forced convection as a function of the Froude number, boiling number, convection number and several fluid specific parameters [9]. Kandlikar's correlation predicts the two phase heat transfer coefficient using:

$$h_{NB}/h_{conv} = C_1 Co^{C_2}(25Fr)^{C_5} + C_3 Bo^{C_4} F_l \qquad [2.13]$$

where the Boiling number is:

$$Bo = \frac{q"}{G\, h_{fg}} \qquad [2.14]$$

the convection number is:

$$Co = \left(\frac{1-x}{x}\right)^{0.8}\left(\frac{\rho_g}{\rho_f}\right)^{0.5} \qquad [2.15]$$

and $C_1$ through $C_5$ are constants specific to the boiling regime, and $F_l$ is a fluid specific parameter, Fr is the liquid Froude number, G is the mass flux.

Early research relied on single point temperature and average electrical power measurements to calculate heat transfer coefficients. These experiments were often developed to demonstrate the overall performance of industrial scale heat exchangers and boilers. Little focus on the small scale physics behind the heat transfer phenomenon was seen until the 1980's. More recent research has attempted to refine the boiling curves through all regimes using more sensitive instruments. Mudawar’s research group uses thermocouple arrays inserted into a heating element to measure temperature and heat flux over a wide range of flow boiling regimes in both earth and micro gravity environments with visualization of the flow [10, 11, 12, 13]. The limitation of this method is that the measurements are made at only a few positions along the test section made of a highly thermally diffuse material (copper) yielding only average heat transfer rates. Some researchers have used X-ray or neutron radiation attenuation through a boiling channel to quantitatively measure the flow field and void fraction [14, 15, 16]. Point measurements of void fraction have been made using conductivity probes [17]. Measurements of the entire wall temperature field have been made using liquid crystal thermometry [18]. Qualitative measurements via flow visualization have been made by dozens of researchers attempting to relate boiling regimes to heat transfer characteristics.

Very little experimental work has been performed that allows detailed local temperature measurements. A number of researchers have published correlations based on mechanistic models [19, 20] that cannot be easily verified due to the lack of detailed experimental data. Out experimental technique attempts to capture data at sufficient resolution to investigate the small scale physics responsible for multiphase heat transfer phenomenon.

## 2.1 Reduced Gravity Effect

Zero gravity research specifically on forced convective boiling is extremely limited. Other than Mudawar's research, only Saito [21] has published experimental data on zero gravity flow boiling. A number of experiments have been flown on both NASA's and ESA's reduced gravity flights investigating gravity effects on pool boiling [22, 23, 24]. These studies have shown a dependence of the heat transfer characteristics upon the magnitude of gravity. More specifically Raj, et al. [24, 25] reported that pool boiling phenomenon changes dramatically at gravity levels approximately 10% that of earth at the investigated heater size. They further concluded that previously accepted correlations did not accurately predict the heat transfer in these low gravity conditions, but suggested a gravity based scaling parameter to correct the predictions.

## 2.2 Infrared Thermometry

Infrared thermometry methods have been used for decades to measure temperatures in a wide range of applications. Recently researchers have been using these methods to obtain high speed temperature measurements along with visualizations of boiling phenomenon. Theofanous was the first to use modern infrared cameras to investigate pool boiling [26]. His experiments used a glass substrate with a very thin titanium heater. The titanium allowed heat generation and measurement of the surface temperature. Buongiorno used a similar technique but with an Indium-Tin-Oxide heater to allow both infrared and visual measurements [27]. Both of these experiments allow high speed, high resolution temperature measurements and Buongiorno has calculated the local heat flux by assuming appropriate boundary conditions for his heating substrate. A study investigating gravity effects on nucleate pool boiling using infrared thermometry has been performed by Stephan using an opaque stainless steel heater surface [28].

# 3. Technique

Based on the objective of obtaining temperature and heat flux measurements with high temporal and spatial resolution along with flow visualization, a unique method utilizing infrared thermometry is used in this work. Infrared thermometry has been used for decades to obtain accurate surface temperature measurements without direct physical contact. Any real surface at a temperature above absolute zero (0 K), emits electromagnetic radiation with energy according to Plank's Law:

$$E(T,\lambda) = \frac{2hc^2}{\lambda^5}\frac{1}{e^{hc/\lambda k_b T} - 1} \qquad [3.1]$$

where h = Planck's constant, c = the speed of light, $k_b$ = Boltzmann's Constant, λ = wavelength, T = temperature. From Plank's Law it can be seen that the energy emitted is

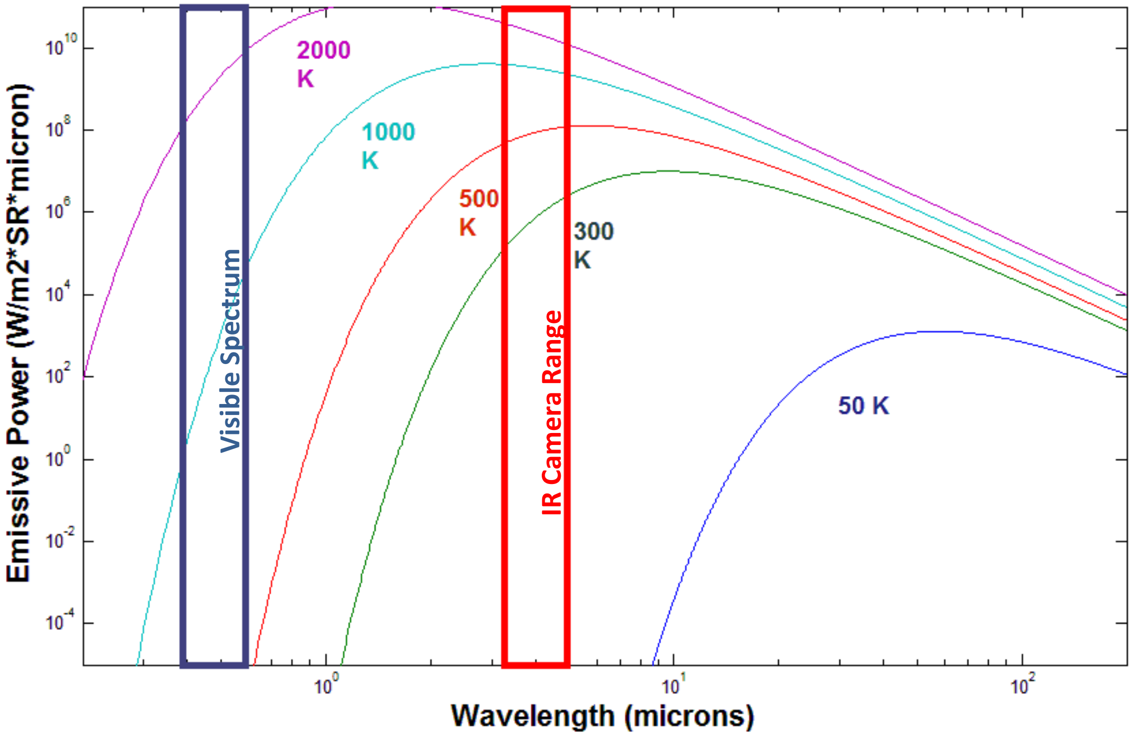

**Figure 3.1: Plank's Law for Various Temperatures**

a function of the wavelength and the temperature. For a constant temperature surface, the distribution of energy is shown in Figure 3.1.

As the surface temperature increases, the total emissive power increases the wavelength at which the emissive power peaks decreases significantly. Only at temperatures above about 800 K do surfaces emit in the visible spectrum which is why only surfaces above that temperature appear to emit radiation. To use thermometry to measure near room temperatures, the visible spectrum cannot be used. The infrared spectrum is usually defined as occurring between wavelengths of 1 and 10 microns. Infrared bandwidth depends on the type of detector used. In our case, the Indium Antimonide detector and optical filter used is only sensitive between 3.7 and 4.8 microns. An infrared camera normally utilizes a cryogenically cooled solid state imaging device to measure the intensity of radiation reaching the camera within its wavelength bandwidth. This intensity is converted to a digital level signal and recorded to form an image. These intensities can be converted to absolute temperatures if the camera has been calibrated against a known blackbody.

A blackbody is defined as a surface that absorbs all radiative energy reaching it, and emits energy according to Plank's Law. It is often easier to measure the total energy emitted from a surface across all wavelengths for a certain temperature. Stephan-Boltzmann's law can be derived by integrating Plank's Law over all wavelength and solid angle to obtain:

$$E(T) = \varepsilon\sigma T^4 \qquad [3.2]$$

where ε is the surface emissivity and σ is the Stefan-Boltzmann constant. From the integration of Plank's Law:

$$\sigma = \frac{2\pi^2 k^4}{15c^2hc^3} = 5.6704 \times 10^{-8}\ {}^{W}\!/_{m^2K^4} \qquad [3.3]$$

Because infrared cameras only capture radiation over a finite bandwidth between λ1 and λ2, and Equation 3.2 was determined by integration over all wavelengths, some modification is needed. It is customary to introduce a band emission factor, *F*, into Equation 3.2 instead of calculating the integral of Equation 3.1 for specific wavelengths:

$$E(T) = F_{\lambda 1-\lambda 2}\varepsilon\sigma T^4 \qquad [3.4]$$

where:

$$F_{\lambda 1-\lambda 2} = \frac{\int_0^{\lambda 2} E(\lambda,T)d\lambda - \int_0^{\lambda 1} E(\lambda,T)d\lambda}{\sigma T^4} \qquad [3.5]$$

Values of *F* have been tabulated so that the two integrals in the above equations are not required to be performed. An infrared camera can yield an accurate measurement of surface temperature using Equation 3.5, if the camera sensing element is properly calibrated from a known blackbody, and the actual surface emissivity is known.

## 3.1 Heat Flux Measurements

To determine not just the temperature of a surface, but the amount of heat transferred through it, the thermal conductivity of the material and the temperature gradient must be known. According to Fourier's Law:

$$q'' = -k\nabla T \qquad [3.6]$$

where q" is the heat flux, k is the thermal conductivity, and T is the temperature scalar field. Because thermometry only measures the temperature of a single surface, to calculate the heat flux a second temperature at a known distance away, separated by a material of known thermal conductivity must be measured. This layer provides a thermal resistance so that a temperature difference exists within the camera's sensitivity.

Consider the multilayer system shown in Figure 3.2. If both temperatures, $T_{s1}$ and $T_{s2}$ are known as a function of time, along with the thermal properties of the silicon, adhesive, and polyimide, then the temperature gradient through the entire system could be found using the transient heat conduction equation. From Fourier's Law, the heat flux can then be calculated from the temperature gradient. The general form of the heat conduction equation is:

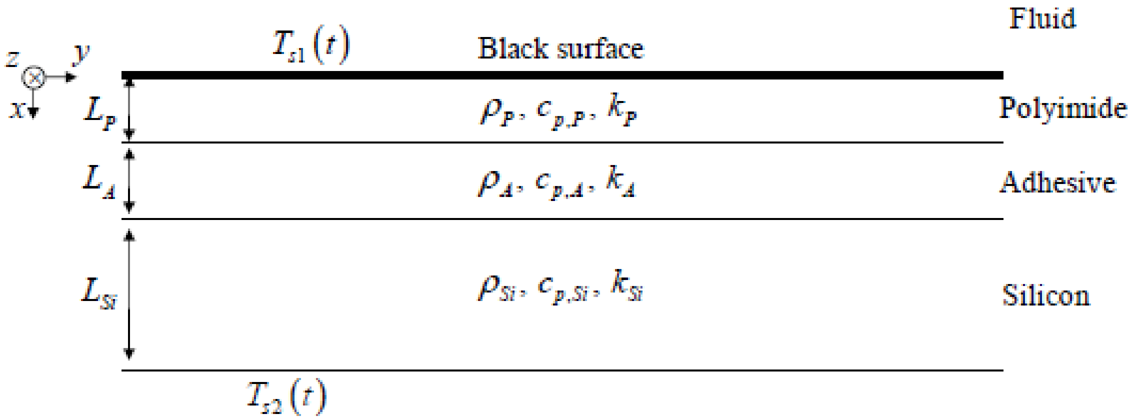

**Figure 3.2: Multi Layer Thermal Model**

$$\rho c_p \frac{\partial T}{\partial t} = k\nabla^2 T + \dot{q} \qquad [3.8]$$

In the system shown in Figure 3.2, several assumptions can simplify the heat conduction equation considerably. The thickness of the adhesive, $L_A$, and polyimide, $L_P$ are very small compared to the thickness of the silicon, $L_{si}$. Also, the thermal diffusivity of the

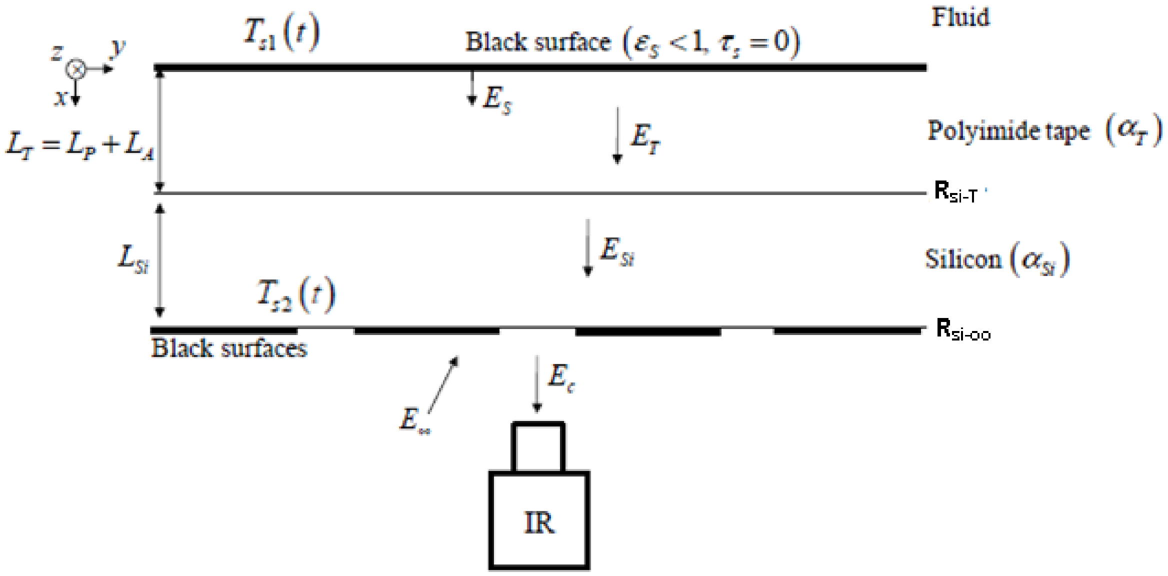

**Figure 3.3: Multi Later Optical Model**

silicon is very high due to its high density and thermal conductivity. For these two reasons, the heat flux in the system is almost entirely confined to the x direction, or:

$$\frac{\partial T}{\partial y} \ll \frac{\partial T}{\partial x} \quad and \quad \frac{\partial T}{\partial z} \ll \frac{\partial T}{\partial x}$$

This allows the problem to be simplified to a one dimensional domain. Also, because only the silicon layer has a heat generation term, $\dot{q}$, the heat conduction equations for the system can be simplified as:

$$\rho_{si} c_{p,si} \frac{\partial T}{\partial t} = k_{si} \frac{\partial^2 T}{\partial x^2} + \dot{q} \tag{3.9}$$

$$\rho_A c_{p,A} \frac{\partial T}{\partial t} = k_A \frac{\partial^2 T}{\partial x^2} \tag{3.10}$$

$$\rho_P c_{p,P} \frac{\partial T}{\partial t} = k_P \frac{\partial^2 T}{\partial x^2} \tag{3.11}$$

If the boundary conditions $T_{s1}(t)$ at x=0, and $T_{s2}(t)$ at x= $L_A$+ $L_P$+ $L_{si}$ are known along with some initial temperature profile, the temperature profiles for all time after t=0 can be solved.

## 3.2 Optical Considerations

In order to calculate $T_{s1}$ and $T_{s2}$ as a function of time, infrared thermometry is used as described in Section 3. Measuring surface temperature is straightforward if air is the only medium between the camera and the surface to be measured and surface reflections can be neglected. As seen in Figure 3.3, however, the camera views surface 1 through not only air, but also layers of silicon, and polyimide tape with adhesive. In the infrared spectrum, pure silicon is highly transparent, and polyimide and acrylic adhesive is somewhat transparent. The optical absorptivity and real component of the refractive index for both layers is given in Table 3.1. Because of these properties, the black

| | Silicon | Acrylic Adhesive | Polyimide Tape | Tape/Adhesive |
|---|---|---|---|---|
| Absorptivity ($m^{-1}$) | 52.6 | 1900 | 3000 | 7110 |
| Refractive Index | 3.41 | 1.46 | 1.7 | 1.6 |

**Table 3.1: Typical Optical Properties**

surface temperature, $T_{s1,}$ can be measured with the infrared camera, but only after compensating for attenuation, reflection, and emission in each of the layers. Because the acrylic adhesive and polyimide have similar optical properties they are treated as a single optical layer. The absorptivitiy of silicon and the combined tape layer were measured experimentally as will be described in section 4.2.

Attenuation of radiation occurs as photons strike a material and sometimes release their energy to the orbital electrons. Attenuation is therefore highly dependent upon the material properties, thickness, and the wavelength of radiation. The Beer-Lambert Law describes the change in radiation intensity through a material as:

$$I = I_0 e^{-\alpha d} \qquad [3.12]$$

where $I_0$ is the initial intensity of radiation, $\alpha$ is the absorptivity coefficient, and d is the thickness of the material. The Beer-Lambert Law may be re-written to calculate a transmissivity, $\tau$, where

$$\tau = {}^{I}/_{I_0} = e^{-\alpha d} \qquad [3.13]$$

Reflection occurs anytime radiation passes through a transition of two materials with differing real refractive indexes. The amount of reflection is dependent upon the index of refraction and the angle of incidence. However, if the radiation is assumed to be passing normally to the surface, as in Figure 3.3, the amount of reflection can be described by Fresnel's Equation:

$$R = \left(\frac{n_1 cos\theta - n_2 cos\theta}{n_1 cos\theta + n_2 cos\theta}\right)^2 = \left(\frac{n_1 - n_2}{n_1 + n_2}\right)^2 \qquad [3.14]$$

From the optical properties in table 3.1 and geometric dimensions of the multilayer, the transmittance and reflectance of each individual layer can easily be calculated from Equations 3.13 and 3.14. However the problem is further complicated by the fact that there are multiple reflections at each layer that compound in a geometric sum. Figure 3.4 shows how the energy emitted from the black surface at $T_{s1}$ is attenuated and reflected through the layers (the first two rays leaving the Si-∞ surface are shown, in reality there are an infinite number of reflections). The total energy leaving the Si-∞ surface can be found by summing each of the rays:

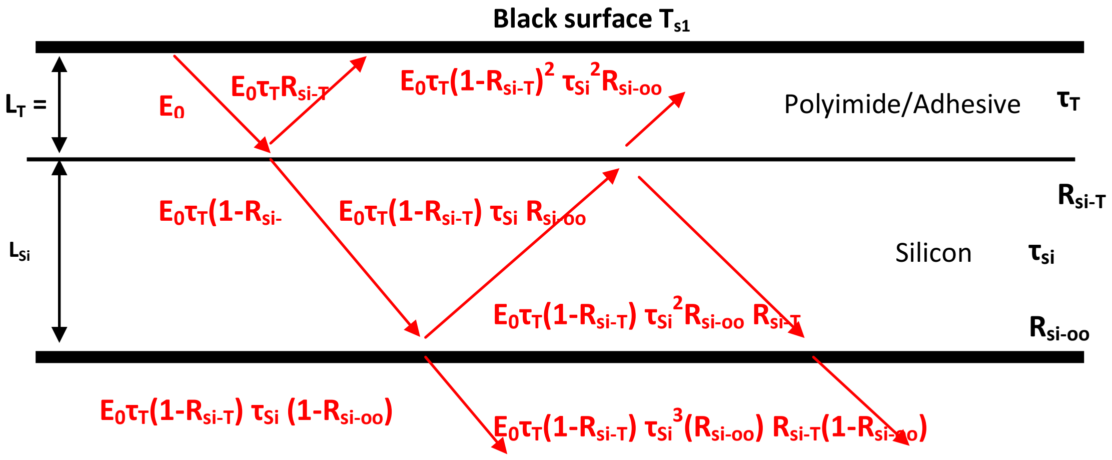

**Figure 3.4: Multiple Reflection Ray Tracing**

$$E/_{E_0} = \tau_T(1 - R_{siT})\tau_{si}(1 - R_{si\infty}) + \tau_T(1 - R_{siT})\tau_{si}{}^3 R_{si\infty} R_{siT}(1 - R_{si\infty}) + \tau_T(1 - R_{siT})\tau_{si}{}^5 R_{si\infty}{}^2 R_{siT}{}^2(1 - R_{si\infty}) + \cdots \quad [3.15]$$

Equation 3.15 gives the effective transmissivity, $\tau_{eff}$, for radiation leaving the black surface $T_{s1}$ and reaching the IR camera located at infinity.

If the silicon and polyimide/adhesive layers were completely transparent, the effective transmissivity derived above and the Stephan Boltzmann Law, Equation 3.15, would be enough to calculate true temperature, $T_{s1}$. Unfortunately the layers are not fully transparent, and they emit radiation according to Equation 3.16 based on their temperature profiles in the x direction. Consider a translucent ($\varepsilon>0$ and $\tau<1$), material shown in Figure 3.5. The slice of the material with thickness *dx*, emissivity $\varepsilon$, and absorption coefficient $\alpha$, will emit radiation with a magnitude of:

$$dE = \epsilon\sigma[T(x)]^4 dx \quad [3.16]$$

The amount of radiation leaving the slice *dx* and reaching surface 1 at a position of x=0 is given by:

$$dE = \epsilon\sigma[T(x)]^4 e^{-\alpha x} dx \quad [3.17]$$

The total radiation leaving surface 1 from the entire layer can be found by integrating Equation 3.17 over the layer thickness, *L*.

$$E = \int_0^L \epsilon\sigma[T(x)]^4 e^{-\alpha x} dx \quad [3.18]$$

If the layer temperature is uniform from x=0 to L, then Equation 3.18 reduces to:

$$E = \frac{\varepsilon}{\alpha}\sigma T^4[1 - e^{-\alpha L}] \qquad [3.19]$$

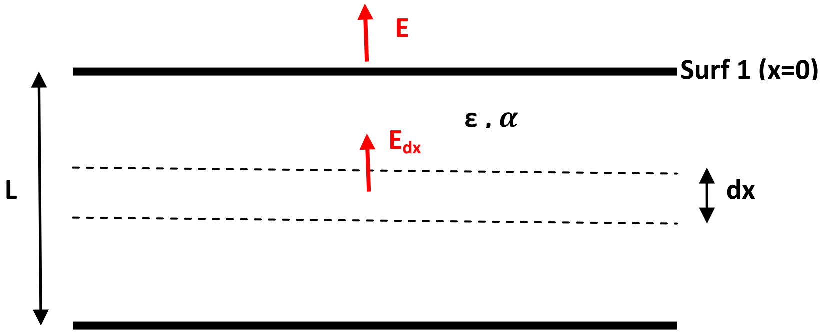

**Figure 3.5: Emission from a Translucent Material**

In the special case where the layer is infinitely thick and at constant temperature, the integral in Equation 3.18 becomes:

$$E = \int_0^\infty \epsilon\sigma[T(x)]^4 e^{-\alpha x}dx = \frac{\epsilon}{\alpha}\sigma T^4 \qquad [3.19b]$$

Infinitely thick layers act as blackbodies, emitting energy such that:

$$E = \sigma T^4 = \frac{\epsilon}{\alpha}\sigma T^4 \qquad [3.19c]$$

Therefore emissivity, ε, and absorptivity, α, must be equal in the translucent layer.

The radiative emission described by Equation 3.19 occurs in both the polyimide/adhesive layer, as well as the silicon layer. These emissions are further attenuated and reflected as they travel through the layer to the camera. The same multiple ray tracing method used to determine the effective transmittance for layer S1 can be used to determine the effective transmittance for the polyimide/adhesive and silicon layer.

The total energy reaching the camera, $E_c$, can be described as:

$$E_c = R_{\infty-c}E_\infty + \tau_{si-c}E_{si} + \tau_{T-c}E_T + \tau_{s-c}E_S \qquad [3.20]$$

Where:

$$E_\infty = F_{\lambda1-\lambda2}\sigma T_\infty^4 \qquad [3.21]$$

$$E_{si} = \int_0^{Lsi} \alpha_{si}F_{\lambda1-\lambda2}\sigma[T_{si}(x)]^4 e^{-\alpha_{si}x}dx \qquad [3.22]$$

$$E_T = \int_0^{L_t} \alpha_t F_{\lambda1-\lambda2}\sigma[T_t(x)]^4 e^{-\alpha_t x}dx \qquad [3.23]$$

$$E_S = F_{\lambda1-\lambda2}\sigma T_{S,1}^4 \qquad [3.24]$$

The effective optical parameters, $R_{\infty-c}$, $\tau_{si-c}$, $\tau_{T-c}$, and $\tau_{s-c}$are geometric sums of the various true reflectivities and trasmissivities. The number of terms needed to approximate these geometric sums depends upon the true optical properties used. Using

| | 1 | 2 | 3 | 4 |
|---|---|---|---|---|
| $\tau_{s-c}$ | -0.988 % | -0.0097 % | -9.66e-5 % | -9.55e-7 % |
| $\tau_{T-c}$ | -0.988 % | -0.0097 % | -9.66e-5 % | -9.55e-7 % |
| $\tau_{si-c}$ | -1.002 % | -0.0233 % | -5.43e-4 % | -1.27-5 % |
| $R_{\infty-c}$ | -5.250 % | -0.0519 % | -5.13e-4% | -5.07-5 % |

**Table 3.2: Error verses Included Number of Terms**

the optical properties from Table 4.1, Table 3.2 shows the percent error in for each effective optical property as a function of the number of geometric terms.

Assuming third order terms and higher are negligible, these parameters become:

$$\tau_{s-c} = \tau_T(1 - R_{siT})\tau_{si}(1 - R_{si\infty}) \\ + \tau_T(1 - R_{siT})\tau_{si}{}^3 R_{si\infty}R_{siT}(1 - R_{si\infty}) \tag{3.25}$$

$$\tau_{T-c} = (1 - R_{siT})\,\tau_{si}(1 - R_{si\infty}) + (1 - R_{siT})\,\tau_{si}{}^3 R_{si\infty}R_{siT}(1 - R_{si\infty}) \tag{3.26}$$

$$\tau_{si-c} = (1 - R_{si\infty}) + \tau_{si}{}^2 R_{si\infty}R_{siT}(1 - R_{si\infty}) \tag{3.27}$$

$$R_{\infty-c} = R_{si\infty} + (1 - R_{si\infty})\tau_{si}{}^2 R_{siT}(1 - R_{si\infty}) \tag{3.28}$$

The true optical parameters are experimentally determined as described in section 4.2. From these parameters and the geometry of the layer, effective optical properties can be determined from Equations 3.25 – 3.28.

## 3.3 True Surface Temperature Calculation

Assuming that the infrared camera is properly calibrated, the temperature readings from the camera are directly related to the energy reaching the camera, $E_C$, by equation 3.4. To determine the true surface temperature, $T_{s1}$, based on the energy leaving the surface, $E_S$, using Equation 3.20, the temperature profiles through the multilayer must be known. By coupling the transient heat conduction equation (Equations 3.9 – 3.11) for each of the layers with the optical transmission equation (Equation 3.20) and assuming some initial temperature profile, the true surface temperature, $T_{s1}$, can be solved at all times via the following algorithm.

1) Assume an arbitrary temperature profile, T(X), within the multilayer at t=0

2) Compute $E_{si}$ and $E_T$ from this temperature profile

3) Determine $T_{s1}$ from Equation 3.20 and 3.4

4) Solve the conduction equation using $T_{s1}$ and $T_{s2}$ as boundary conditions to obtain a new temperature profile T(X) at $t = t+\Delta t$

5) Repeat steps 2-4 for each successive time step

The initially assumed temperature profile decays within only a few time steps, after which the true temperature profile will be known for all values of x and time. The heat flux from the surface $T_{s1}$ into the surrounding fluid can be calculated via Fourier's Law, Equation 3.6, applied at the surface.

For computational ease, several simplifications are used. The Stephan-Boltzmann band emission factor, $F_{\lambda 1-\lambda 2}$, is a function of the wavelength cutoff values and the temperature of the surface. To save the computational time of performing this integral numerically every time a value of $F_{\lambda 1-\lambda 2}$ is needed, a 5th order polynomial curve fit was used over the range of temperatures needed in the problem, and with fixed values of $\lambda_1$=3.7 and $\lambda_2$=4.8 microns based on the infrared bandwidth of the camera.

The solution of the 1D transient heat conduction equation was performed at each time step using an implicit finite difference scheme with varying grid spacing. Because most of the temperature variation in the x direction occurs in the thin but more insulating polyimide and adhesive layers, the grid was refined in these regions, while a course grid was used in the highly thermally diffusive silicon layer. With 60 total nodes, the implicit problem was solved efficiently by inverting a tri-diagonal sparse matrix to yield the temperatures at the next time step. The integrals for $E_{si}$ and $E_T$, Equations 3.22 and 3.23, were performed numerically using a simple quadrangular rule using the same grid spacing as the finite difference problem.

# 4. Experimental Setup

The experimental setup used to obtain heat flux measurements in a both reduced and earth gravity environments can be broken into two parts. First are the laboratory based apparatus that allowed accurate measurement of the optical properties, calibration of the infrared camera, and verification of the technique. Second, is the self contained experimental rack that can be flow aboard either NASA's or the European Space Agency's reduced gravity aircraft, or used in the lab to obtain earth gravity data.

## 4.1 Camera Calibration

A FLIR Systems Silver 660M, Mid-Infrared range camera was used for all of the experimental configurations. Although factory calibrated, the data analysis software has a number of variables that can be modified which result in changes in recorded

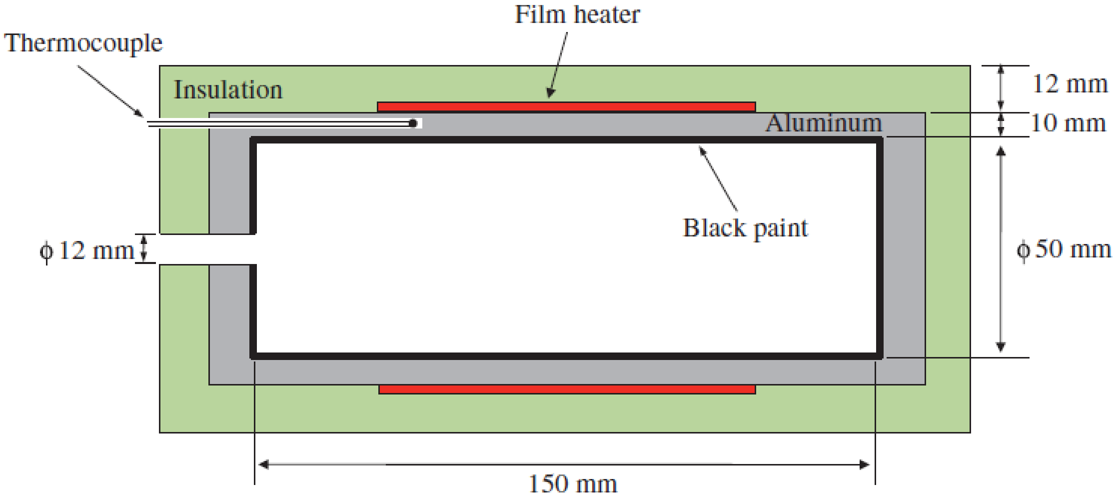

**Figure 4.1: Cross Sectional View of Black Body Emitter**

temperature. To verify proper operation and calibration of the camera, an in laboratory calibration test was performed. If properly calibrated, the camera's temperature measurements should be the same as the actual temperature of a surface with an emissivity of 100%. To create a blackbody radiation source, a temperature controlled enclosed aluminum cylinder with a black interior coating was created as seen in Figure 4.1. The cylinder was heated with a 100 watt resistive film heater, and insulated on the exterior. A small 12 mm diameter hole was drilled at one end of the cylinder to allow imaging of the inside of the volume with the camera. An ideal blackbody will absorb all radiation incident upon it. Any radiation entering the 12 mm diameter hole would have to reflect off the black interior surface, which itself has a reflectivity less than 5%, and exit through the same small hole. For this reason the black body in Figure 4.1 has an extremely high emissivity when viewed through the 12 mm hole. Based on geometrical view factors provided by Quinn [31], the emissivity of this blackbody is estimated to >0.999. This excellent blackbody is used as a radiation source for calibration as well as determination of optical properties in the following section.

## 4.2 Material Optical Properties

As shown in Section 3.3, the true optical properties including absorption and reflectivity, of each of the materials in the multilayer must be known to accurate calculate the true temperatures on the surface. Although silicon, acrylic and polyimide are common materials, and there are property values given in the literature, a small error in these values can cause disproportionately large uncertainties in the final calculated heat flux. Factors such as material purity and composition as well as exactly which

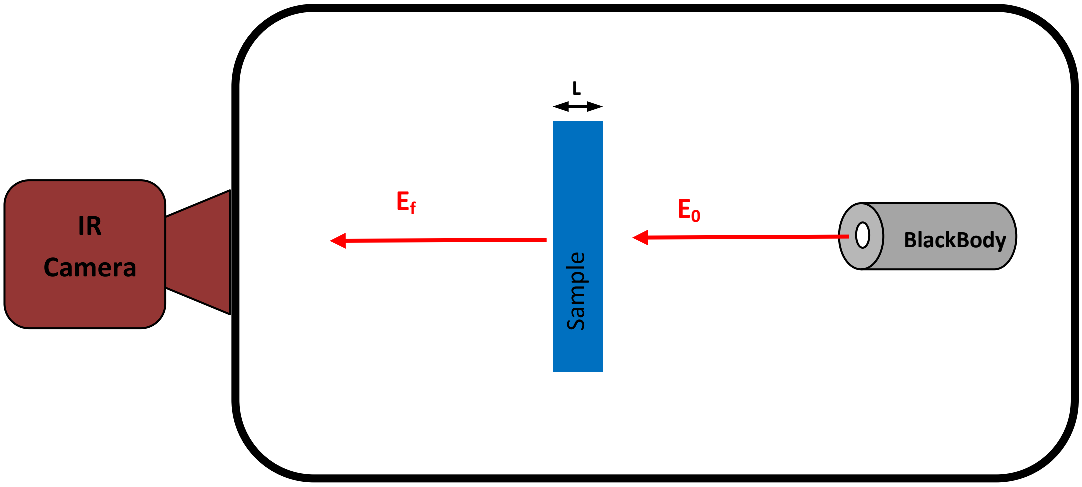

**Figure 4.2  Absorption Measurement**

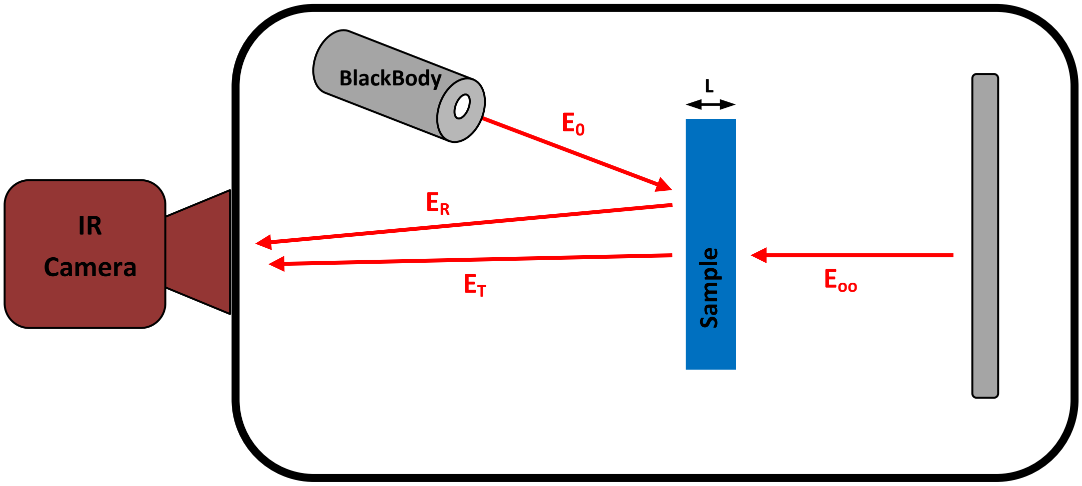

**Figure 4.3  Reflection Measurement**

wavelengths are being used can affect these optical properties. The best approach is to experimentally measure the properties using the same instruments (infrared camera) that will be used in the final experiments.

To determine the optical absorptivity, α, of a material the setup shown in Figure 4.2 was used. The radiation passing through the material is attenuated, and because the thickness of the material is known, the absorptivity can be calculated using the Beer-

Lambert Law, Equation 3.12. In all of the optical property experiments, the apparatus was placed in an enclosure at a known temperature, so that any reflection effects were due to the enclosure only.

The configuration shown in Figure 4.3 was used along with the absorption data to determine the reflectivity. Because reflectance is a function of incidence angle, the blackbody and IR camera area were aligned so that the incident angle of reflection was as close to 90 degrees as possible. By using the results of both experiments simultaneously, both the absorptivity and reflectance of any material could be determined. To ensure these values were not a function of temperature, the measurements were repeated over a range of temperatures between 20 and 80 °C. Table 4.1 shows the values of absorptivity of each material from the literature as well as the values determined from experimental data. The discrepancy in the absorptivity values for silicon was likely because the silicon used in our experiment was not completely pure. Zero reflectance between the polyimide tape and air was assumed because the index of refraction is close to that of air.

| | Silicon [32] | Silicon Experimental | Polyimide [33] | Acrylic [33] | Polyimide/Acrylic Tape Experimental |
|---|---|---|---|---|---|
| α ($m^{-1}$) | 0.1 | 52.6 | 3000 | 1900 | 7100 |
| n | 3.41 | | 1.7 | 1.46 | |
| R (in air) | 0.299 | 0.298 | 0.067 | 0.035 | 0 |

**Table 4.1: Optical Properties for Materials Within the Multilayer**

## 4.3 Flat Multilayer Construction

The multilayer was created by adhesively bonding a layer of polyimide tape to a silicon substrate. For the simple, flat rectangular geometry used in the droplet evaporation study in Section 5, commercially available polyimide tape was applied using its own acrylic adhesive. For the temperature and heat fluxes used, it was determined that 30 micron thick tape would create temperature differences across the layer that were easily measured by the camera, yet kept the total temperature difference relatively small. Using a Tencor Model TP-20 profilometer with an accuracy of 100 nm, the actual thickness of the polyimide and the acrylic adhesive was determined to be on average 15 microns each. The silicon substrate was simply an un-doped 10 cm diameter silicon wafer, 508 microns thick. In order to create a very thin but completely opaque coating on which to sense the surface temperatures, a high carbon content black paint was applied to the surface of the polyimide. A commercial vendor, Laser Film Technlogy Inc., was

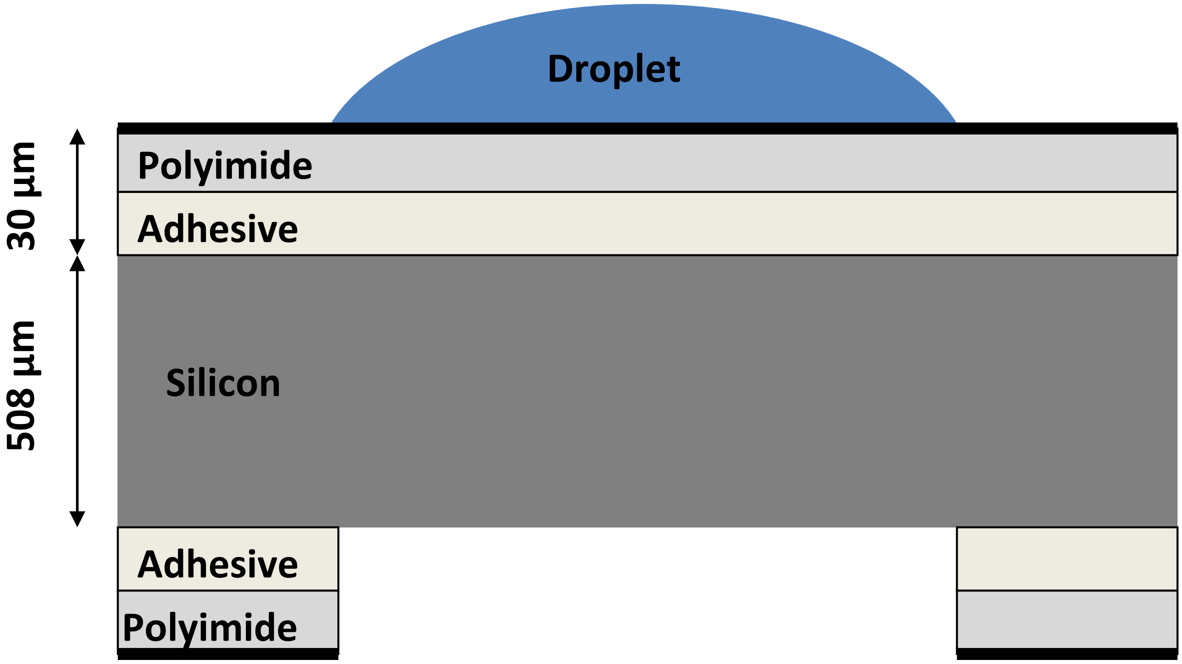

**Figure 4.4: Cross Sectional View of the Flat Geometry Multilayer**

contracted to apply Nazdar GV series, gloss black lithography paint to the polyimide tape. The thickness of the black coating was determined to be approximately 6 microns. Using the calibrated infrared camera and a controlled temperature source, the emissivity of the black coating was determined to be 0.90. Figure 4.4 shows the construction of the multilayer used in the Section 5 droplet evaporation experiment. The entire top surface of the wafer was covered with the opaque polyimide coating. Only portions of the bottom surface were covered since the bottom surface temperature was needed to calculate the top surface temperature and heat flux per Section 3.4.

## 4.4 Cylindrical Multilayer Construction

To achieve the same effect in the cylindrical geometry necessary to investigate flow boiling through pipes, the polyimide tape needed to be inserted on the interior and exterior of a silicon tube. The silicon tube was manufactured by drawing a rod of slightly doped silicon from a molten pool, blanks were cut, an interior 6 mm diameter surface was bored, then both surfaces were polished. The result was a 12 cm long silicon tube, with a wall thickness of 1 mm that is nearly completely transparent in the infrared. Before the polyimide tape could be applied to the interior and exterior surfaces as shown in Figure 4.5, accommodations for two sets of electrical connections were constructed. Since it was desired to heat the silicon tube resistively by passing current through it, electrodes needed to be deposited at each end. Pure crystalline silicon has a resistivity of $3.2 \times 10^5$ Ω-cm, but the silicon used had a resistivity of between 10 and 100 Ω-cm. From 4-wire resistance bridge measurements, the silicon tubes were found to have a resistance of approximately 1200 Ω at room temperature. To drive enough current for adequate heat

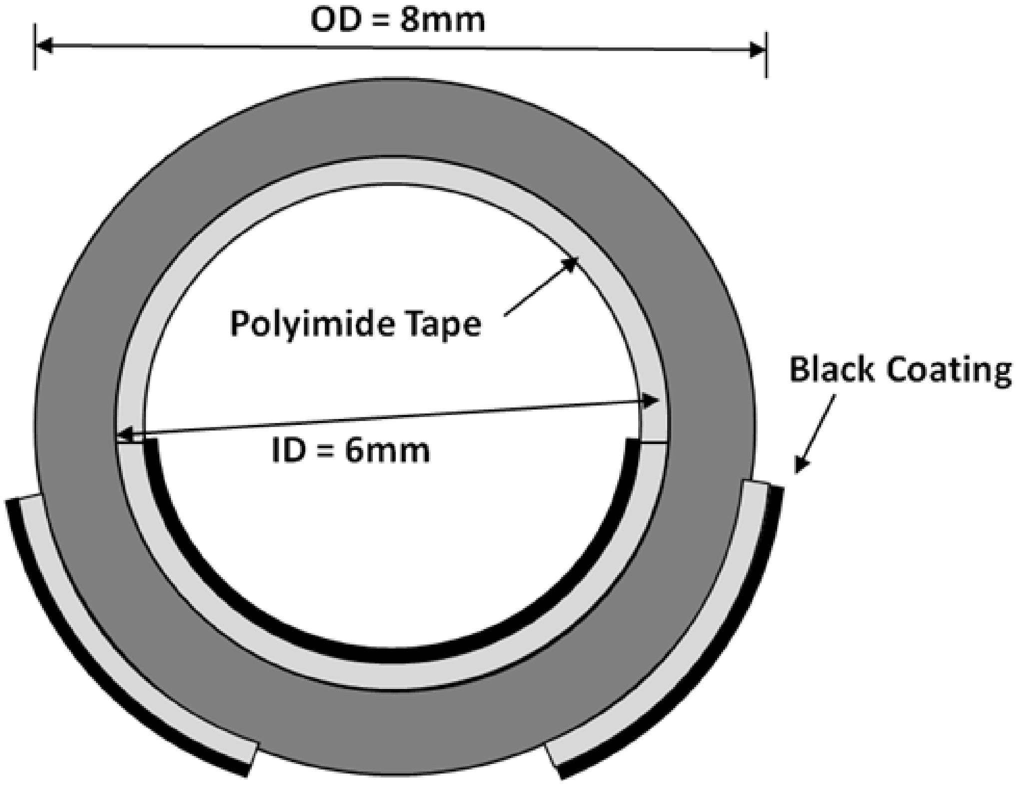

Figure 4.5: Silicon Tube Multilayer

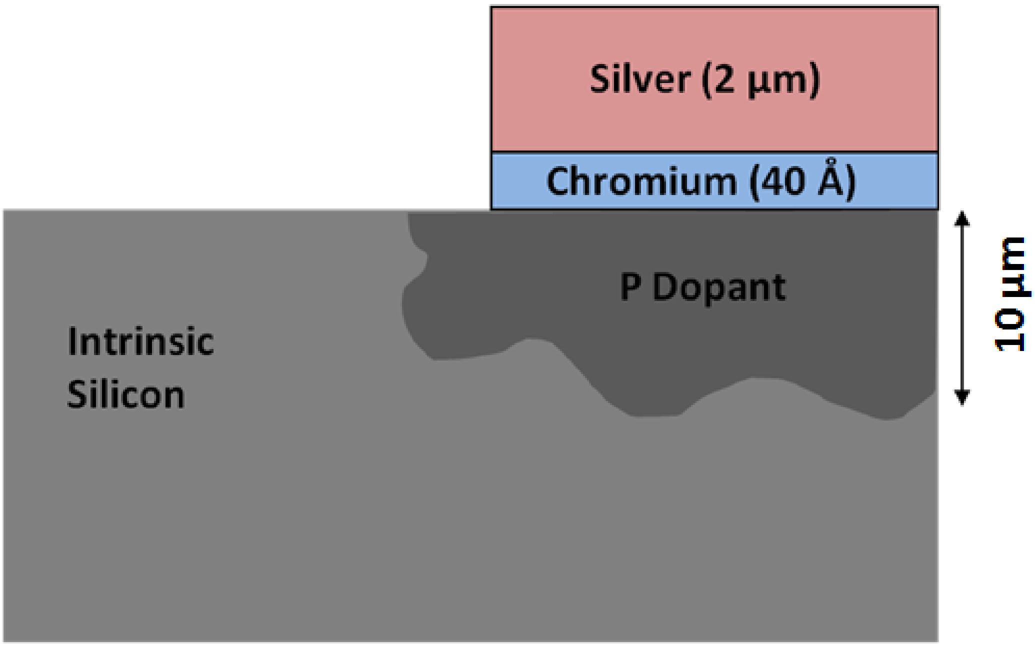

Figure 4.6: Detail of Silicon Tube Electrode Construction

Figure 4.7: Metra Thermal Evaporator

rates, a high voltage must be applied. From Ohm's law, if 300 VDC is applied, a power of 75 W can be generated giving a heat flux of 4 W/cm$^2$.

The contact resistance between power leads and the silicon tube was quite high (15 Ω ) even when soldering techniques were used to attach the leads. An added complication was the fact that soldering to a highly polished, pure silicon material was quite difficult. To solve these problems, metal contact surfaces were created using thermal deposition techniques to provide an area that physical spring type contacts could be attached. Silver and gold, while excellent conductors, do not readily adhere to silicon, therefore it is common to first apply a chromium adhesion layer. Pure chromium can have serious stress cracking issues especially when undergoing thermal cycling, so the adhesion layer is usually limited to only a few nanometers in thickness. A further complication was that when the silicon was coated with a good conductor such as chromium or silver, the surface acted like an n-p junction where silicon was the semiconductor and the metal was the conductor or p material. This created a primitive diode with a low reverse bias resistance creating more contact resistance problems for our connections. The only way to reduce the effects of this n-p junction was to increase the conductivity of the silicon in the region near the chromium adhesion layer through doping.

Figure 4.6 shows how the contact electrodes were created in an ideal flat silicon substrate. The Phosphorus (p-type) dopant was applied to the silicon surface and then thermally driven into the silicon through a batch oven process. The chromium and silver were then deposited via thermal evaporation. In the cylindrical tube geometry, the electrodes need to cover the entire circumference of the tube in four bands, two for the power electrodes and two for current measuring leads. To accomplish this, a unique process was developed using the University of Maryland’s FabLab.

To prepare the silicon for doping it was bathed in 5 molar hydrofluoric acid to etch off any naturally occurring silicon dioxide insulating layer. After rinsing and drying, the silicon tube was coated with phosphorus dopant covering four concentric rings where the electrodes were eventually deposited. These rings were positioned with the help of a master physical mask. The dopant was then hardened by baking at 120 °C for 30 minutes. Thermal diffusion of the phosphours dopant was accomplished by baking the tube in a process oven at 900 °C for 30 minutes in a partial oxygen atmosphere. Based on the dopant’s vendor data, this process yielded a depth of approximately 10 microns. Excess dopant was removed after the tube cooled, using a standard 5 molar buffer oxide etchant.

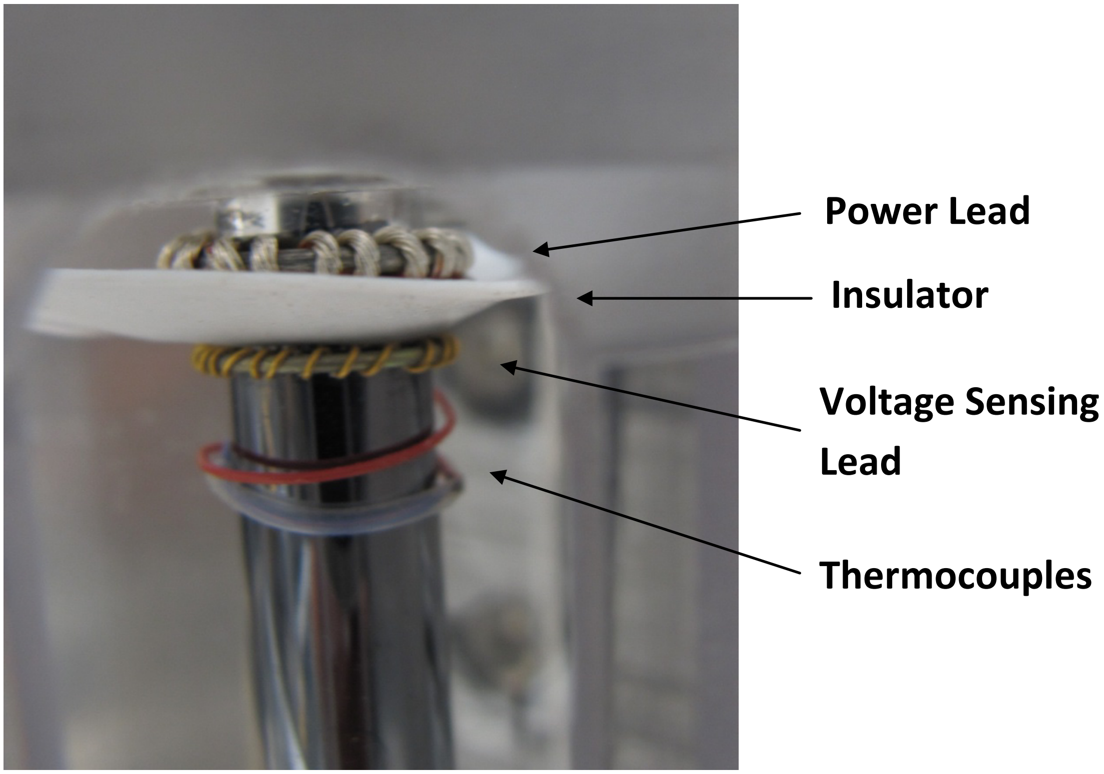

**Figure 4.8: Silicon Tube Electrodes**

The application of the chromium and silver layers was accomplished using a Metra thermal evaporator (Figure 4.7) in 3 separate processes, each one covering a 120° arc over the tube's circumference. Fundamentally, a thermal evaporator allows layers of metal to be deposited angstroms at a time as metal boils or sublimates (depending upon the critical point of the material) at very low pressures and moderate metal temperatures. After the evaporator chamber was pumped down to less than $2 \times 10^{-6}$ Torr, a ceramic crucible containing the metal was resistively heated. A cloud of metal vapor evaporates from the crucible, and anything in its path is coated in a layer as the vapor condenses on cooler surfaces. A quartz crystal microbalance was monitored to gauge the thickness of metal deposited on the surfaces. The silicon tube was located approximately 20 cm above the crucible, and masked using Kapton tape, so that only the areas previously doped would be coated, forming the four electrode rings. Approximately 40 angstroms of Chromium was deposited, followed by nearly 2 microns of silver. The chamber was vented with nitrogen, cooled and opened to allow the tube to be rotated 120°. Repeating the process twice more completed the electrode rings. Figure 4.8 shows one end of the silicon tube with the power and voltage sensing leads connected, along with two thermocouple sensors used for over temperature protection circuitry.

## 4.5 Test Section Construction

The entire silicon tube was mounted inside a "test section", which provides fluid connections, physical mounting, and an optical view path to the infrared camera. To allow viewing the full 360° of the tube's circumference, an assembly of six gold plated mirrors was used to split the infrared camera's field of view into two sections. Half the field of view allowed visualization of the flow by looking at the tube through the transparent side. The other half of the field of view allowed temperature measurements to be made on both the inside and outside surfaces. Figure 4.9 shows the mirror and silicon tube setup from a top view.

The test section was manufactured from several pieces of clear polycarbonate material. The outer assembly held two inner pieces with a series of set screws. Each of the inner pieces provided a fluid connection to the silicon tube via O ring seals, and Swage-Lok external fittings.

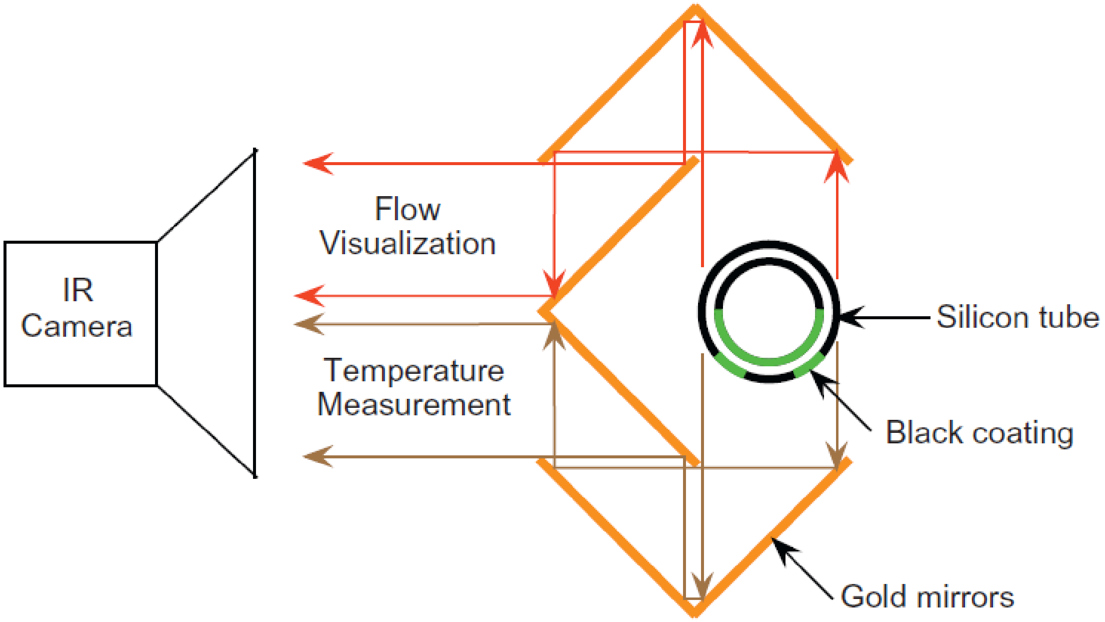

**Figure 4.9: Camera View Setup, Mirror Arrangement**

Each of the inner pieces also provided pressure tap connections via 1/16 inch (1.58 mm) tubing to a highly sensitive differential pressure transducer to allow measurement of the pressure drop across the tube. On the downstream or top end of the test section, a 2 cm long quartz tube was used to allow visualization of the flow in the visible spectrum, or for film thickness measurements in the future.

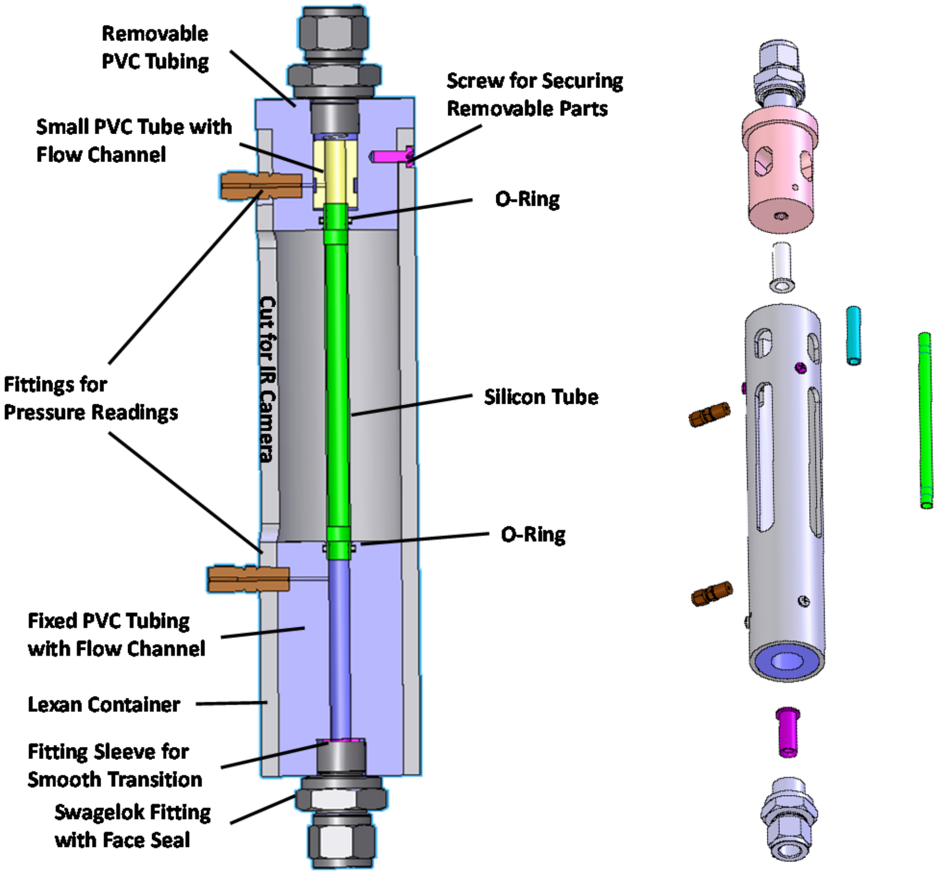

**Figure 4.10: Test Section Expanded View**

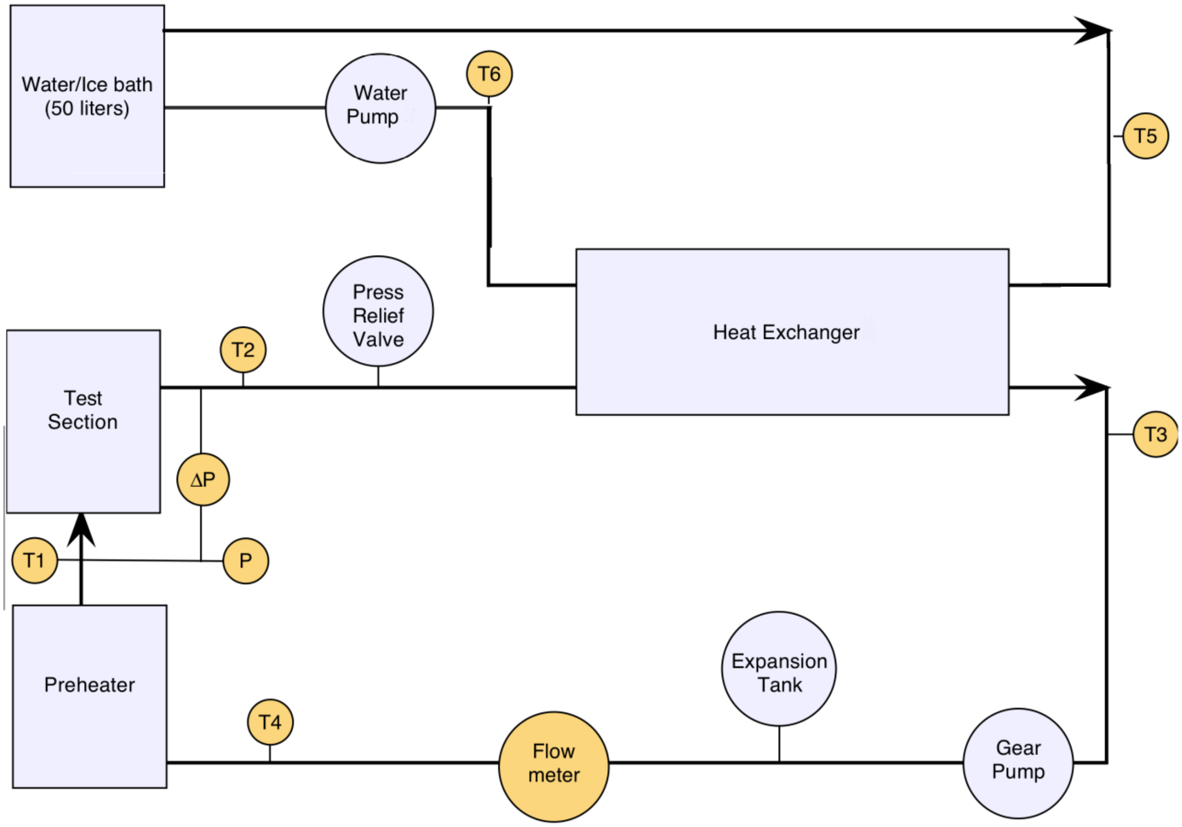

Figure 4.11: Fluid Loop Schematic Layout

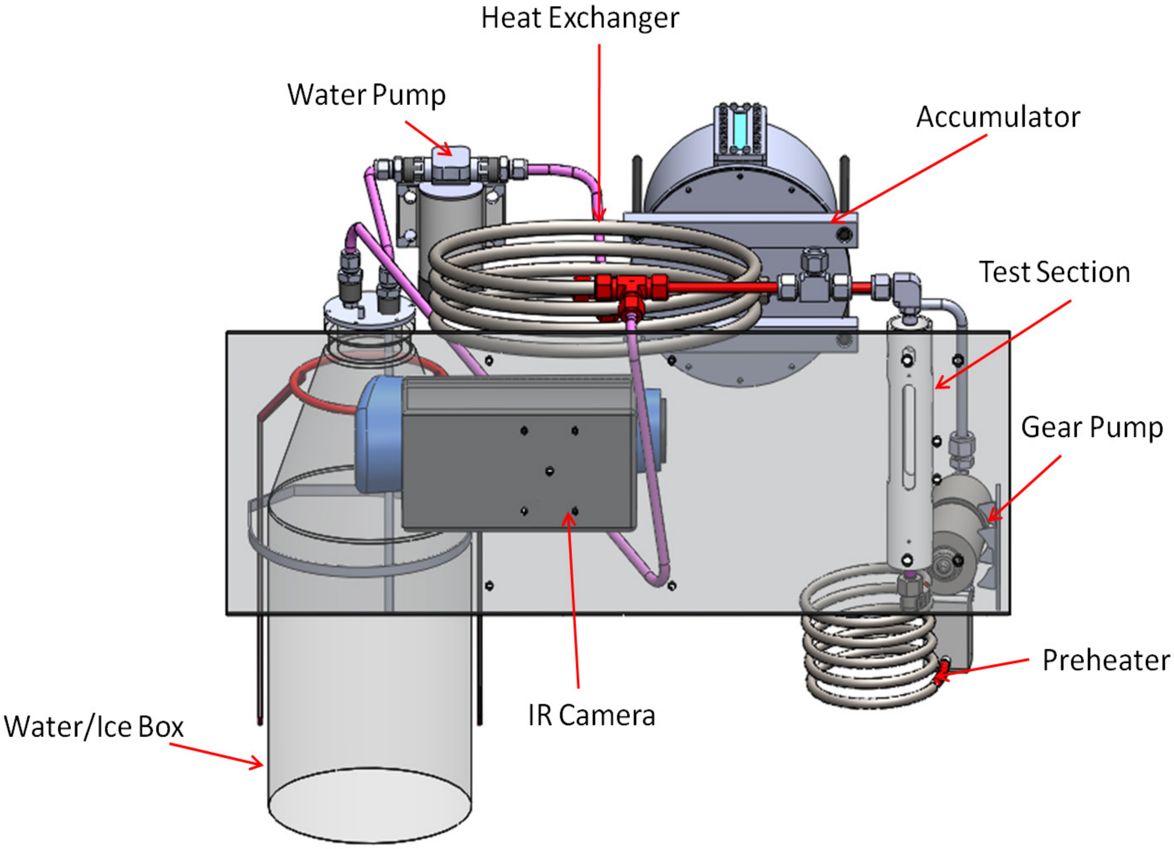

Figure 4.12: Fluid Loop Physical Layout

## 4.6 Fluid Loop

To provide fluid (normally 3M PF-5060) at a controlled flow rate, temperature and pressure to test section, a flow loop housed within the test rig was constructed. The flow loop, schematically shown in Figure 4.11, consisted of a positive displacement gear pump, stainless steel bellows type accumulator, flow meter, pre-heater, and condenser. Thermocouples provide temperature measurements of the fluid, and are indicated as T1 through T6. The gear pump, Micropump Model 132-000, was magnetically coupled to a direct current motor, and has a built in recirculation line in the event of operation with no flow path. The flow rate of the pump was manually controlled by adjusting the supplied voltage. The flow meter, Omega Model FLR-1010D, was capable of measuring flow rates of between 100 and 2000 ml/min. A flow rate display was provided, as well as a 0-5 VDC analog output that was recorded by the data acquisition system. The accumulator was a custom built design that allows a constant pressure to be maintained while the system volume increases during heat up. By pulling a vacuum on the "dry" side of the accumulator and measuring system pressure and temperature, a measurement of total gas concentration in the fluid was obtained. After experiencing problems with flow transients when the gravity magnitude changes during in flight operation, the original diaphragm type accumulator was replaced with a stainless steel bellows incased in an aluminum chamber with pressure connections and sight glass. Because the bellows moved in a horizontal direction (aligned with the aircraft longitudinal axis in flight) changes in gravity as the aircraft performs its parabolic maneuvers did not affect the system pressure or flow rate.

The pre-heater was designed to heat the fluid in a controlled manner from room temperature up to saturation temperature at any of the design flow rates. To accomplish this, a large amount of power was required while heating the fluid at fluxes well below the critical heat flux point and ideally without phase change. A 3/8 inch (9.52 mm) diameter stainless steel pipe with a 0.3 mm wall thickness and a length of 2.9 meters allowed the necessary power to be applied to the fluid, and allowed resistive heating internal to the stainless steel pipe. Although stainless steel has a low resistivity, the pipe is extremely thin walled and relatively long, therefore a total resistance of approximately 0.28 ohms was obtained. Electrical current was applied via two 4 gauge cables brazed to the outside of either end of the tube. The entire length of tube was coiling with an approximate diameter 20 cm to reduce its footprint in the test rig. Control of the pre-heater was through solid state relays switching 12 or 24 VDC power in pulse width modulation control when used aboard NASA aircraft. For some of the laboratory experiments where higher power to the pre-heater was desired a 120 VAC variable transformer was coupled to a 10:1 step down transformer to allow high current 0-12 VAC power from a wall receptacle to be applied. Voltage was measured with a Agilent model 34401A benchtop multi-meter and current with a Tektronix P6021 indirect clamp on current probe. More detail on the pre-heater control and calibration in this mode can be found in appendix A-1.

Under normal operating conditions the output of the test section was a liquid vapor mixture at saturation temperature. In order to recycle this fluid back to the gear pump, it must be condensed and subcooled to a fixed temperature. This was accomplished with a custom built counter-flow concentric tube heat exchanger. The heat exchanger was a 2 meter long stainless steel tube containing the fluid, surrounded by a 1 inch diameter polypropylene tube containing cooling water. The cooling water was supplied from a 5 liter dewar, normally filled with ice water, with a 12 VDC Reverso Model GP311 centrifugal pump. The ice water pump was controlled via solid state relays in pulse-width modulation mode to control the degree of subcooling of the fluid.

Other components in the fluid loop included a combination filter and fluid/gas separator that allows degassing of the fluid volume while in operation. A globe valve immediately downstream of the gear pump provided a pressure drop to allow more stable control at small flow rates. Fill and drain connections were provided at the high and low

| | | |
|---|---|---|
| Fluid Volume | 1.8 liters | |
| Flow rate (ml/min) | 50 | 2000 |
| Test Section Inlet Temp (C) | 5 | 56 |
| Pressure | Atmospheric +-3 psia | |
| Test Section Fluid Velocity (m/s) | 0.029 | 1.179 |
| Test Section mass flux (kg/s-$m^2$) | 49.5 | 1980 |
| Test Section Reynolds Number | 464 | 18568 |

**Table 4.2: Flow Loop Parameters**

points of the loop. All of the previously described components allowed a wide range of flow variables to be controlled as summarized in Table 4.2.

## 4.7 Electrical and Control Systems

The entire experimental setup must be self sufficient with the exception of external 115 VAC power supplied by a wall receptacle or the aircraft. Safety requirements for flying on NASA and ESA aircraft required all electrical systems to be shut down in an emergency with the push of a single button. Over temperature protection was desired on the test sections and preheater to prevent permanent damage in the case of a malfunction. For all of these reasons, an extensive electrical and control system was designed for the test rig.

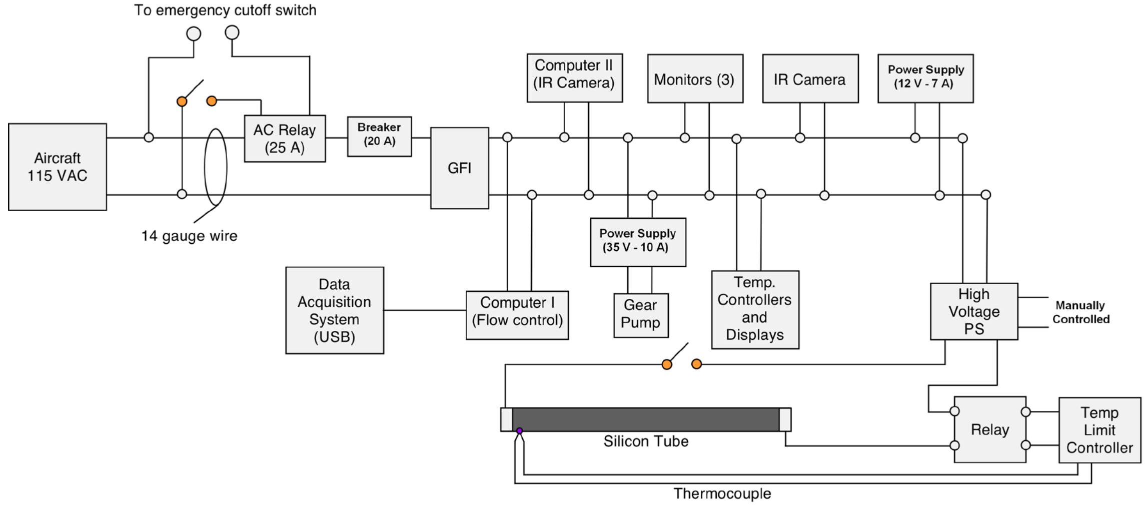

**Figure 4.13: 115 VAC System Schematic**

The electrical system within the rig can be broken into three parts: the 115 VAC bus, a 12 VDC bus for various sensors and pumps, and a 24 VDC high current system provided by onboard lead acid batteries. All three of these systems were controlled through a single box located near the primary operator’s position. Figure 4.13 shows the various loads supplied by the 115 VAC bus. Power was supplied by the aircraft or wall receptacle in the lab, and had over current protection via a conventional circuit breaker. All of the

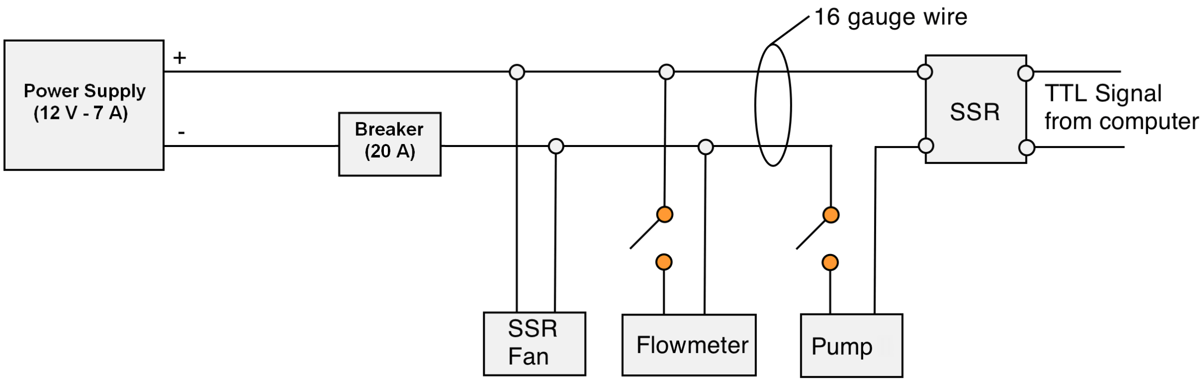

Figure 4.14: 12 VDC System Schematic

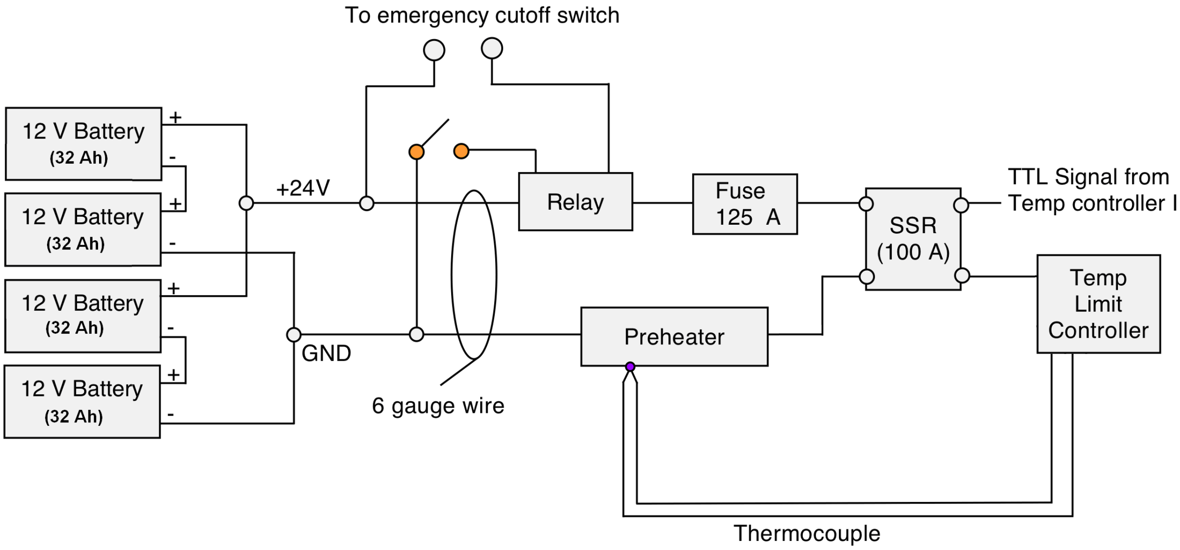

Figure 4.15: 24 VDC System Schematic

loads were GFCI protected, and could be de-energized by removing latching voltage supplied to a normally open master relay. Over temperature protection of the silicon tube was accomplished by double redundant temperature controllers monitoring the surface temperature at the exit of the test section. These controllers provided latch voltage to a dedicated solid state relay that would de-energize the high voltage power supply at a temperature of 90 °C.

The 12 VDC system, shown in Figure 4.14, was supplied by a 7 amp commercial power supply, then routed through a dedicated 12 VDC circuit breaker in the control box. Emergency shutdown of the 12 VDC system was accomplished anytime the 115 VAC system was shutdown because the power supply was fed from this system.

The 24 VDC system was powered from 4 sealed lead acid batteries located in the base of the rig. These were necessary because the current draw from the preheater was 84 amps, and a power supply rated at this current would be prohibitively large. Wiring for the batteries was accomplished with 6 gauge cable, and could be modified to supply

**Figure 4.16: Control Box**

12 VDC vice 24 if lower power was required from the preheater. A 150 amp normally open relay provided emergency shut-down capability of the system and a 125 amp fuse provided over current protection. Control of the preheater power is via pulse width modulation of a 100 amp solid state relay. It was found that the steadiest control of the fluid inlet temperature to the test section was accomplished by fixing the preheater surface temperature to a value 3-5 °C above the desired fluid temperature. An Aubur Model SYL-1512 temperature controller provided the solid state relay control voltage. Over temperature protection for the preheater was provide by a second temperature controller sensing a thermocouple placed on the exit of the preheater's surface.

Figure 4.16 shows the control box housing the temperature controllers, solid state relays, 12 volt electrical bus, and breakers. Located on the top of the control box was the red emergency shut-down button. In addition to control and safety, the control box housed 6 extra temperature controllers which provided backup indication of critical temperatures inside the apparatus in case the data acquisition system was not functioning.

## 4.8 Data Acquisition

To monitor and record the various temperatures, pressures and flows in the apparatus, an Omega Model OMB-DAQ-3005, 32 channel data acquisition system was used. This system could utilize all of the input channels as either a thermocouple or 0-5 VDC analog input. T type thermocouples were used throughout to allow temperature measurements via the data acquisition system and for display on the control box. Absolute pressure inside the flow loop was measured with an Omega Model PX209-030A pressure transducer with a range of 0-30 psia (0 - 206 kPa) and an accuracy of

±0.45 psia (±3.1 kPa). Differential pressure drop across the test section was measured with a Valindyne Model P55D-1-N-1-36-S-4-A transducer with a range from - 0.5 to + 0.5 psid (- 3.4 to + 3.4 kPa) with an accuracy of ± 0.005 psi (± 34 Pa). Both of these transducers had 0-5 VDC outputs that were recorded by the data acquisition system and displayed on the control box.

Voltage and current were supplied to the silicon tube from a Sorenson XGS-600 high voltage power supply, and were measured by the data acquisition system through a system of voltage divider resistors. Tube voltage was measured from the inner electrodes to give an accurate reading of the voltage drop across the silicon not including voltage loss in the power leads and contact resistance. At a maximum power supply voltage of 300 VDC, the actual voltage drop across the silicon tube is approximately 280 VDC. The current applied to the test section was measured by recording the voltage drop across a 10 Ω resistor. Both the voltage divider network and current measuring resistor were calibrated with bench top multi-meters, and checked with the data acquisition readings.

Additional parameters such as battery voltage, ambient temperature inside the rig, and ice water temperature were measured by the data acquisition system as well. Acceleration was provided by a 3 axis accelerometer mounted to the frame of the apparatus and recorded by the data acquisition system. All functions of, and data recorded by the data acquisition system were controlled by a Labview program running on a dedicated computer. Measurements were normally recorded at a frequency of 10 Hz.

A separate, high performance desktop computer was dedicated to operating and recorded data from the infrared camera. Connectivity between the computer and camera was via gigabit Ethernet, which allowed 100 Hz frame rate at full resolution or up to 2000 Hz with a reduced image size, to be recorded. Synchronization between the Labview and IR camera computers was via internal computer clocks. As a secondary method of synchronization, a small infrared LED was mounted on the test section on the edge of the camera's field of view. The LED could be toggled on and off with the Labview program, recorded in the data stream, and seen on the camera movies.

## 4.9 Structural Layout

The experimental rack, shown in Figure 4.17, with a total weight of 260 kg and

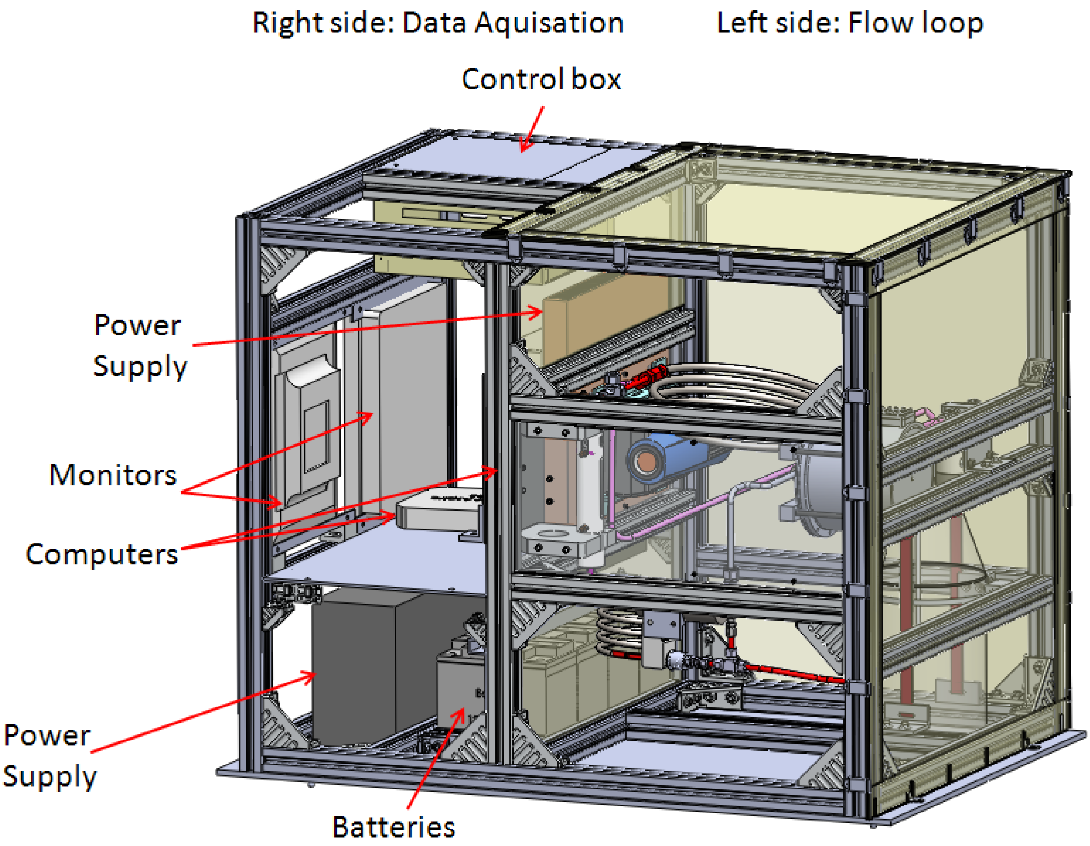

**Figure 4.17: Test Apparatus**

was primarily composed of commercial extruded aluminum beams mounted to a 10 mm thick aluminum base plate. Overall dimensions of the rack were 1.1 m long by 0.84 m wide by 0.94 m high. The base plate had 6 bolt holes that align with threaded fittings on the aircraft floor. On the fluid side of the rack, double containment of the refrigerant was accomplished by encasing the exterior sides with clear Lexan panels attached with quick release fittings. This enclosure also prevented temperature variations from the outside environment affecting the camera readings via reflection.

## 4.10 Degassing and Calibration

Before measurements were taken, the fluid volume of PF-5060 was degassed and filtered. A vacuum pump drawing on the vapor side of the liquid-vapor membrane filter was run for a period of 6 hours while the fluid loop was circulated at a moderate flow rate (500 ml/min). At hour intervals the degassing was stopped, and a total gas measurement taken. The total gas within the PF-5060 can be measured by pulling a vacuum on the air side of the accumulator, and creating a vapor space inside the accumulator. The absolute pressure and fluid temperature are recorded and using Henry's Law the total gas can be calculated, where the total gas concentration is:

$$C_g = H(T)P_g \qquad [4.1]$$

where H(T) is Henry's constant for PF-5060 as a function of fluid temperature, and $P_g$ is the partial pressure of gas in the vapor space which can be calculated by:

$$P_g = P_{tot} - P_{sat} \qquad [4.2]$$

where $P_{tot}$ is the measured absolute pressure of the system, and $P_{sat}$ is the saturation pressure of PF-5060 at the fluid temperature. Henry's constant for PF-5060 has been calculated by Raj [40] to be $5.4x10^{-8}$ mole/mole-Pa for fluid temperatures between 31 and 60 °C. Three hours of continuous degassing reduced air saturated PF-5060 from a total gas reading of 1500 ppm to less than 50 ppm.

The algorithm described in Section 3 requires a known temperature of the surroundings, $T_{inf}$, to compensate for energy reflected off the surface of the silicon tube. Experimental results have shown that the correct value of $T_{inf}$ varies by location along the silicon tube, and with silicon tube temperature. Simply setting $T_{inf}$ equal to the room temperature does not yield the correct heat flux due to variations in reflectivity across the length of the tube. A $T_{inf}$ for every axial position along the tube was determined during a known zero heat flux condition, essentially performing a pixel by pixel calibration at every axial position. This was accomplished by recording temperatures using the infrared camera while circulating fluid at a fixed temperature at high flow rates. The losses to ambient were assumed to be negligible; therefore the silicon tube was be in an isothermal state. The $T_{inf}$ calculated at each axial position was then used in the analysis algorithm to determine the true temperatures and heat fluxes.

## 4.11 Experimental Uncertainty

Maximum experimental uncertainty for the technique described in the previous sections was calculated based on uncertainty in each input to the analysis algorithm. Because the algorithm utilizes a numerical method, the uncertainty cannot be analyzed by simple differential analysis. For a simple explicit function, F, with N input variables, $X_1$ to $X_N$, so that:

$$Y = F(X_1, X_2 X_3 \dots X_N) \tag{4.3}$$

the maximum uncertainty is:

$$\text{error}^2 = \sum_{i=1}^{N} \left( \frac{\partial F}{\partial X_i} \Delta X_i \right)^2 \tag{4.4}$$

where $\Delta X_i$ is the maximum uncertainty for each input variable. To perform this type of uncertainty analysis on the algorithm outlined in Section 3, a simple steady state case was

| **Algorithm Input Variable** | **Value** | **Assumed Uncertainty** |
|---|---|---|
| Silicon Thickness | 0.001 meters | 3% |
| Adhesive Thickness | 15 micrometers | 3% |
| Polyimide Thickness | 15 micrometers | 3% |
| Black Surface Emissivity | 0.896 | 0.01 |
| Silicon Absorptivity | 8 | 5% |
| Polyimide/Adhesive Absorptivity | 7109.8 | 5% |
| Silicon Effective Emissivity | 0.847 | 0.01 |
| Polyimide/Adhesive Effective Emissivity | 0.666 | 0.01 |
| Effective Transmissivity | 0.445 | 0.01 |
| Effective Reflectivity | 0.427 | 0.01 |

**Table 4.3: Input Variable Assumed Uncertainties**

run at a single pixel while perturbing every input variable in the algorithm. From the resulting change in calculated heat flux, the $\partial \mathrm{F} / \partial \mathrm{X}_{\mathrm{i}}$ term was calculated. Table 4.3 summarizes the input variables that were significant contributors to total uncertainty and the assumed uncertainty values. The overall uncertainty was dominated by changes in the optical property values and each layer's thickness. Table 4.4 shows a summary of the estimated maximum error at several different heat flux values. As the heat flux increases so does the maximum error, but only slightly, resulting in lower percent errors at higher heat fluxes.

| Heat Flux (W/cm$^2$) | 4 | 3.5 | 3 | 2.5 | 2 | 1.5 | 1 | 0.5 |
|---|---|---|---|---|---|---|---|---|
| Max Error (W/cm$^2$) | 0.274 | 0.261 | 0.252 | 0.242 | 0.234 | 0.230 | 0.224 | 0.221 |
| Percent Error (%) | 6.8 | 7.5 | 8.3 | 9.7 | 11.8 | 14.7 | 21.0 | 47.8 |

**Table 4.4: Maximum Experimental Uncertainty**

# 5. Single Droplet Evaporation

The measurement technique described in the previous Sections 3 and 4 can be utilized to investigate the heat transfer characteristics of a single droplet evaporating from a heated surface. This phenomenon is well documented in the literature because it is important in several areas of engineering including fire protection and fundamental multiphase heat transfer models. Because single droplet evaporation is already well studied, and because a simple first law energy balance can be derived for each droplet,

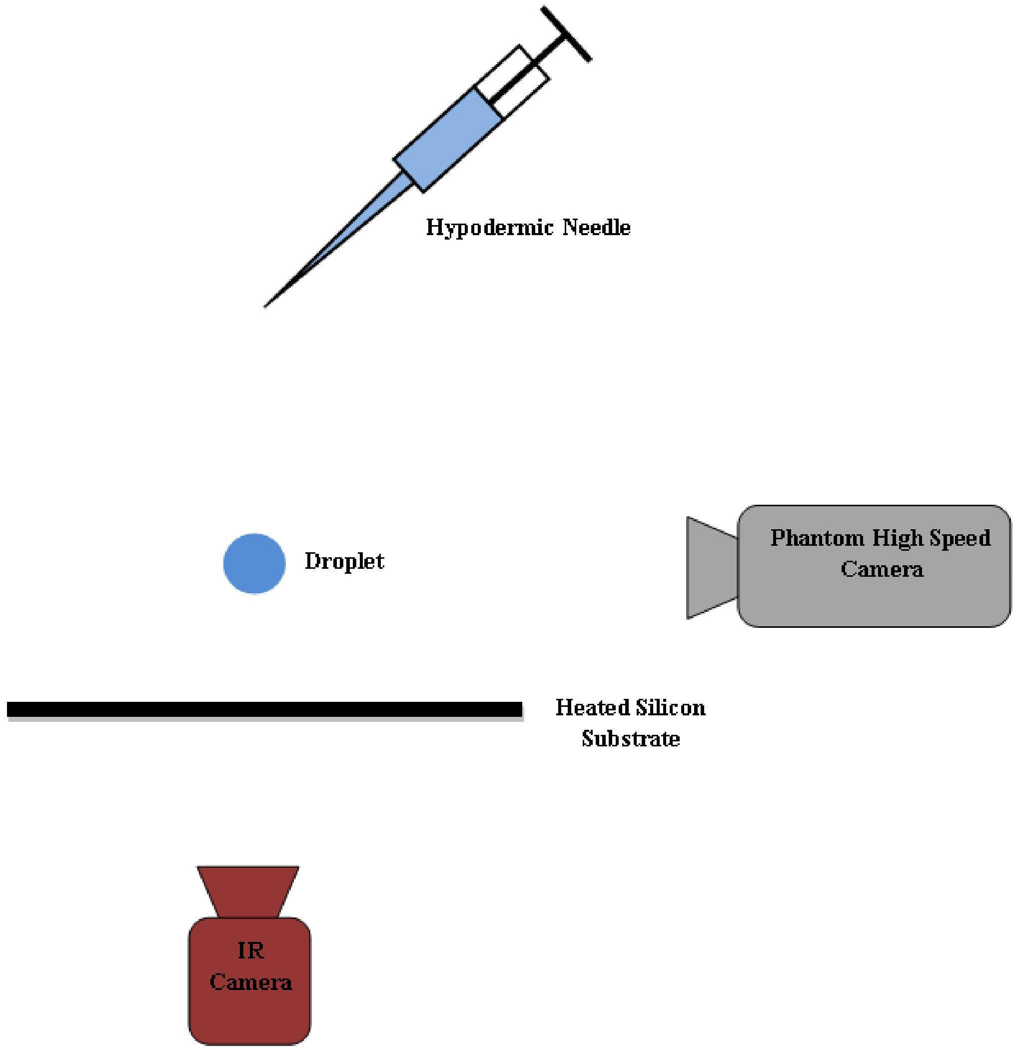

Figure 5.1: Droplet Evaporation Experimental Setup

this phenomenon can serve as an excellent validation of the infrared thermometry technique and analysis algorithm.

## 5.1 Experimental Setup

The single droplet evaporation experimental setup consisted of a silicon wafer lightly doped with phosphorous to a depth of approximately 1 micrometer. This dopant reduced the resistance of the wafer, allowing a low voltage (0-30 VDC) power supply to electrically heat it. Silver electrodes were deposited on the wafer to allow electrical

| Run | Surface Temp (°C) | Impact Velocity (m/s) | Droplet Diam (mm) |
|---|---|---|---|
| 1 | 51 | 0.53 | 1.27 |
| 2 | 55 | 0.53 | 1.27 |
| 3 | 56 | 0.53 | 1.27 |
| 4 | 60 | 0.53 | 1.27 |
| 5 | 66 | 0.53 | 1.27 |
| 6 | 70 | 0.53 | 1.27 |
| 7 | 74 | 0.53 | 1.27 |
| 8 | 76 | 0.53 | 1.27 |
| 9 | 80 | 0.53 | 1.27 |
| 10 | 66 | 0.97 | 1.27 |
| 11 | 74 | 0.97 | 1.27 |
| 12 | 56 | 0.97 | 1.27 |

**Table 5.1: Summary of Parametric Runs**

contact. Wafer surface temperature was controlled by varying the voltage applied by the power supply. The same polyimide-adhesive coating described in Section 4.3 was used to completely cover the top side of the wafer between the electrodes, while two small strips of the polyimide-adhesive coating were used on the bottom side of the wafer. These optically opaque layers allowed for temperature measurements over a wide area on the top side wafer, while also allowing temperature measurements of the bottom side of the wafer.

Droplets with a diameter of approximately 1 mm were deposited on the heated wafer from a hypodermic needle held at a fixed height above the surface. By varying the height of the needle, various impact velocities could be achieved in order to match those in the literature. The high speed digital infrared camera was positioned directly below the heated wafer, while a high speed visual camera (Vision Research Phantom 500) was situated to the side as depicted in Figure 5.1. This setup allowed the infrared camera to measure the instantaneous temperatures of the wafer, while the visual camera captured the droplet's impact velocity and diameter.

The fluid used was 3M's Performance fluid 5060 (PF 5060) which has a saturation temperature of 56 °C at one atmosphere. Wafer temperatures of between 56 and 80 °C were used with droplet impact velocities of 0.5 and 1.0 meters per second. Table 1 shows the temperatures, droplet diameters, and impact velocities used in each of the parametric runs.

## 5.2 Data Analysis

The optical and heat conduction model described in Section 3.3 was used as a basis for the data analysis algorithm. The bottom wafer temperature was calculated based solely on the black surface emissivity, reflectance and temperature of the surroundings. This temperature was calculated along two lines on either side of the “target” area for the droplets and then averaged at each time step. A plot of wafer backside temperature for several droplets is show in Figure 5.2 showing a slight decrease in temperature as the droplet evaporates but relatively steady temperature.

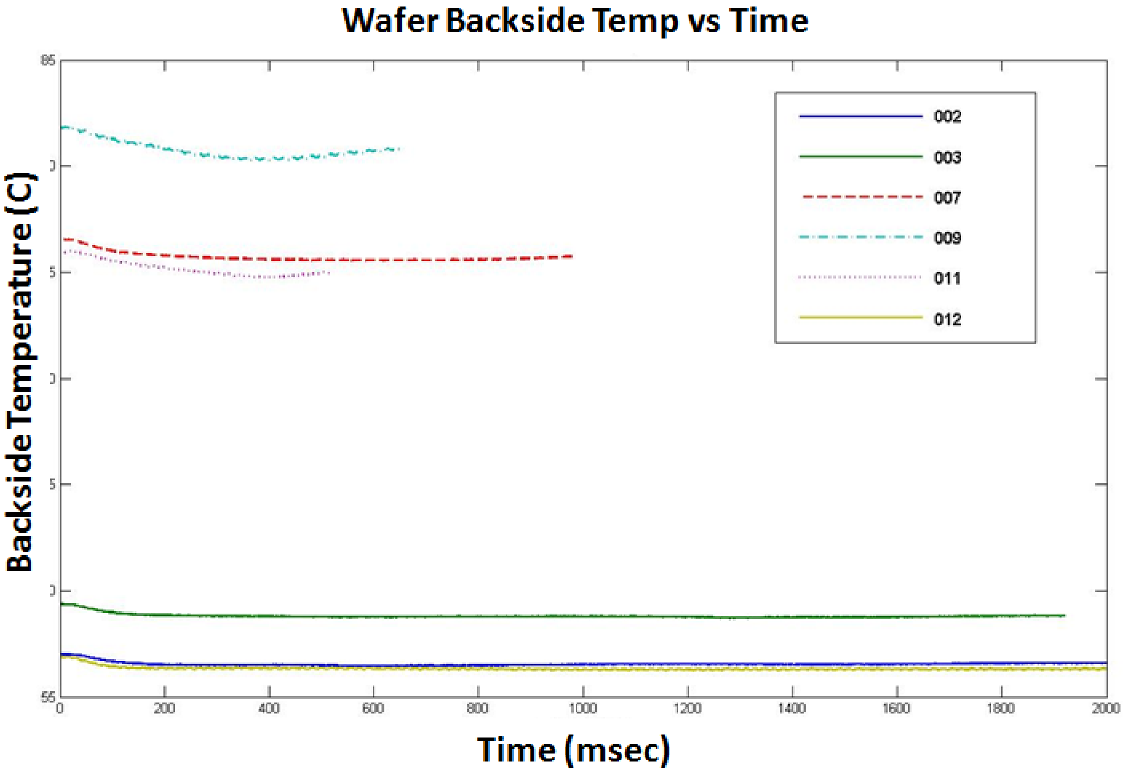

**Figure 5.2: Back Side Wafer Temperature vs Time for Each Droplet**

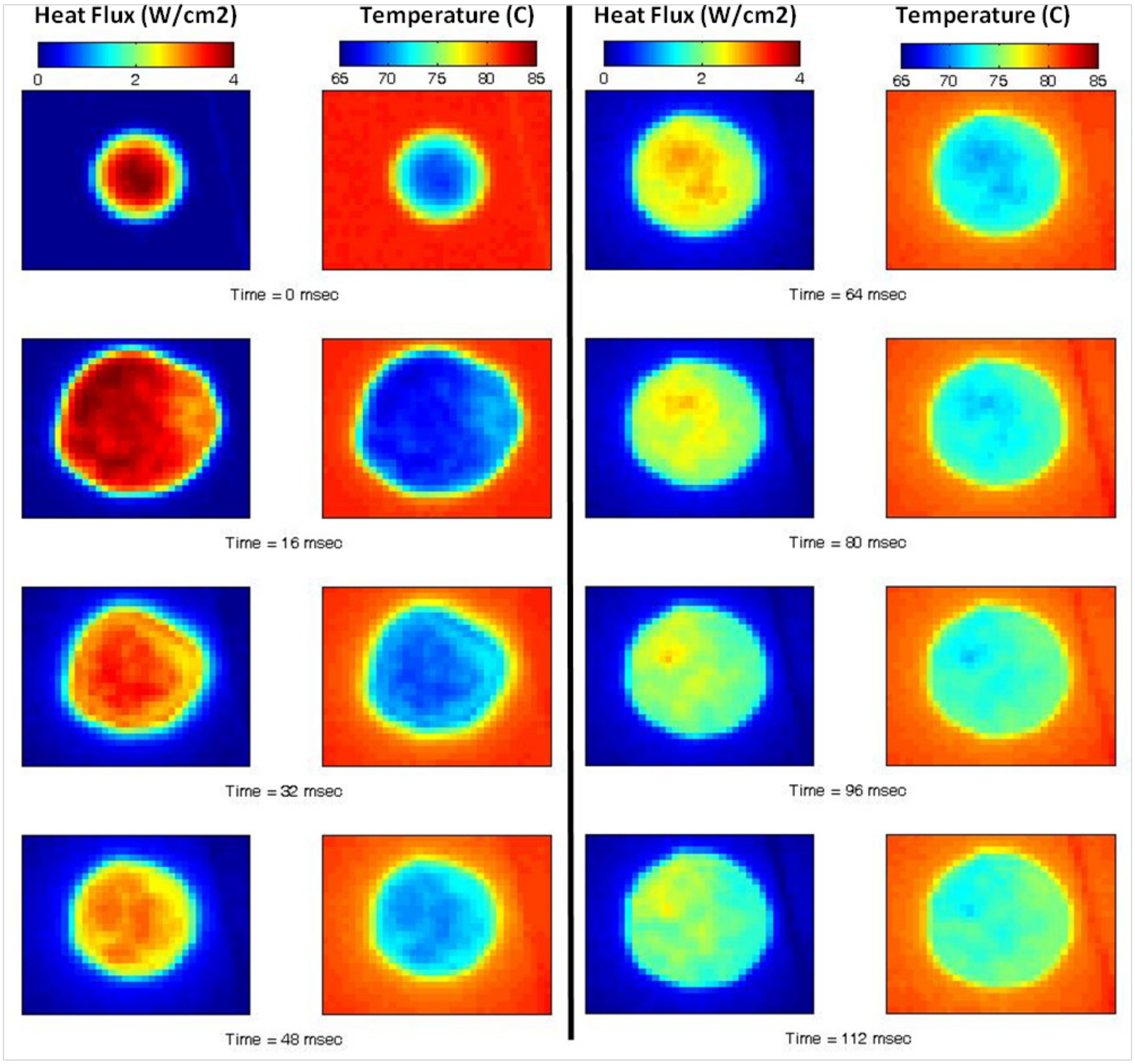

**Figure 5.3: Temperature and Heat Flux During Droplet Evaporation**

It can be assumed that immediately before the droplet impacts the surface, the entire wafer was in thermodynamic equilibrium, with the heat input balanced through losses due to natural convection in the air. This heat flux was small when compared to the fluxes involved in the droplet evaporation. The algorithm was used generate calibration data at each pixel which will yield zero heat flux at a time prior to the droplet's impact. This calibration data was then used for the remainder of the algorithm to ensure an accurate measurement of the temperatures and heat flux. The values of this calibration data ranged from 0.84 to 1.43. This variance was due to pixel to pixel error within the infrared camera, and due to non-uniform optical properties in the wafer.

Figure 5.3 shows several snapshots of the instantaneous heat flux and surface temperature from droplet nine. It is clearly evident that heat flux varied greatly across the diameter of the droplet, especially near the edge. The high heat fluxes on the droplet edge were due to the wetting or receding liquid-vapor line. The high resolution of the technique can be seen in Figure 5.3 where some nucleate boiling is evident near the droplet's center.

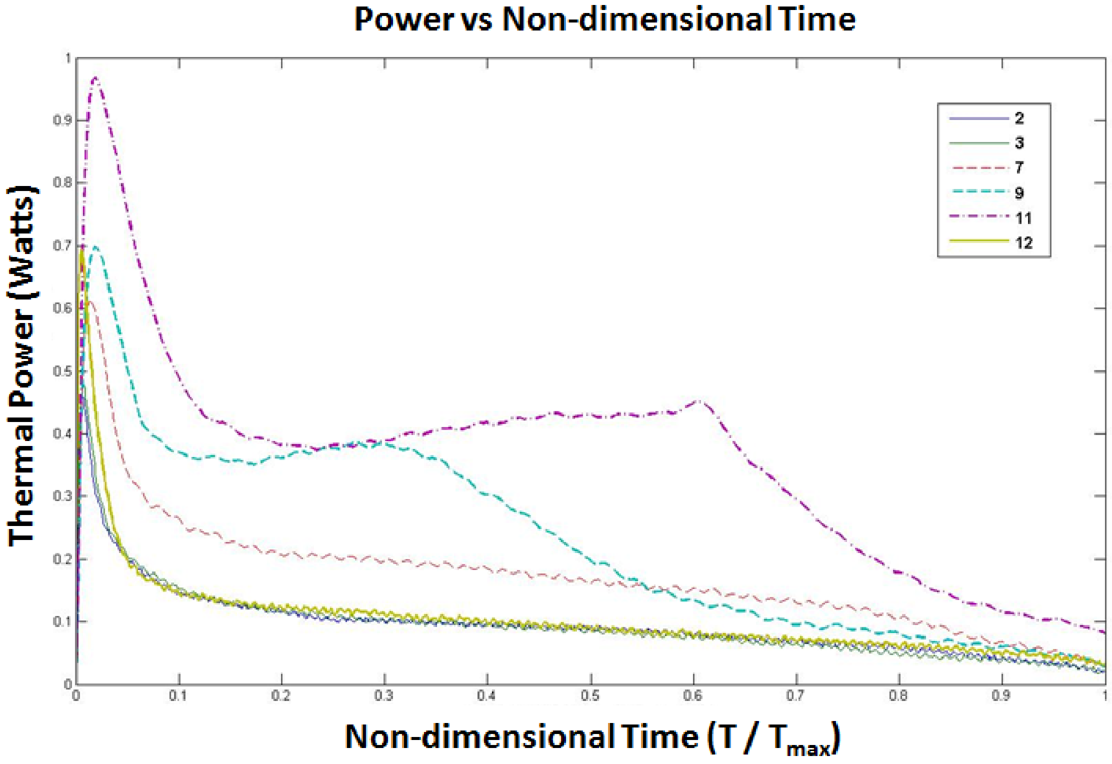

**Figure 5.4: Power vs Time of Droplet Evaporation at Various Surface Superheats**

Figure 5.4 shows the total thermal power in watts verses non-dimensional time for several different wafer superheats. The total power was calculated by integrating the heat flux at every pixel across the area of the wafer. Runs 12 and 3 are at the same temperature (saturation) but have different impact velocities (0.53 and 0.97 m/s), yet show little difference in heat transfer behavior. Runs 11 and 7 are also at the same temperature (76 °C) but having different impact velocities. Run 11, with a higher impact velocity, has a much larger initial thermal power due to the droplet spreading quicker at impact.

Although many qualitative observations may be made based on the droplet impact analysis, the real value of this study is to validate the infrared thermometry method and analysis algorithm. From the high speed camera side view, the droplet diameter could be measured quite accurately. In all 12 runs, the droplet diameter were 1.27 mm with an

| Run Number | Wafer Temp (°C ) | Measured Energy (joules) | Energy of Vaporization (joules) | Percent Difference |
|---|---|---|---|---|
| 2 | 56.5 | 0.226 | 0.220 | 3.06 |
| 3 | 58.8 | 0.182 | 0.220 | -17.07 |
| 7 | 75.6 | 0.169 | 0.220 | -22.92 |
| 9 | 80.7 | 0.151 | 0.220 | -31.26 |
| 11 | 74 | 0.185 | 0.220 | -15.8 |
| 12 | 56 | 0.228 | 0.220 | 3.69 |

**Table 5.2: Error Estimation of Droplet Evaporation**

uncertainty of 0.127 mm or 10%. Using a First Law energy balance, assuming no heat transfer to the ambient air, the thermal power transferred into the droplet could be compared to the energy needed to heat and vaporize the droplet. Table 5.2 shows the total power during droplet evaporation for several different velocities and superheats, the expected thermal power based on droplet diameter, and the percent difference between the two.

## 5.3 Comparison with Published Data

A similar study on single droplet evaporation was performed by Lee [34] using PF-5060, a heated surface and high speed photography. In this study the instantaneous heat flux was measured using a thin film micro-heater array allowing data to be collected

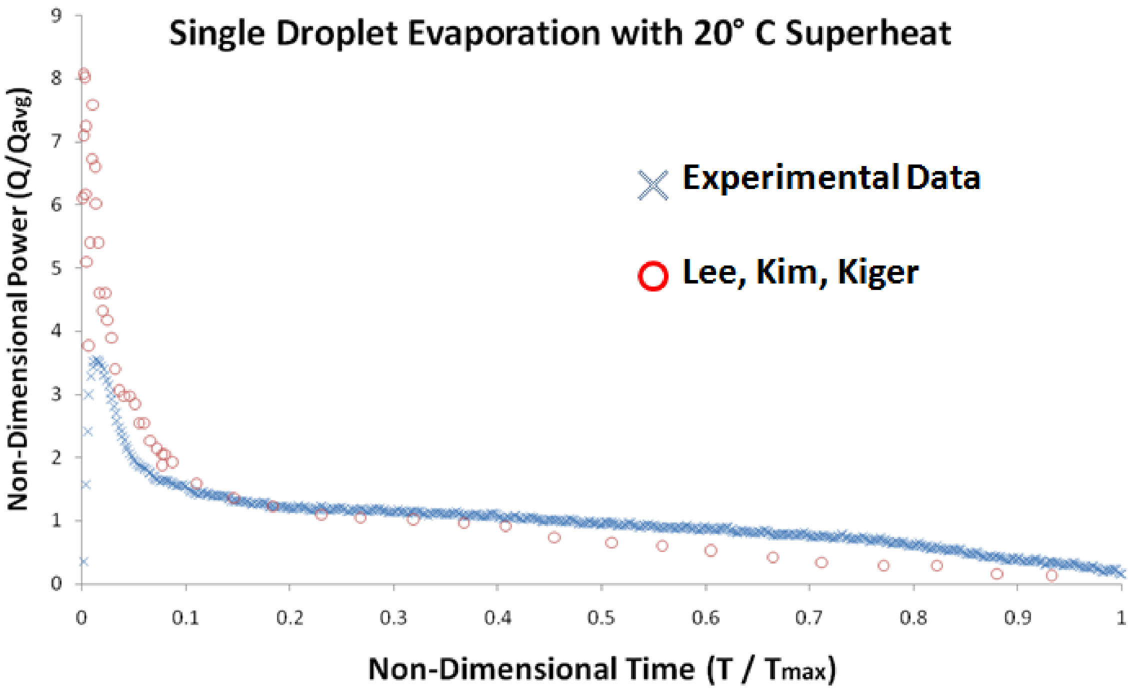

**Figure 5.5: Single Droplet Heat Transfer Comparison**

at 3000 Hz, but with potentially a lower special resolution than the present method. Similar droplet sizes, surface superheats, and impact velocities were used in Lee's study. To compare results, the total heat transfer rate over the entire heat was non-dimensionalized by average heat transfer rate, and time was non-dimensionalized by total time for evaporation, $T_{max}$. Figure 5.5 shows droplet 7 compared to Lee's data for the same superheat, and a slightly different impact velocity. The difference between the data at the initial time of impact could be due to the smaller droplet diameters used in Lee's study reaching saturation temperature quicker and nucleate boiling occurring more rapidly inside the droplet.

# 6. Single Phase Heat Transfer

A second validation for the experimental technique described in Section 3 was by collecting single phase heat transfer data. Forced convection heat transfer has been widely studied since the 1930's and experimental correlations are quite accurate for simple geometries. Comparisons to exact solutions to the heat diffusion equation for laminar flow forced convection can also be made using time averaged results from the experimental apparatus. For all earth gravity experiments the test apparatus was allowed to reach steady state with regards to flow, temperature, and power. Then 5 seconds of data were acquired at a frame rate of 200 Hz. The analysis algorithm described in Chapter 4 was used to calculate local heat flux, and temperatures at every axial position along the tube at time steps of 5 milliseconds. The time resolved data was then averaged over the 5 seconds of steady conditions. The ranges of experimental parameters covered are shown in Table 6.1. Because most heat transfer researchers report their data in non-dimensional terms or by the heat transfer coefficient, the time averaged heat flux data was converted to these variables. Heat transfer coefficients for boiling heat transfer are commonly defined as:

| | |
|---|---|
| **Absolute Pressure (kPa)** | **97.56** |
| **Flow Rate (ml/min)** | **25, 50, 75, 100, 150, 200** |
| **Reynolds Number** | **230, 460, 690, 930, 1390, 1860** |
| **Mass Flux, G, (kg/m$^2$s)** | **25, 50, 75, 100, 150, 200** |
| **Heat Flux, q", (w/cm$^2$)** | **0 - 5.25** |
| **Degrees Subcooling (°C )** | **0 , 5 , 15** |
| **Inlet Quality, X** | **0.15, 0.30, 0.50** |

**Table 6. 1: Experimental Parameters**

$$h_{2-phase} = \frac{q"}{T_{wall} - T_{sat}} \quad [6.1]$$

but for single phase forced convection:

$$h_{1-phase} = \frac{q"}{T_{wall} - T_{bulk}} \quad [6.2]$$

The bulk fluid temperature can be calculated based on the inlet temperature at the beginning of the test section, $T_{bulk}(0)$, axial position, z, mass flow rate, $\dot{m}$, and local heat flux, q" by:

$$T_{bulk}(z) = T_{bulk}(0) + \frac{\pi\, d\, \int_0^z q"(z)}{\dot{m}\, c_p} \quad [6.3]$$

Once the bulk fluid temperature reaches saturation temperature, any additional heat flux serves to change the bulk quality, x, of the fluid where:

$$x\,(z) = \frac{\pi\, d\, \int_{z\,at\,T=Tsat}^{z} q"(z)}{\dot{m}\, h_{fg}} \quad [6.4]$$

The fluid properties of PF-5060 were evaluated using the bulk fluid temperature and system pressure at every axial position. Equations from the manufacturer (3M) used to determine these properties are summarized in Table 6.2

| Fluid Property | Equation | Range of values |
|---|---|---|
| Density, ρ (kg/m$^3$) | $\rho = 1740 - 2.61(T)$ | 1594 - 1688 |
| Heat Capacity, $c_p$ (J/kg-K) | $c_p = 1014 + 1.544(T)$ | 1045 - 1101 |
| Thermal Conductivity, k (W/m-K) | $k = 0.060 - 0.00011(T)$ | 0.0538 - 0.0578 |
| Saturation Temperature, $T_{sat}$ (°C) | $T_{sat} = \frac{-1562}{\log\left(\frac{P}{10^{9.729}}\right)} + 273.15$ | 56.5 |
| Dynamic Viscosity, μ (N-s/m$^2$) | $\mu = -6(10^{-6})T + 7.8(10^{-4})$ | 0.000454 - 0.000663 |

**Table 6.2: Fluid Properties Summary**

## 6.1 Laminar Flow Forced Convection

For hydraulically and thermally developed laminar flow through round ducts, exact solutions to the heat diffusion equation are available that fully describe the heat transfer. The solution depends upon the boundary conditions used, resulting in a Nusselt number of:

$$Nu = \frac{h_{conv}\, d}{k} = 4.36 \qquad if\ q" = constant \tag{6.5}$$

$$Nu = \frac{h_{conv}\, d}{k} = 3.66 \qquad if\ T_{wall} = constant \tag{6.6}$$

The present experimental apparatus has neither constant heat flux nor constant wall temperature boundary conditions but something in between, so experimental Nusselt numbers between 4.36 and 3.66 would be expected. Figure 6.1 shows a plot of Nusselt number vs. axial position for a single mass flow rate (Reynolds number = 1800) and several different average heat fluxes. Two of the data series show a transition to nucleate boiling as seen by a sharp increase in the Nusselt number. All of the other series represent single phase forced convection or fully developed nucleate boiling. All of the series exhibit Nusselt numbers much larger than the expected Nu = 4.36. Secondly, there is a decreasing trend in Nusselt number with respect to axial position instead of a constant value as expected.

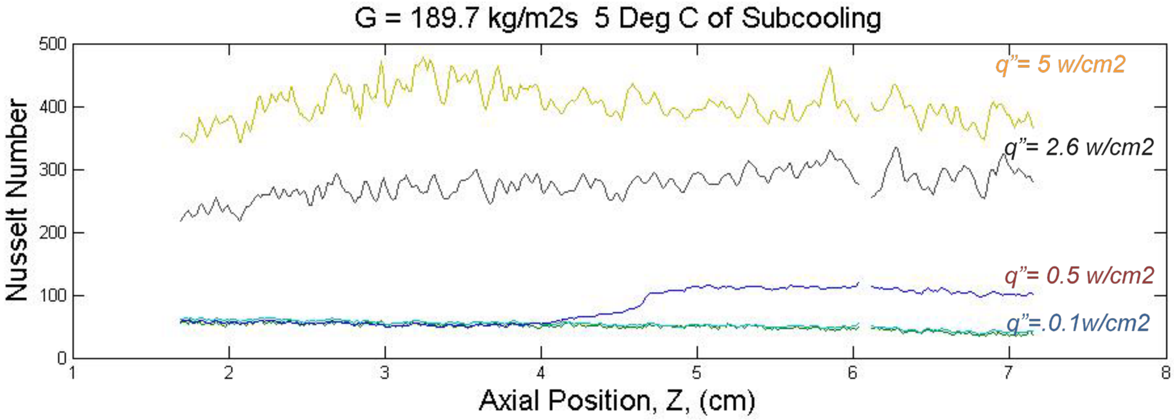

**Figure 6.1: Single and Two Phase Flow Local Nusselt Number vs. Axial Position**

Because the flow through the heated test section has not yet become thermally fully developed, the Nusselt number changes with respect to axial position and is higher than for the fully developed case. An exact solution to the thermally developing flow through a round duct was developed by Graetz [37] and later by Sellers, Tribus and Klien [38]. In place of the eigenvalue solution most engineers use curve fits to the exact solution. In both methods the axial position is non-dimensionalized by the Graetz number:

$$Gz = \frac{\left({}^{z}/_{d}\right)}{Pr\ Re} \qquad [6.7]$$

Shah's curve fit to Graetz's exact solution for an isothermal wall boundary condition is:

$$Nu(z) = \begin{cases} 1.302\ Gz^{-1/3} - 1 & if\ \ Gz < 0.01 \\ 3.657 + 6.874(10^3 Gz)^{-0.488} e^{-57.2Gz} & if\ \ Gz > 0.01 \end{cases} \qquad [6.8]$$

and for a constant heat flux wall boundary condition:

$$Nu(z) = \begin{cases} 1.302\ Gz^{-1/3} - 1 & if\ \ Gz < 0.00005 \\ 1.302\ Gz^{-1/3} - 0.5 & if\ \ 0.00005 < Gz < 0.0015 \\ 4.364 + 8.68(10^3 Gz)^{-0.506} e^{-41Gz} & if\ \ Gz > 0.0015 \end{cases} \qquad [6.9]$$

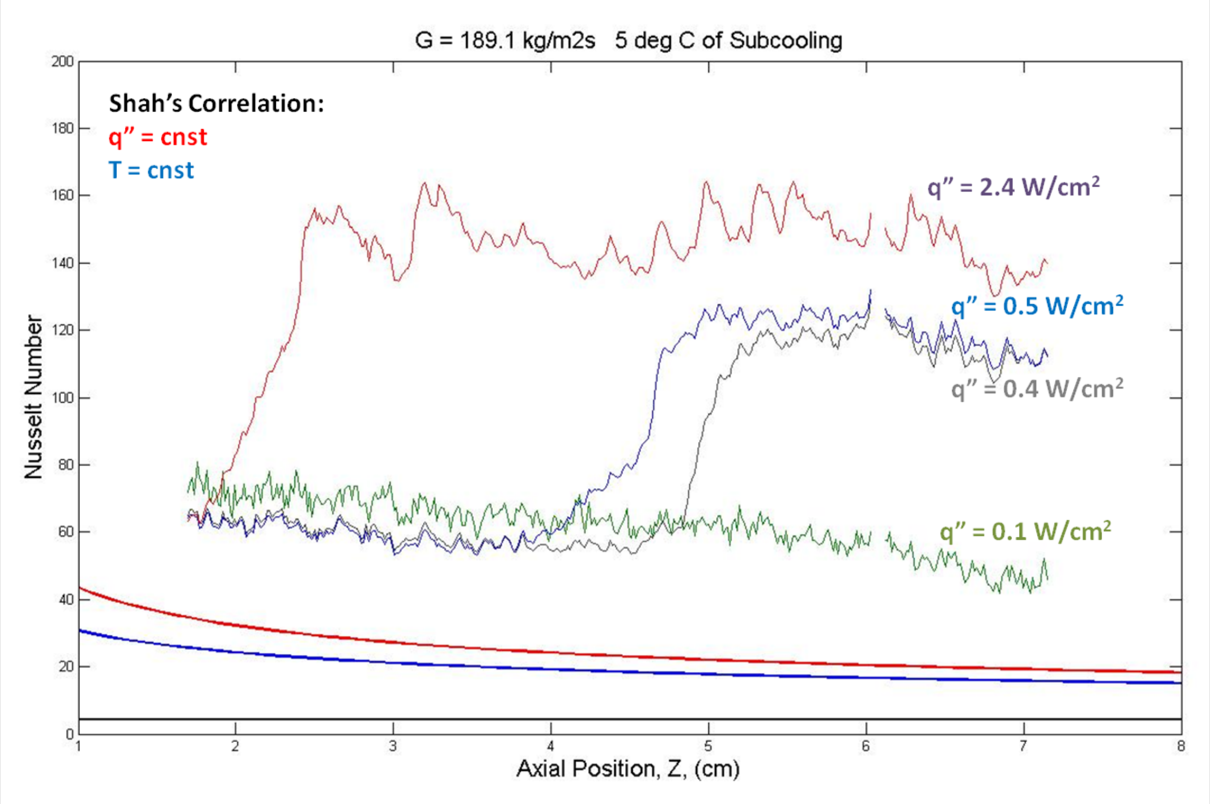

**Figure 6.2: Thermally Developing Flow Nusselt Number vs. Axial Position**

Figure 6.2 shows the same experimental data from Figure 6.1 along with Shah's solution for thermally developing flow. The trend in the Nusselt number agrees with the experimental data, but still under predicts the measured data. All of the solutions for thermally developing flow assume that the velocity profiles are already fully developed. For laminar flow developing from a uniform velocity profile the hydraulic entry length is:

$$\frac{z}{d} = 0.026\, Re_d \qquad [6.10]$$

For the Reynolds number in this study, the entry length ranges from 3.6 to 29 cm. The actual entry length is somewhat less than predicted by Equation 6.10 because the profiles are not developing from a uniform velocity but “re-developing” after an extremely sharp elbow upstream of the test section. Figure 6.3 shows the relevant dimensions of the test section and upstream piping.

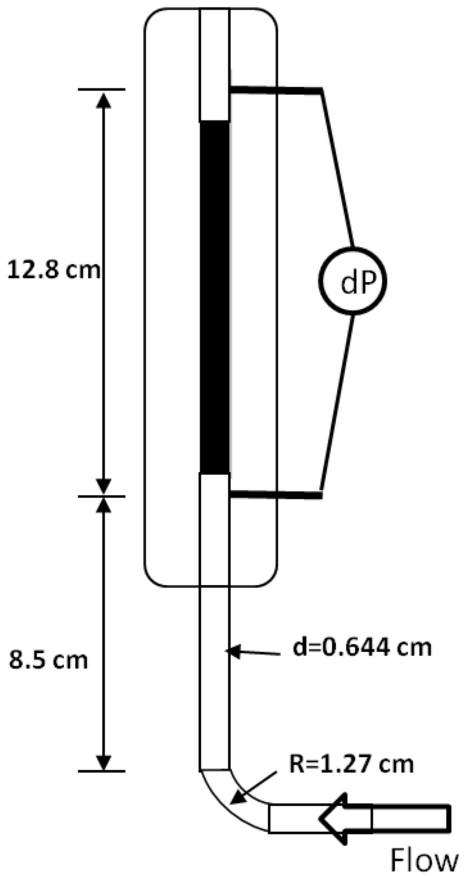

Figure 6.3: Test Section Dimensions

Experimental work by Ito [39] has shown that pipe bends effect the flow field and pressure drop both upstream and downstream of the elbow. How long these effects last depends upon radius of curvature in the elbow and Reynolds number. Ito's work deals only with turbulent flow and compares the local pressure drop to the total pressure drop across an elbow if the upstream and downstream pipes were of infinite length. Figure 6.4

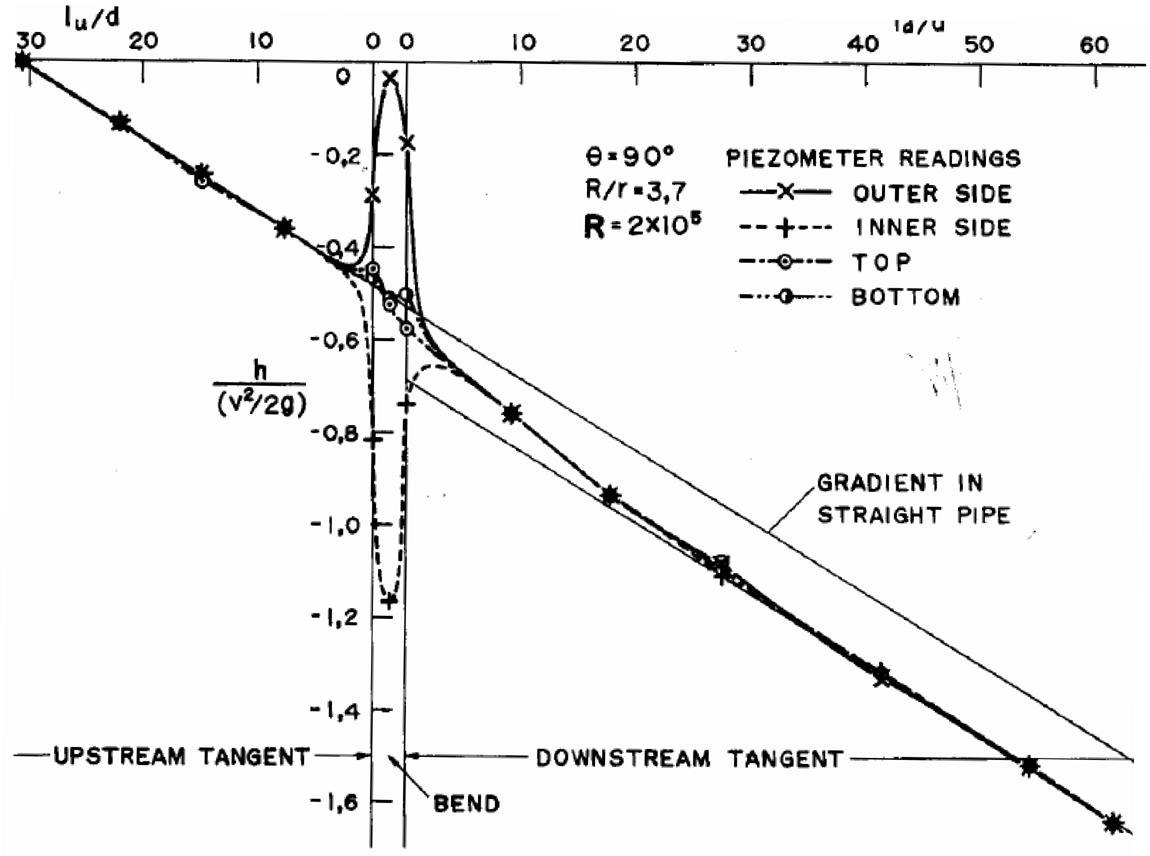

**Figure 6.4: Pressure Loss With a Pipe Elbow [from Ref 28]**

shows a plot of the pressure head loss through a 90 degree elbow. It is evident that at these conditions it takes approximately 30 diameters before the pressure drop per unit length becomes equal to that of normal pipe flow. From Ito's work the local pressure loss coefficient, k, can be determined as a function of the total loss coefficient, $k_t$. To supplement Ito's work, an ANSYS computational fluid dynamics solver was used to determine the centerline fluid pressure after a 90 degree elbow in the laminar regime. Figure 6.5 shows a plot of the change in pressure per unit length for three different laminar flow rates along with the pressure drop predicted by the laminar flow friction loss coefficient.

$$\frac{dP}{dZ} = \frac{V^2 f}{2\rho d} \qquad [6.11]$$

and

$$f = 64/Re \qquad [6.12]$$

Also shown on Figure 6.5 are the locations of the differential pressure transducer connections for reference. The computational model used a constant diameter (6mm) tube with a 10 cm entrance length, 90 degree elbow, and 1.5 meters of downstream piping. Convergence and mesh independence were verified to not affect the final solution. Table 6.3 shows a summary of the total elbow loss coefficient from the computational simulation as well as predicted by Ito's paper. Loss coefficients for

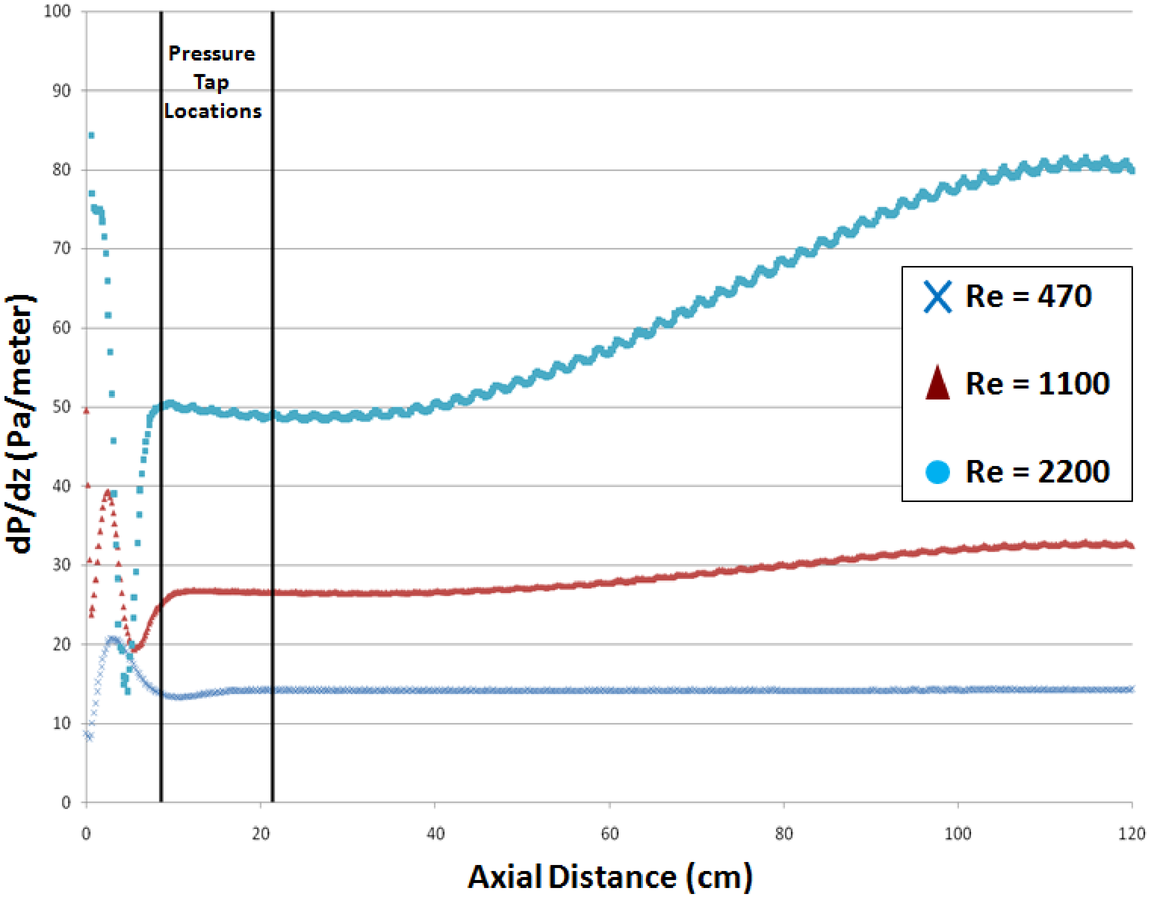

Figure 6.5: CFD Predicted Pressure Drop Downstream of a 90 Degree Elbow

laminar flow rates were included in Ito's paper based on other authors' experimental data. The turbulent flow case with a Reynolds number of 10,300 was simulated using a K-ε turbulence model, and Ito's predicted value was determined using his recommended method. Figure 6.5 shows that even at the lowest flow rates, the pressure drop is has not reached its predicted values, indicating that the velocity field is not yet fully developed. Ito's work along with the computational results provide an answer to why the fully developed thermal boundary layer solutions shown in Figure 6.2 do not agree precisely with the experimental data. Figure 6.4 shows a comparison of actual and predicted differential pressure drop over a wide variety of flow rates. The predicted pressure drop was calculated using Equation 6.11 and either a laminar of turbulent friction factor. Calculation of the turbulent friction was done using the Colebrook formula:

$$\frac{1}{\sqrt{\mathrm{f}}} = -2.0 \log\left(\frac{2.51}{\mathrm{Re}\,\sqrt{\mathrm{f}}}\right) \qquad [6.13]$$

In all cases the actual differential pressure drop was slightly higher than predicted due to the effects of the sharp upstream elbow in the flow.

| Re | Vel (m/s) | dP (Pa) | k elbow | k  predicted (Ito) |
|---|---|---|---|---|
| 470 | 0.0294 | 9.34 | 3.29 | 7.56 |
| 260 | 0.0147 | 4.23 | 5.01 | 8.82 |
| 1100 | 0.0589 | 22.57 | 2.67 | 6.93 |
| 1550 | 0.0884 | 39.83 | 2.32 | 6.43 |
| 2200 | 0.117 | 60.80 | 2.22 | 5.54 |
| 10300 | 0.589 | 446.58 | 0.73 | 0.439 |

Table  6.3: Elbow Loss Coefficient Comparisons

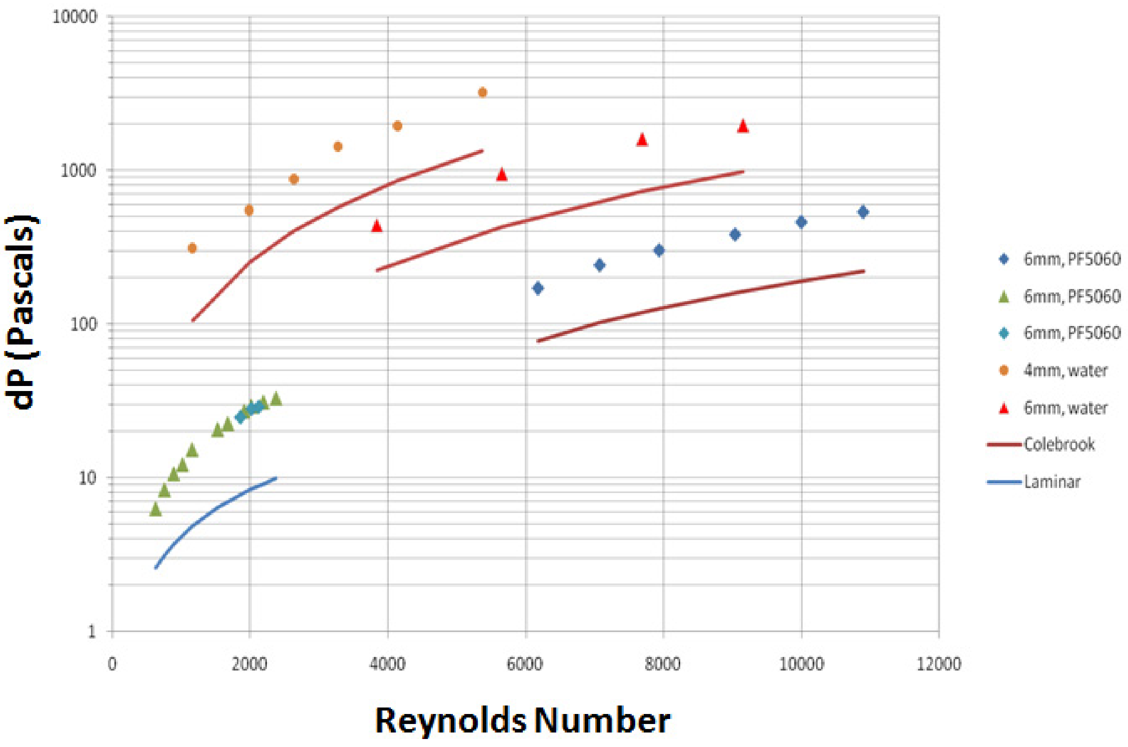

Figure  6.6: Actual Differential Pressure Drop Across the Test Section

# 7. Earth Gravity Flow Boiling

As a comparison to the numerous flow boiling correlations, some of which were overviewed in Section 2.1, the flight test rig was operated in the lab to obtain two phase data in earth gravity. The test setup described in detail in Section 4.5 was used to obtain heat flux and temperature measurements within the silicon test section. A wide range of parameters summarized in Table 7.1 were used.

| | |
|---|---|
| Average Heat Flux (W/cm$^2$) | 0 – 5.25 |
| Flow Rate (ml/min) | 25, 50, 75, 100, 150, 200 |
| Mass Flux (kg/sm$^2$) | 25, 50, 75, 100, 150, 200 |
| Reynolds Number | 230, 460, 690, 930, 1390, 1860 |
| Degrees Subcooling (°C) | 0, 5, 15 |
| Pressure (kPa) | 97.56 |

**Table 7.1: Summary of Experimental Parameters**

## 7.1 Time Resolved Results

Data was taken with flow, temperature, and power in steady state. After a three to five minute wait to ensure equilibrium, 5 seconds of data were captured at a frame rate of 200 Hz. After the data analysis algorithm was completed on each video file, the visual frame is combined with plots of the instantaneous heat transfer rate, outside and inside temperature, and local heat transfer coefficient where:

$$h = \frac{q''}{(T_w - T_{sat})} \qquad [7.1]$$

Figure 7.1 shows a single frame of this combined plot. The average heat transfer coefficient over the period of time when constant power was being supplied is also shown. The movies generated frame by frame show in excellent detail how heat transfer varies with boiling flow structure. It is also evident from Figure 7.1 where the flow transitions to nucleate boiling at an axial position of 2.5cm, both visually and by inspecting the heat flux plot. Figure 7.2 shows a single frame at a lower mass flow rate where the entire test section is boiling. A uniform heat flux and heat transfer coefficient is seen, and the time variation of these parameters is quite small.

Figure 7.3 shows the flow transitioning to slug flow along the final 2-3 cm of axial length. As the vapor slugs cover portions of the tube, it is evident that the local heat flux drops significantly. The portions of the tube that are then rewetted around the slugs exhibit higher than average heat transfer. When seen in frame by frame, the time variations in heat transfer can be seen to exactly match with the vapor slugs passing.

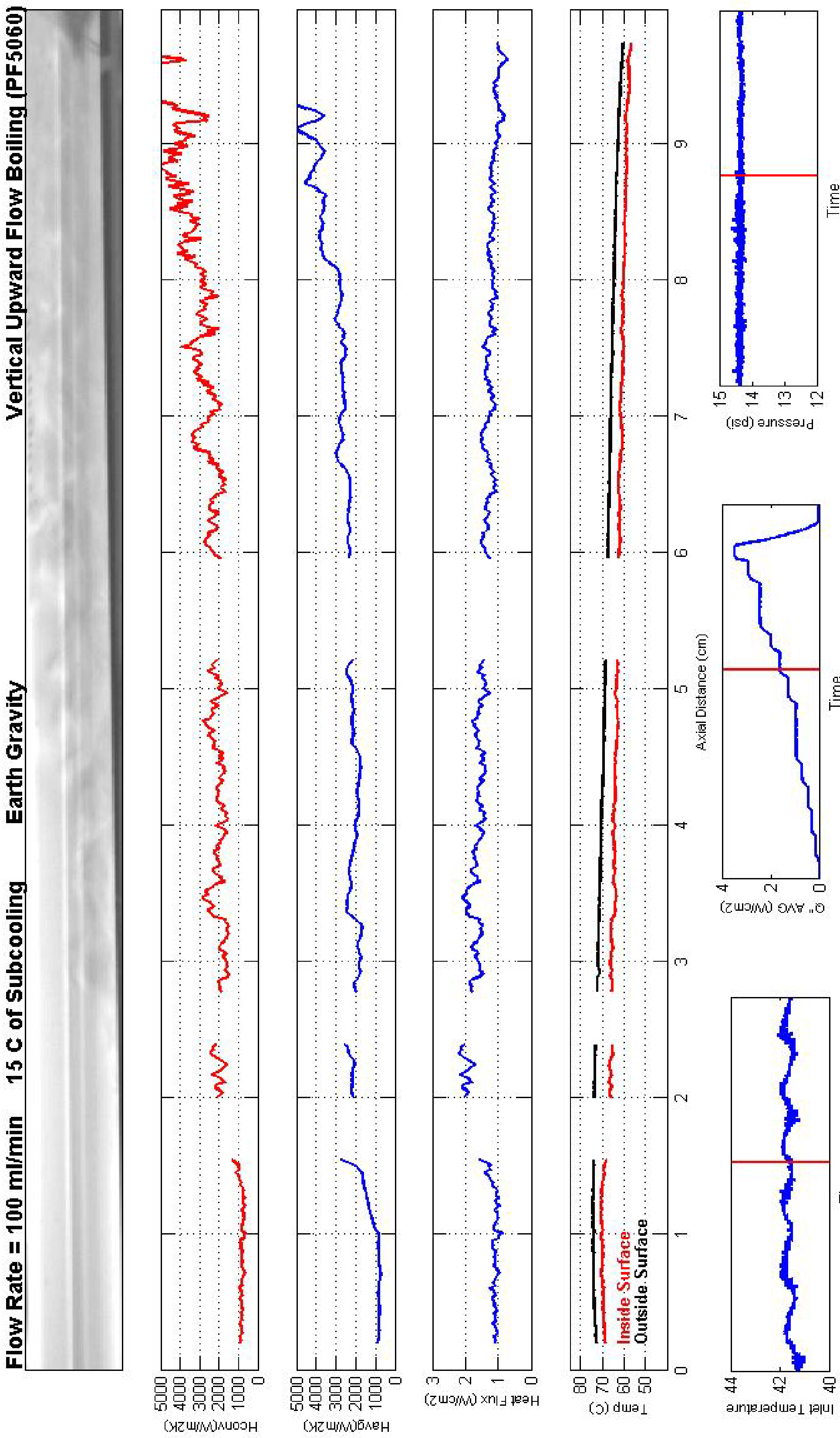

Figure 7.1: Single frame captured at 200 Hz showing ONB

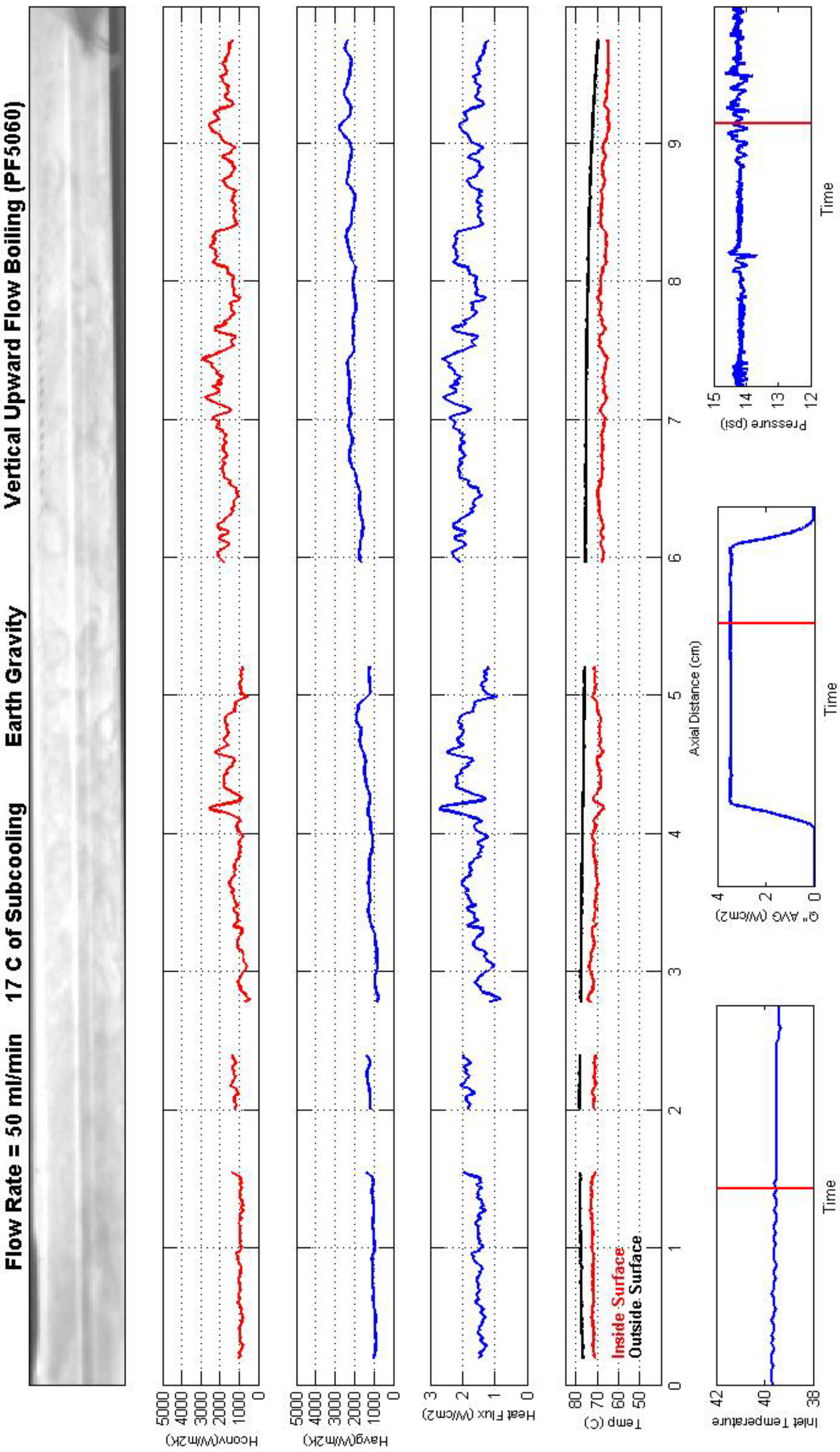

Figure 7.2: Single frame captured at 200 Hz showing fully developed boiling

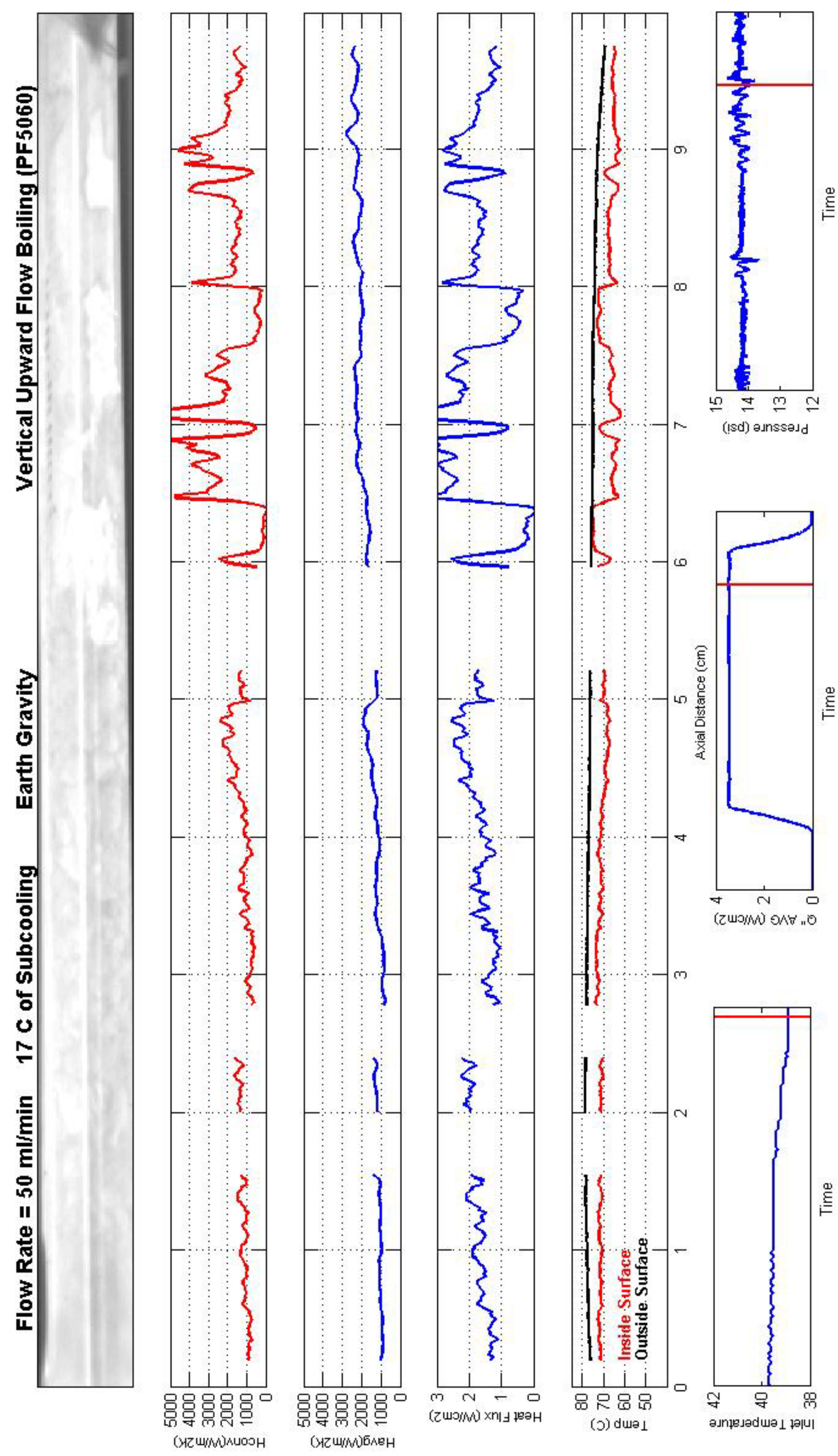

Figure 7.3: Single frame captured at 200 Hz showing slug flow

## 7.2 Time Averaged Results

Nearly every published empirical correlation considering flow boiling attempts to predict the average heat transfer characteristics of the flow. To compare the present experimental data to these correlations, time averaged data must be used. In all cases, the flow was allowed to reach equilibrium after temperature or power parameters were changed. Then the heat flux, local heat transfer coefficient and surface temperatures were averaged over 5 seconds or 1000 frames of video. A more detailed look at exactly

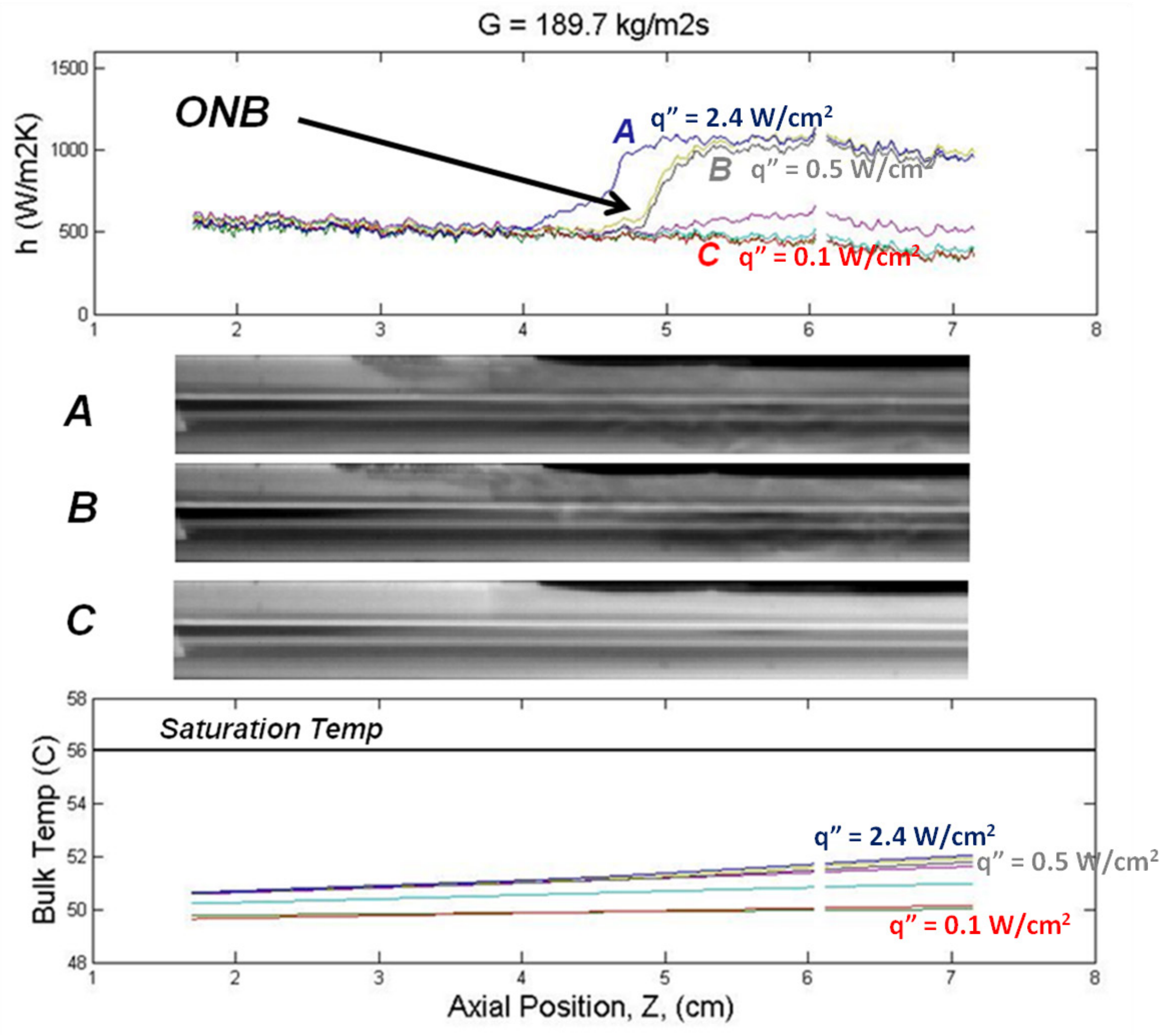

**Figure 7.4: Transition to Nucleate Boiling**

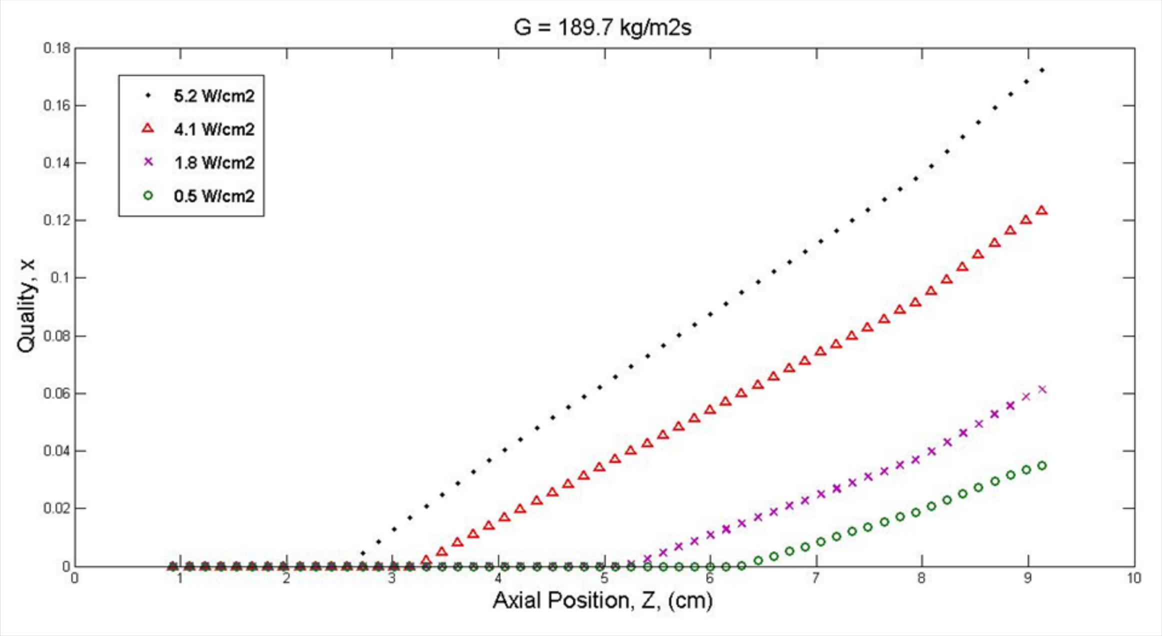

Figure 7.5: Quality vs. Axial Position

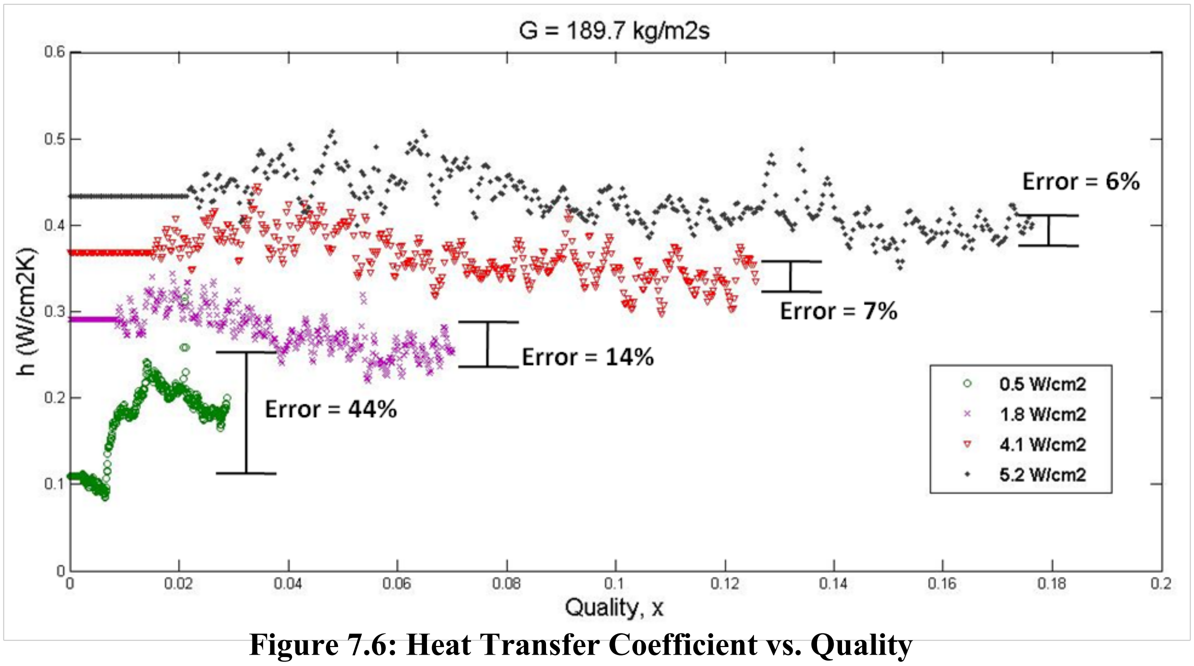

Figure 7.6: Heat Transfer Coefficient vs. Quality

what is happening in the heated test section can be found by plotting heat transfer data verses axial position. Figure 7.5 and 7.6 shows the local heat transfer coefficient as well as the bulk fluid temperature at 7 different average power settings. In all cases the bulk temperature is below the saturation temperature, but boiling still occurs in several of the plots. The onset of nucleate boiling (ONB) point can be seen by the jump in heat transfer coefficient as well as on the still frame images. In frames A and B the ONB point appears at a position of Z = 2.8 cm, but the jump in heat transfer coefficient occurs at Z =5 cm. This discrepancy can be explained by the fact that the nucleation site does not occur at the same radial position as where the temperature measurements are being made. In fact, in all of the experiments it seems that the initial bubble nucleation site is at a radial position 90 degrees offset from the camera face, and 90 degrees from the temperature measurement point. This is where the two pieces of polyimide tape overlap creating a roughness that enhances nucleation. The axial position where the heat transfer coefficient jumps corresponds to where the boiling becomes rapid enough to envelope the entire circumference of the tube. The bulk temperature and fluid quality can be found by numerically integrating the heat flux using Equations 6.3 and 6.4. A plot of the fluid quality verses position for several different average power settings is shown in Figure 7.5. Figure 7.6 shows the local heat transfer coefficient verses fluid quality. The lowest and highest average heat fluxes are labeled. There are many overlapping data points at a quality of x = 0 because the flow is single phase for the first several centimeters of axial position. Figure 7.6 indicates that the heat transfer coefficient is relatively constant regardless of fluid quality. This has been seen by numerous researchers, and is true as long as the boiling flow regime does not drastically change. In all of the cases plotted in

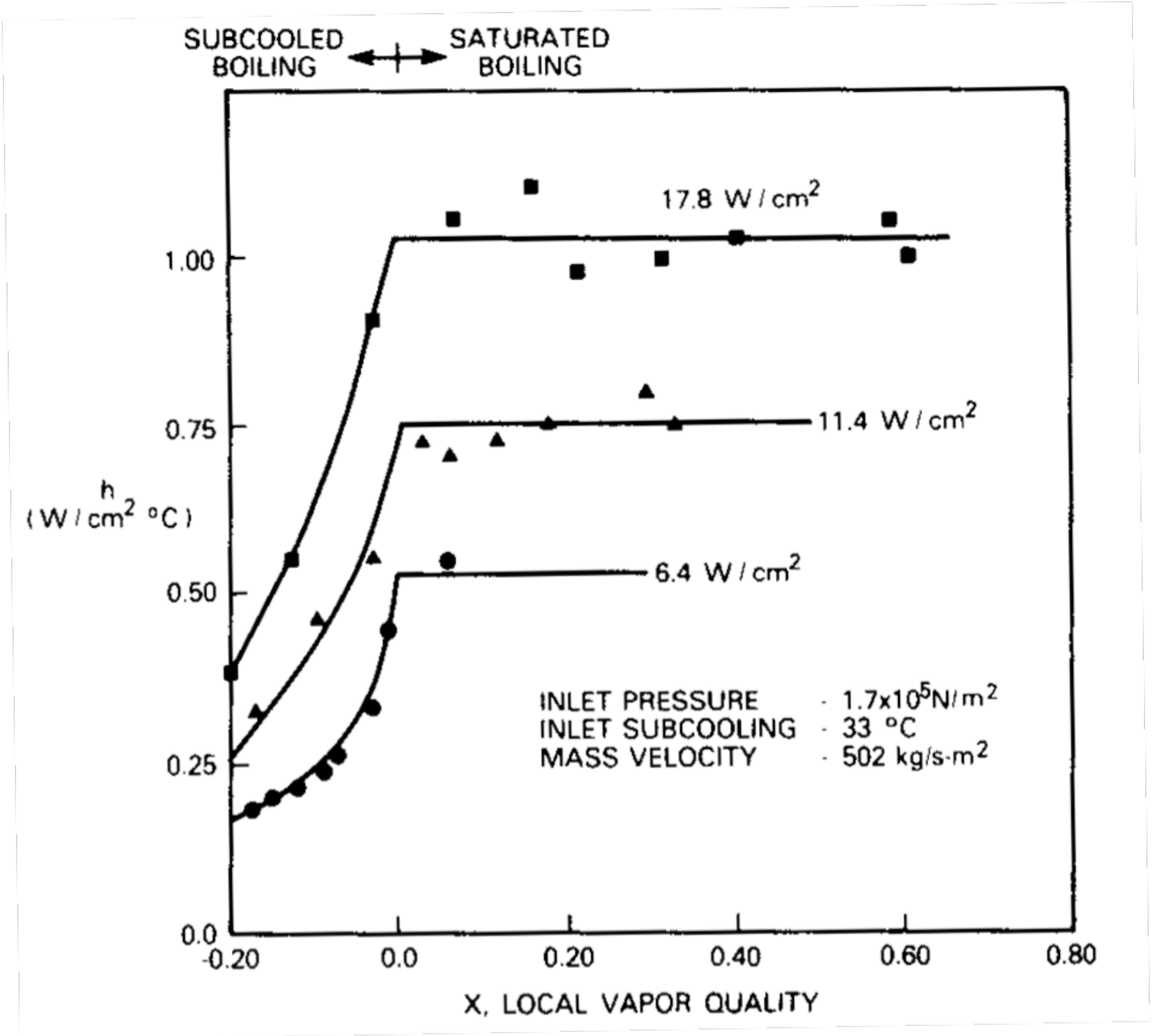

**Figure 7.7: Heat Transfer Coefficient vs. Quality from Lazarek [30]**

Figure 7.4 the heat flux is low enough that the flow remains in the nucleate boiling regime at all times. Figure 7.7 shows a plot from Lazarek's experimental work on flow boiling and pressure drop. His research used R-113 as a working fluid over heat fluxes and flow rates very similar to those in the present study. A similar trend to that of Figure 7.5 can be seen, where an increase in average heat flux increases the heat transfer coefficient, while there is no change as quality increases. This phenomenon occurs because as the average power increases the wall temperature does as well. Higher wall temperatures activate more nucleation sites and the heat transfer is enhanced.

## 7.3 Comparison to existing correlations

Comparisons to other experimental work and accepted heat transfer correlations have been calculated to validate the present study. While most existing experimental data was taken at only several points within the flow geometry, this study's method resolves the heat transfer characteristics at every axial position. To compare this data to other

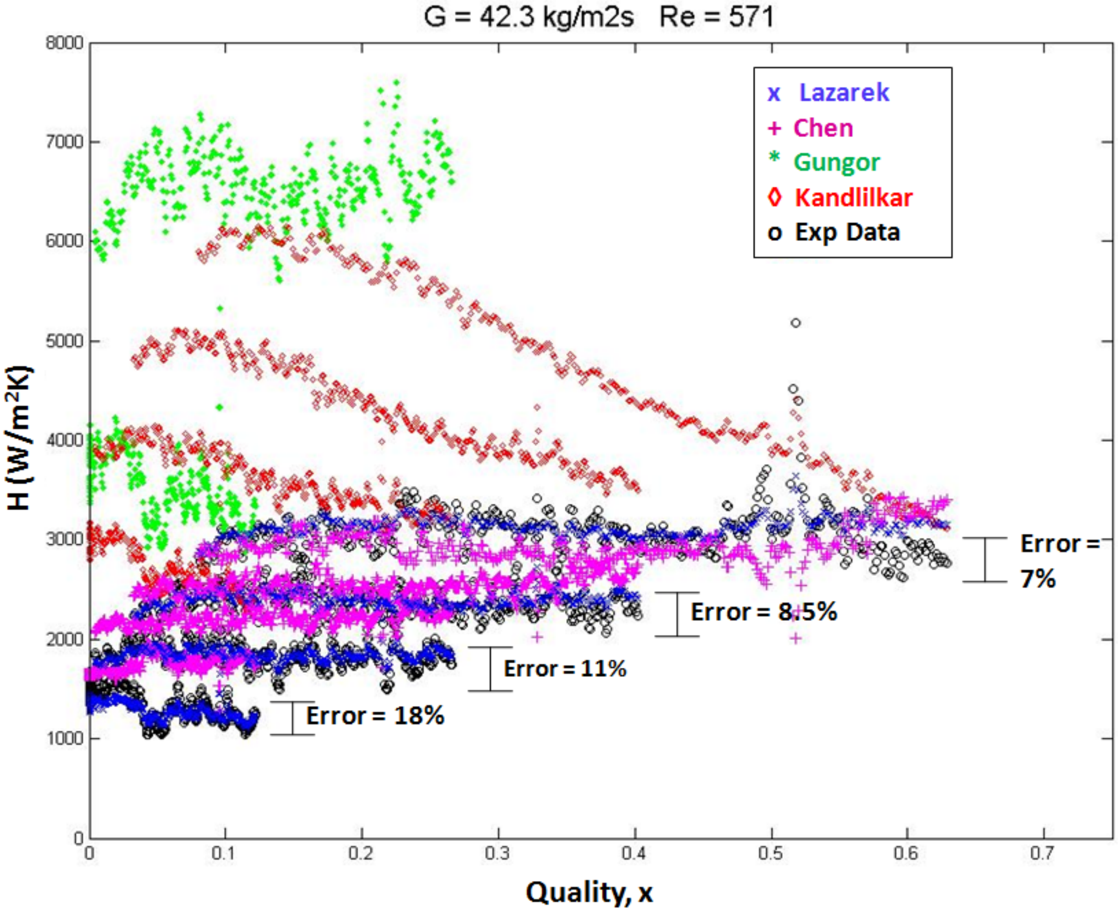

**Figure 7.8: Comparison of Experimental Data to Published Correlations for Nucleate Boiling**

published correlations, the local heat transfer coefficient was calculated based on experimental parameters. The resulting plot, shown in Figure 7.8, contains data points for each correlation corresponding to an actual experimental data point.

Lazarek's [41] correlation for fully developed convective boiling seems to best agree with the experimental data. His correlation is a power law formula with the form:

$$\mathrm{Nu} = \frac{\mathrm{h\,k}}{\mathrm{d}} = 30\ \mathrm{Re}^{0.857}\mathrm{Bo}^{0.714} \qquad [7.2]$$

where, Bo, is the boiling number:

$$\mathrm{Bo} = {}^{q''}\!/_{\mathrm{G\,h_{fg}}} \qquad [7.3]$$

The good agreement with correlation is not surprising due to the fact that Lazarek used R-113 as a working fluid and covered a range of heat and mass fluxes similar to those in our experiment as summarized in Table 7.2.

| | **q" (W/cm$^2$)** | **G (kg/m$^2$s)** | **Re** | **Pressure (kPa)** | **Fluid** |
|---|---|---|---|---|---|
| **Experimental** | 0.1-5.5 | 25-200 | 230 - 1860 | 101 | PF-5060 |
| **Lazerak** | 0.14 - 3.8 | 125-750 | 860-5500 | 130-410 | R-113 |

**Table 7.2: Comparison of Experimental Parameters**

Chen's correlation [42] has been used extensively since the 1970's for industrial applications and is often cited by current researchers. His correlation is a superposition type with the assumption that the heat transfer is a combination of a forced convection and modified pool boiling term, where:

$$h = S\,h_{\text{pool}} + F\,h_{\text{convection}} \tag{7.4}$$

and, F, the forced convection two phase multiplier is:

$$F = \left(\frac{1}{X_{tt}} + 0.213\right)^{0.736} \tag{7.5}$$

where $X_{tt}$ is the Martinelli parameter, and, S, the pool boiling suppression factor is:

$$S = \frac{1}{1 + (2.53x10^{-6})Re^{1.17}} \tag{7.6}$$

Any acceptable pool boiling correlation can be used to calculate $h_{pool}$.

Gungor and Winteron [43] proposed a modified version of Chen's correlation based on experimental data from a number of fluids including water, R-11, R-12, R-22, R-113, and R-114 in vertical upward flow. Their method uses Cooper's nucleate pool boiling correlation:

$$h_{\text{pool}} = 55p_r^{0.12}(-0.4343ln(p_r))^{-0.55}M^{-0.5}q''^{0.67} \tag{7.6}$$

where, M is the molecular weight, and $p_r$ is the reduced pressure. Gungor's modified two phase multiplier and pool boiling suppression factor are:

$$F = 1 + 24000Bo^{1.16} + 1.37\left(\frac{1}{X_{tt}}\right)^{0.86} \tag{7.7}$$

$$S = [1 + (1.15 \times 10^{-6})F^2Re^{1.17}]^{-1} \tag{7.8}$$

Kandlikar's [9] correlation as outlined in Chapter 2 was also included as the most modern widely used flow boiling correlation.

Shah's [44] correlation, originally a graphical chart method, must be solved via a series of implicit expressions. Shah's method calculates a heat transfer coefficient for nucleate boiling and convective boiling and chooses the larger of the two.

$$h = \max\,[h_{cb}, h_{nb}] \tag{7.9}$$

The convective boiling heat transfer coefficient is a modification of the Dittus-Boelter forced convection expression:

$$h_{cb} = {}^{1.8\,h_l}\!/_{Co^{0.8}} \tag{7.10}$$

where:

$$h_l = 0.023 Re^{0.8} Pr^{0.4} \frac{k}{d} \tag{7.11}$$

and:

$$Co = \left(\frac{1-x}{x}\right)^{0.8} \left(\frac{\rho_g}{\rho_f}\right)^{0.5} \tag{7.12}$$

The nucleate boiling heat transfer coefficient depends upon the magnitude of the boiling number, Bo and convection number, Co:

$$h_{nb} = \begin{cases} 230 h_l Bo^{0.5} & if\ \ Co > 1\ and\ Bo > 0.0003 \\ h_l(1 + 46Bo^{0.5}) & if\ \ Co > 1\ and\ B < 0.0003 \\ h_l\left(F_s Bo^{0.5} \mathrm{e}^{2.74\mathrm{Co}-0.1}\right) & if\ \ 1 < Co > 0.1 \\ h_l\left(F_s Bo^{0.5} \mathrm{e}^{2.74\mathrm{Co}-0.15}\right) & if\ Co < 0.1 \end{cases} \tag{7.13}$$

and:

$$F_s = \begin{cases} 14.7 & if\ Bo > 0.001 \\ 15.43 & if\ Bo < 0.001 \end{cases} \qquad [7.14]$$

A second way to compare all of the previously described correlations to the experimental data is by plotting every experimental data point with the predicted heat transfer coefficient. Figure 7.9 shows the predicted verse actual heat transfer coefficient along with 25% error bands. Clearly Lazerak's correlation performs the best over the range of experimental parameters used which are restricted to the fully developed boiling portion of the boiling curve. None of the data taken in the current study approached the critical heat flux point.

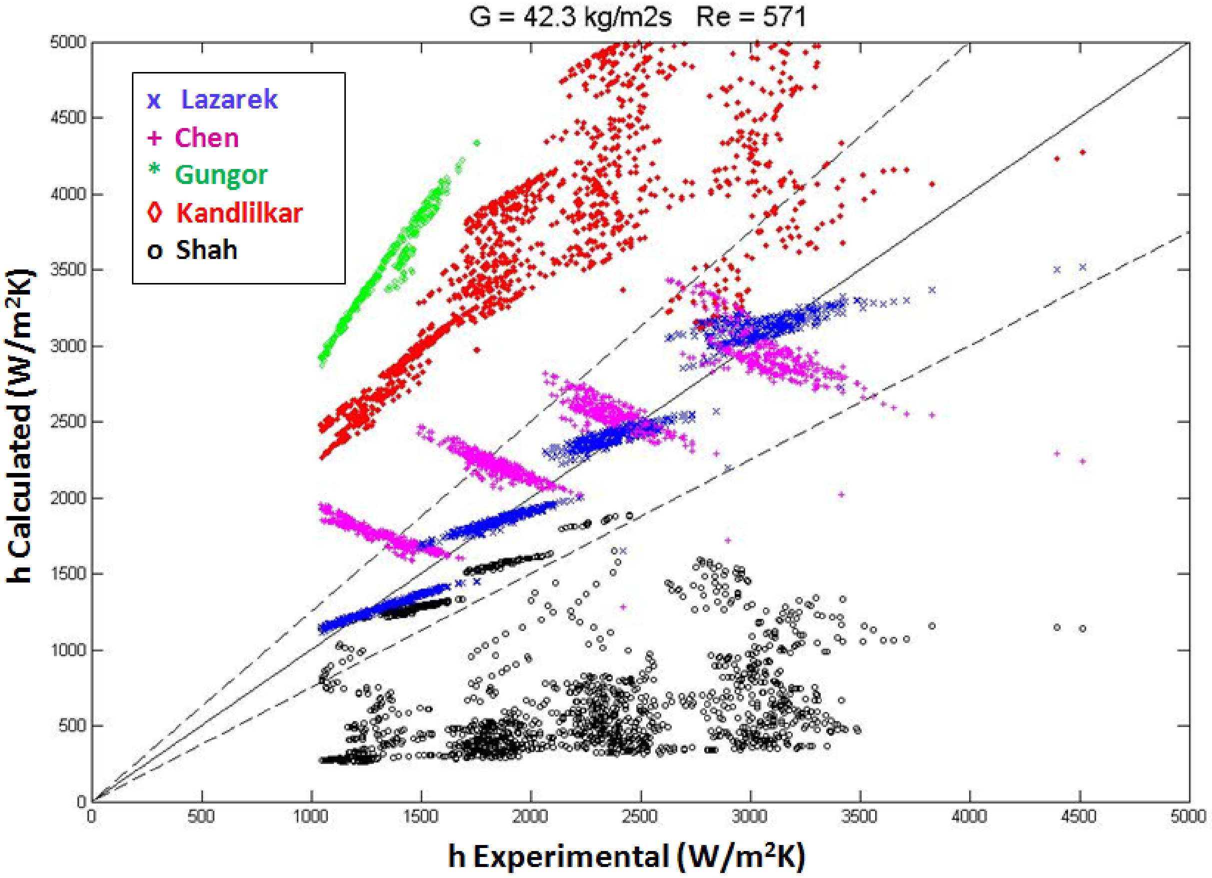

**Figure 7.9: Predicted vs. Experimental Heat Transfer Coefficient**

Lazarek's correlation is based on experimental data taken using R-113 over a range of flow rates and heat fluxes very similar to the test matrix in the current study. Lazarek's studied the boiling phenomenon over the first third of the boiling curve, covering only the fully developed nucleate boiling regime. Because the correlation was based on a narrow set of data very similar to the experimental data in the current study, it fits the data quite well. As the flow regime starts to transition to slug or annular flow Lazarek's correlation starts to show less agreement with the data. Kandlikar's and Gungor's correlations are meant to be used over a wide range of boiling conditions from the onset point up to the critical heat flux condition. Because of the wide range of use for these correlations, the error can be expected to be greater. The apparently excellent fit of Lazarek's correlation should not be expected at higher heat fluxes approaching the critical heat flux point.

# 8. Conclusions and Further Study

The goal of this study was to develop and validate a new technique to simultaneously measure the local heat transfer while visualizing the boiling phenomena.

The first significant contribution of this study was the development of the theory needed to properly analyze the optics of the multilayer. The optical model detailed in Section 3.2 coupled with the algorithm described in Section 3.3 are unique in the field of infrared thermometry. Detailed information about the construction of the multi-layer as well as both thermal and optical properties must be known for the technique to produce accurate results. A significant portion of this study was spent taking accurate measurements of these optical properties using the actual instruments used during the flow boiling experiments.

A second contribution of this study, was development of the unique multi-layer construction method needed to add the optical layer and power electrodes to a radial geometry. Much trial and error in the University of Maryland's FabLab was needed to successfully make electrical connections to a round silicon tube. The thermal deposition and silicon doping methods developed in this study are already being used by other researchers on different geometries.

Zero gravity data taken over the course of over 22 hours of flight time in NASA's parabolic aircraft proved that the technique and hardware satisfactorily perform even in a demanding, non laboratory environment. Analysis of this data is ongoing, and future flights using the experimental apparatus described in Section 4 are planned.

Perhaps the most important contribution of this study was the validation of the technique against existing earth gravity data. The validation techniques outlined in Sections 5 and 6 indicate that the infrared thermometry technique and associated analysis algorithm can produce accurate results. Single phase heat transfer results were similar to exact solutions for laminar forced convection when entry length effects were accounted for. Time averaged flow boiling data was compared to a variety of accepted experimental correlations in Section 7. Excellent fit with the current study's data was found with at least one of the correlations over the flow parameters tested.

Based on these results it can be shown that the technique in this study can yield accurate measurements of the time varying, local heat flux and temperature in the geometry tested. Qualitative observations on the boiling flow regime are also possible thanks to the flow visualization ability. Future work using this technique will enable researchers to combine detailed quantitative data with visualizations of the flow regime. Existing models that rely on the type of boiling regime to determine the correct correlation can be tested much more accurately. Additionally, models such as Thome's [19], which attempt to describe boiling heat transfer at the single bubble or slug level can be tested with accurate time resolved data. Time varying heat flux data may also be used to investigate possible correlation between heat transfer rates and the frequency of the transient phenomena.

The current study has adequately qualified the experimental apparatus and technique. Further analysis of earth gravity flow boiling data could prove valuable as a comparison to other researchers' mechanistic models. Variable gravity flow boiling data currently available necessitates further analysis so that quantitative comparisons between heat transfer rates and flow regimes can be made.

# Appendix 1: Calibration data

Laboratory calibrations were performed on all applicable sensors prior to and additionally, in some cases, after data was taken.

## A1.1: Differential Pressure Transducer

A Validyne Model P55D-1-N-1-36-S-4-A, Serial number 137881 was used to measure the differential pressure across the test section via two 0.8 mm diameter pressure taps. The transducer came factory calibrated with a DC output voltage of 0-5 volts corresponding to a pressure range of 0-5 psid. This pressure range was too large for the actual experimental pressures so a replacement diaphragm was used to change the range to ±0.5 psid. A calibration was performed using a manometer filled with both water and

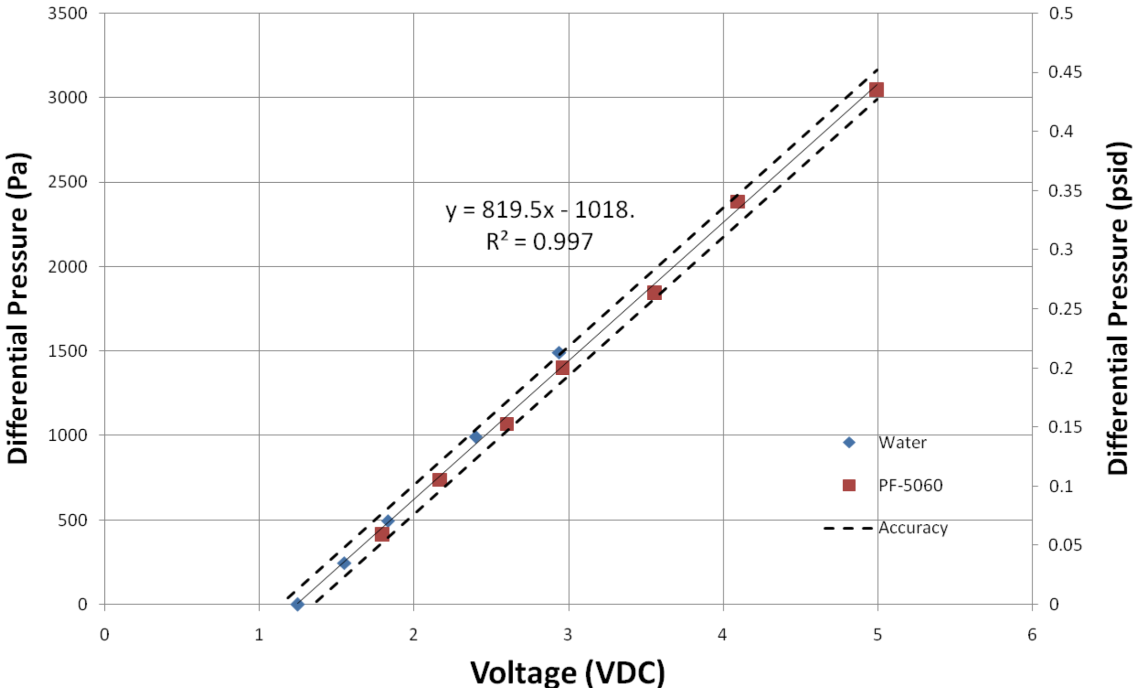

**Figure A1.1: Differential Pressure Transducer Calibration**

PF-5060. Figure A.1 shows the calibration curve along with the voltage to pressure curve fit and the transducers accuracy of ±0.25% of full scale. Voltage was measured using the data acquisition system as well as a Agilent Model 34401a bench top multimeter.

## A1.2: Flow Meter

An Omega Model FLR1000 pin-wheel type flow meter is used to measure the volumetric flow rate of refrigerant through the test apparatus. The flow meter came factory calibrated using a 0-5 VDC output. The calibration was checked using a positive displacement gear pump and graduated cylinder. Voltage was measured using the data

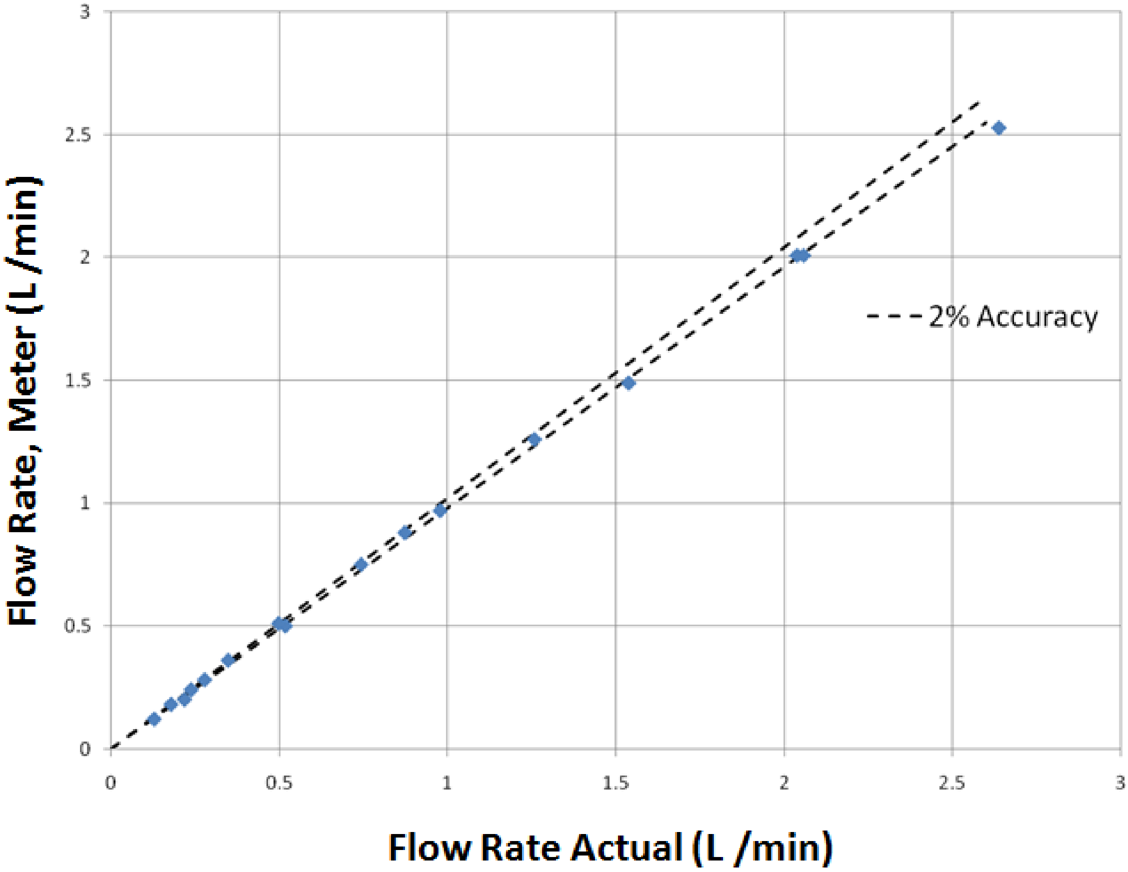

**Figure A1.2: Flow Meter Calibration**

acquisition system along with an Agilent Model 34401a bench top mulitmeter. Figure A1.2 shows the actual and measured flow rate along with 2% accuracy bounds.

## A1.3: High Voltage Power Supply

An AMTEK Model XTR-600-1.5 direct current power supply was used to apply voltage to the silicon test section. Because the silicon tube is lightly doped, yielding good optical characteristics, the resistivity was quite high. Resistivity ranged from 10 - 100 Ω-cm, giving a tube resistance of approximately 1200 Ω including contact and lead resistance. To drive enough current a high voltage power supply must be used, but voltage measurements were taken using a data acquisition system with an input range of 0-5 VDC. To accomplish this as well as allowing current measurements, a voltage

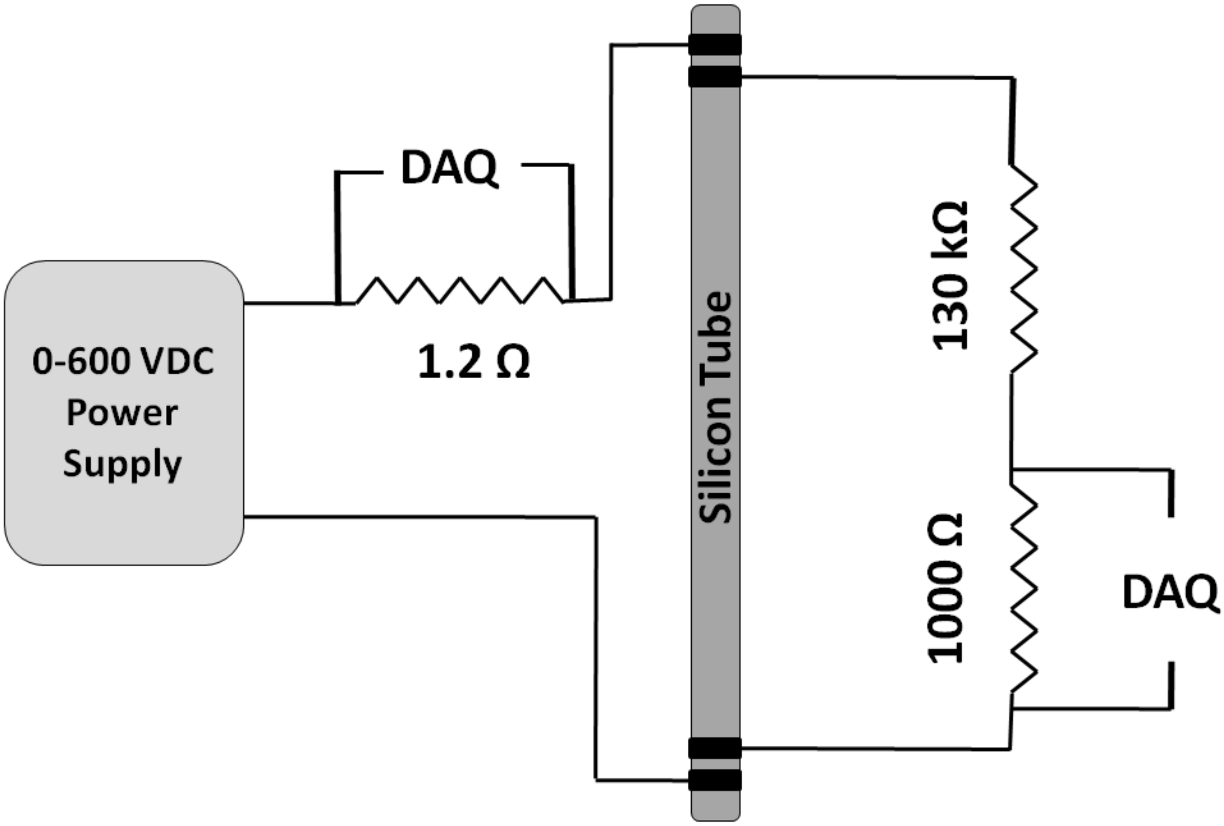

**Figure A1.3: Voltage Divider Schematic**

divider network along with a current measuring resistor were used along with the built in digital readouts on the power supply. Figure A1.3 shows a schematic of the voltage divider and current resistor connections. To validate the system, two Agilent Model 34401a bench top mulitmeters were used to simultaneously measure current and voltage during laboratory testing. As expected the resistance of the tube changes with the power applied due to temperature changes and the large temperature coefficient of resistivity of silicon. Figure A1.4 shows the silicon tube resistance verses the tube voltage. Resistance increases because at higher voltages the silicon is warmer and therefore more resistive. Both the minimum and maximum flow rates were plotted which correspond to the high and low limits of tube temperature at each voltage. Because during test runs and calibration the actual voltage applied by the power supply was known and always slightly higher than the tube voltage, the contact and lead resistance to the silicon tube could be calculated. The contact resistance was calculated by:

$$R_{contact} = {(V_{supplied} - V_{tube})}/{I} \tag{A.1}$$

Figure A1.6, a plot of the calculated contact resistance as a function of supplied voltage, showed little change as a function of voltage and therefore temperature.

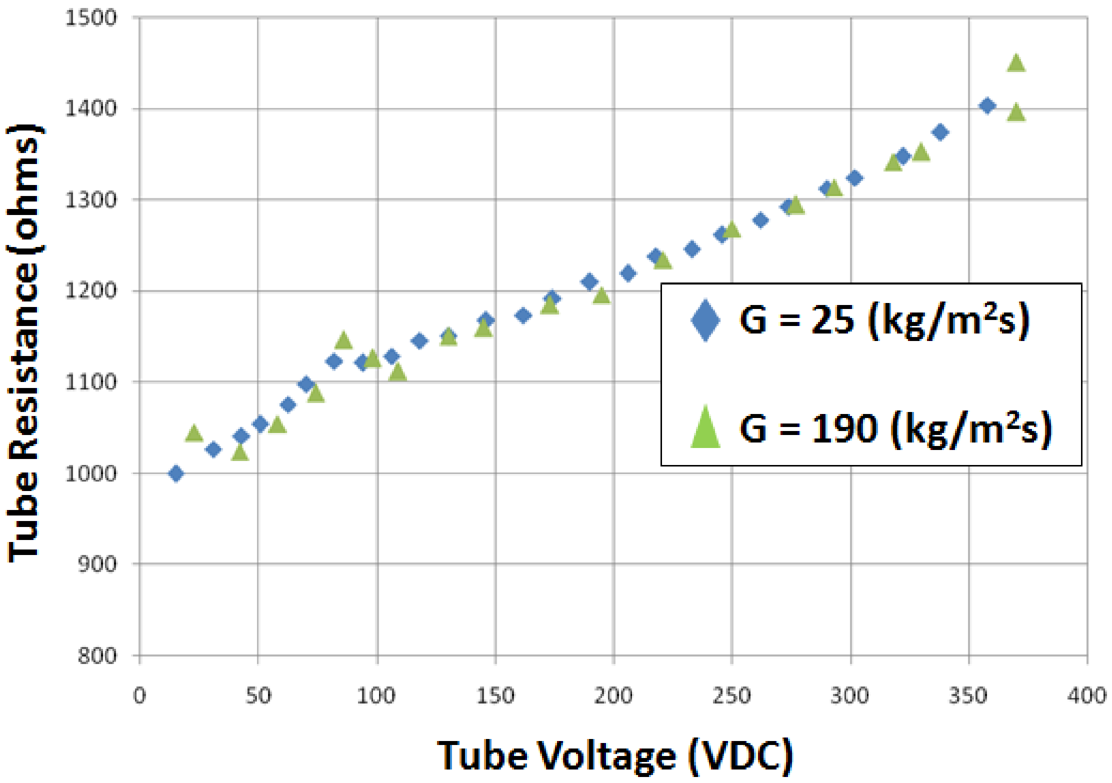

Figure A1.4: Silicon Tube Resistance

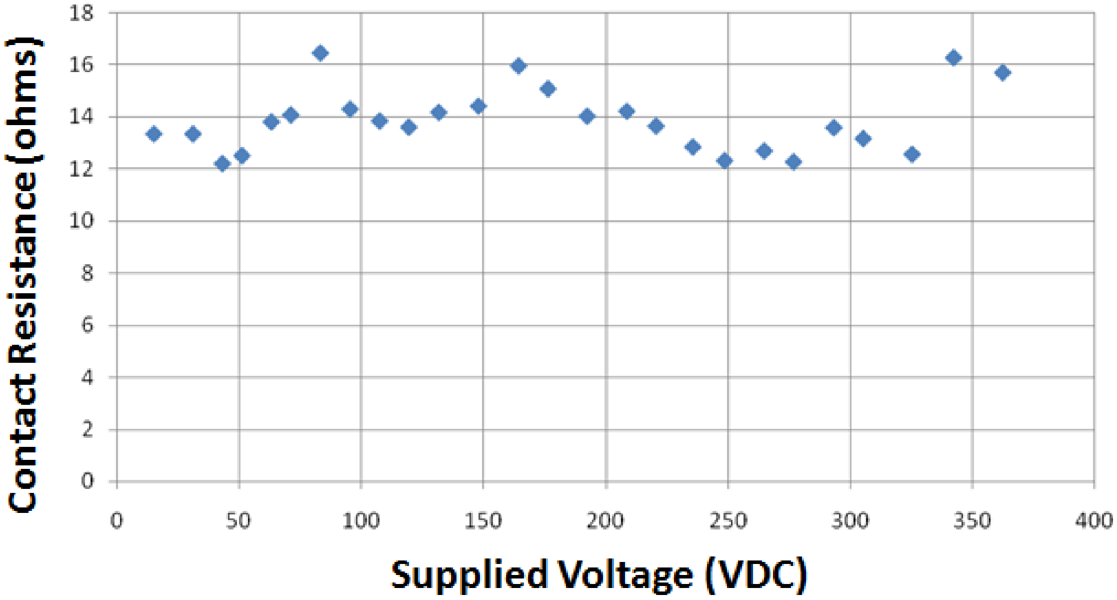

Figure A1.5: Silicon Tube Contact Resistance

## A1.4: Pre-Heater

The fluid pre-heater was fabricated by brazing together two 6 foot lengths of 3/8 inch outside diameter 316 Stainless steel tubing and then trimming to a final length of 2.9 meters. Using tubing with a wall thickness of 0.3 mm gave an overall resistance of 0.25 Ω. The driving voltage for most of the earth gravity tests was 0 -12 volts AC, provided by a high power variable AC transformer (VARIAC) and 10:1 step down transformer. Current was measured using a Tektronix P6021 indirect clamp on current probe and voltage measured with an Agilent model 34401A benchtop multimeter. Because alternating voltage was used to power the pre-heater, and the electrical system consisted of a number of inductors, a check of the true power factor was made to ensure the pre-heater could be treated as a purely resistive element and impedance ignored. Power factor measurement was accomplished by using a Tektronix Model TDS1000 oscilloscope to monitor the current and voltage. Any non purely resistive electrical system operating with alternating current will exhibit a lag between the voltage and current waveform. Utilizing an oscilloscope to trace both waveforms allowed the lag angle to be determined and the power factor, PF, where:

$$\mathrm{PF} = \cos(\theta) = \cos\left(\frac{\Delta t \cdot \mathrm{freq}}{2\pi}\right) \tag{A.2}$$

and θ is the lag phase angle, Δt is the time difference between the peaks of the two waveforms, and freq is the alternating voltage frequency. For the current study it was determined that the power factor was 0.995 indicating the circuit could be analyzed as purely resistive because true power in an alternating current circuit is defined as:

$$\mathrm{power} = \mathrm{voltage} \cdot \mathrm{current} \cdot \mathrm{PF} \qquad [A.3]$$

A calibration of the pre-heater performance was accomplished by monitoring the applied electrical power defined by equation A.2, and comparing it to the required power to heat the fluid in liquid phase. The pre-heater inlet and outlet temperatures were monitored as well as the mass flow rate. The required thermal power from the pre-heater can be calculated by:

$$\dot{Q}_{\mathrm{fluid}} = \dot{m}\, c_p (T_{\mathrm{outlet}} - T_{\mathrm{inlet}}) \qquad [A.4]$$

The efficiency of the preheater, φ, can be defined as:

$$\varphi = \frac{\dot{Q}_{\mathrm{fluid}}}{\dot{Q}_{\mathrm{elec}}} = \frac{\dot{m}\, c_p (T_{\mathrm{outlet}} - T_{\mathrm{inlet}})}{V \cdot I \cdot PF} \qquad [A.5]$$

Figure A1.7 shows a plot of the pre-heater efficiency verses surface temperature for the un-insulated and insulated pre-heater. Adding plastic pipe insulating to the pre-heater surface increased the efficiency to approximately 95%, but a slight downward trend with surface temperature was seen due to higher losses to ambient from natural convection. The pre-heater efficiency was not important for sub-cooled inlet conditions to the test section, because power was controlled based on pre-heater outlet temperature. For data collect where the test section has an inlet quality greater than zero, the pre-heater efficiency was used to calculate the exact inlet conditions to the test section.

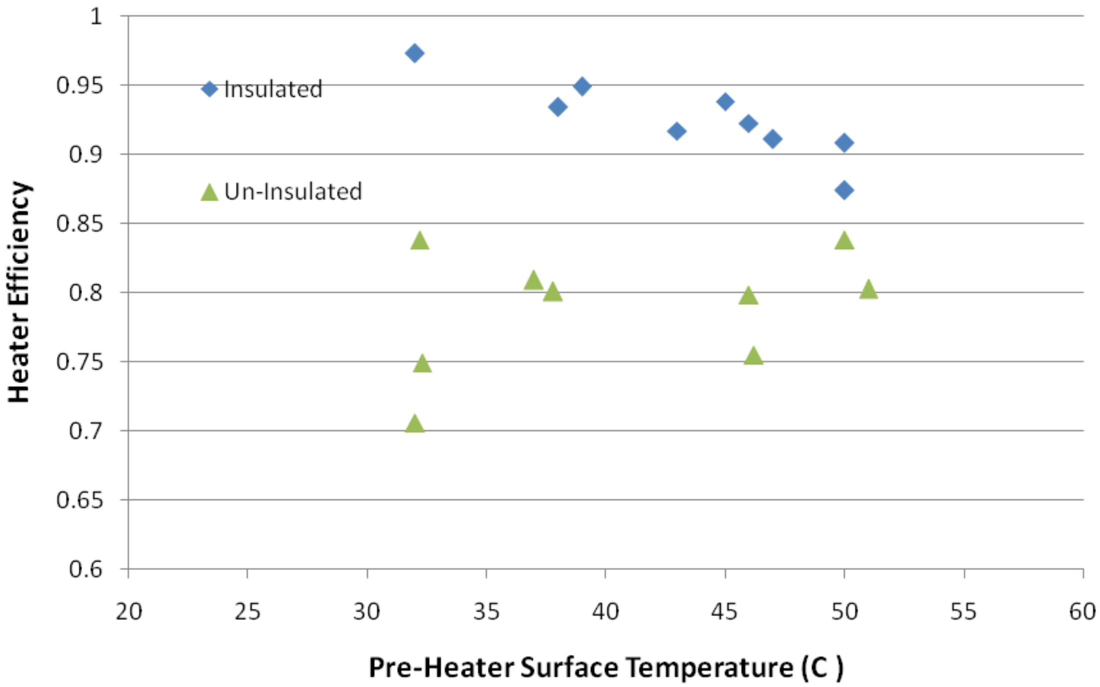

Figure A1.6: Pre-Heater Thermal Efficiency

# Appendix 2: Analysis Algorithm Code

Matlab was used to perform the analysis algorithm detailed in Section 3 as well as to plot the various outputs. Several different functions were created to perform separate steps in the analysis with a Matlab script calling each function in correct order.

## A2.1: Overall Program Flow

Overall analysis program flow can be represented by the block diagram in Figure A2.1. The individual functions called at each point in the program are noted in Figure A2.1 and detailed in the A.2.2 through A2.9.

For the *analysis_script.m* to work properly, each of the Matlab script files listed in Figure A2.1 must be in the working directory along with a *.asc* and *.ptw* file for each data run that is to be analyzed. Typically 20-30 sets of files were analyzed per batch, with each file set representing set of steady state conditions. The *.asc* file was a tab delimitated Altair output file representing the raw temperature readings over the opaque section of the silicon tube at each captured video frame. The *.ptw* file was a binary Altair output file representing the image intensity over the visualization portion of the silicon test section at each captured video frame. The *.ptw* file also included camera information, resolution and time step data.

The *analysis_script.m* program first determined all of the Altair files in the working directory, then loaded each set of files using *ascloader.m* and *ptwloader.m* and saved the data in Matlab file formats. Next the analysis algorithm was run for each set of files using *tubecond.m*. The final saved outputs include visualization video frames

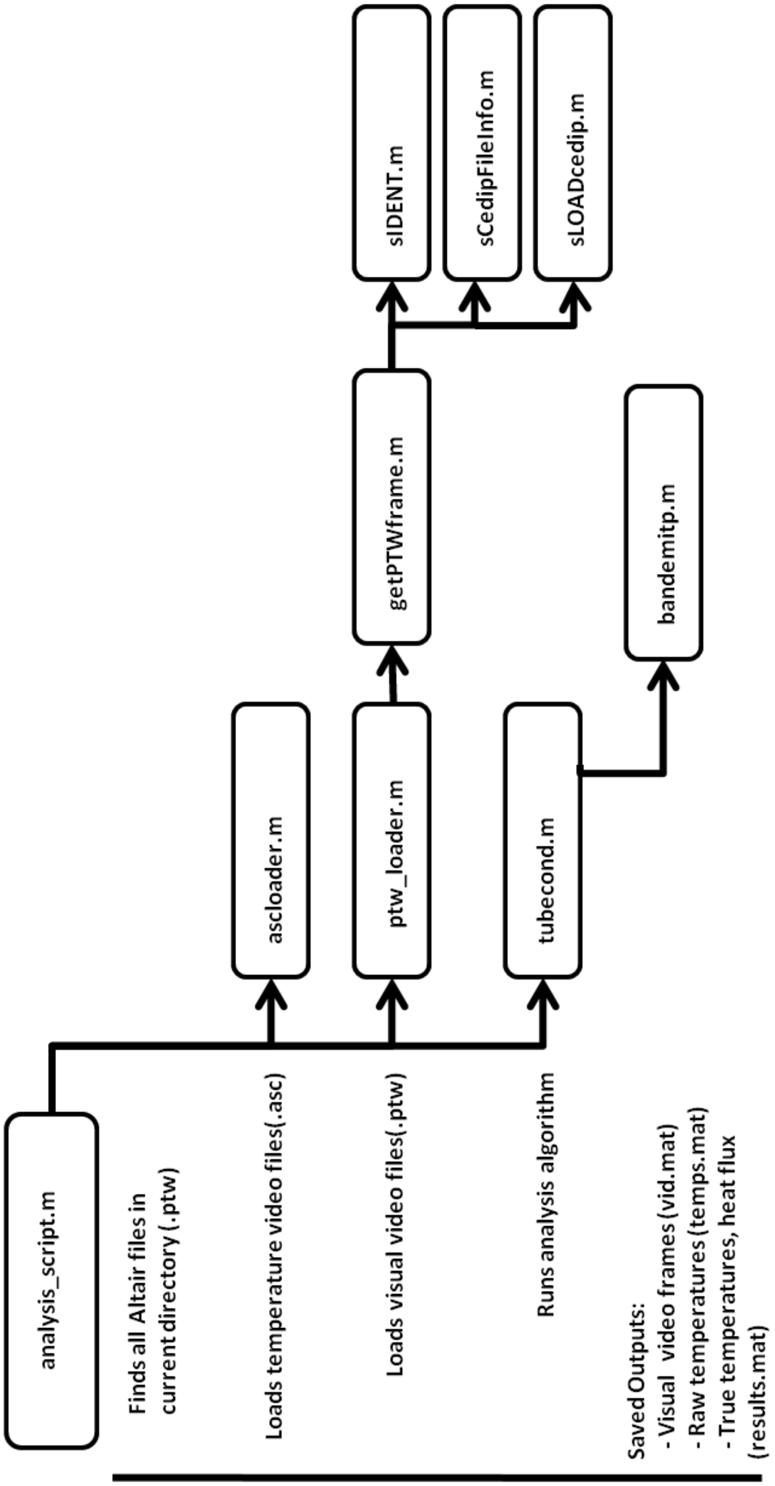

**Figure A2.1: Computer Algorithm Functional Diagram**

(*vid_xx.mat*), raw camera temperatures (*temps_xx.mat*), and true temperatures, heat fluxes, and times (*results_xx.mat*). Plotting routines were then used to display the results, time average the results, and calculate other heat transfer variables such as heat transfer coefficient and bulk fluid quality.

## A2.2: Analysis Script

Code for the overall analysis script is presented below. Required inputs were at least 1 set of Altair output files, as well as all of the associated children functions. The Altair output files were consistently named such that for the first pair the visualization file is *01.ptw* and the opaque file is *01.asc*. The script analyzed each pair of files located in the directory in ascending order.

```
function analysis_script()
clear all
%determin all .asc and .ptw files in current directory
file_asc=dir('*.asc');
file_ptw=dir('*.ptw');

%a and c are number of files in directory
[a b]=size(file_asc);
[c d]=size(file_ptw);

if a~=c
    %.ptw and .asc files must be of same number
    disp('ERROR - Number of .ptw and .asc files does not match')
end

for i=1:a
    filein=file_asc(i,1).name
    [e f]=size(filein);
    suffix=filein(1:f-4);
    fileout=['temps_' suffix];
    %run ascii loader
    [numframes]=ascloader(filein, fileout);
    clear filein fileout
    %run ptwloader
    filein=file_ptw(i,1).name
```

```
    [e f]=size(filein);
    suffix=filein(1:f-4);
    fileout=['vid_' suffix];
    [vid res]=ptwloader(filein,numframes,fileout);
    clear vid res numframes
end

disp('All .asc and .ptw files loaded and saved as .mat files')
beep
beep
disp('Starting analysis algorythm')

for i=1:a
    filein=file_asc(i,1).name
    [e f]=size(filein);ana
    suffix=filein(1:f-4);
    filein=['temps_' suffix];
    fileout=['results_' suffix];

    %run tubecond.m to perform analysis algorithm
    [ttemp tblack qflux]=tubecond(filein, fileout);
    clear ttemp tblack qflux filein fileout
end
```

## A2.3: Opaque  Video File Loader Function (ascloader.m)

This function opened a tab deliminated (*.asc*) file and loaded the temperature data for each frame while deleting the frame information header.  After the temperature data had been loaded, the inside and outside temperature profiles along the tube were found by only selecting the relevant pixles.  All of the data was loaded using low level file functions such as *fgets*, and *sscanf*.  The function output was a saved Matlab data file (*temps_xx.mat*) with the inside and outside temperature profiles.

```
function [frames]=ascloader(filein, fileout)
%Loads the temperature data stored in a tab delimitated .asc
%file, then the inside and outside tube temperatures are determined
%based on defined lines relative to the video frame

ts=1
```

```
te=2
fid = fopen(filein)
clear i res a t row vid
%scan the file header and save information needed
for i=1:27
    a=fgets(fid);
    if i==6
        res=sscanf(a,'%*s %d %d');
    end
    if i==4
        date=a;
    end
end

for j=1:ts-1
%loop moves down one frame
for i=1:(1+1+res(2)+3)
    a=fgets(fid);
end
end
%start scanning each frame
t=1;
while ~feof(fid)

    clear vid_inst
    row=1;
    a=fgets(fid);
    time(t,1)=t;
    %added by alex-2012
     if length(a) == 5
        times = sscanf(fgets(fid),'%12c');
    else
        check = sscanf(fgets(fid), '%12c');    % collects time for each
frame
        if length(check) == 18
            times = sscanf(check, '%*4s %12c');
        elseif length(check) == 14
            times = sscanf(check, '%12c');
        end
    end

 if length(times) == 12
        time(t,2) = sscanf(times,'%2d'); %records hours
        time(t,3)=sscanf(times,'%*3s %2d'); %records minutes
        time(t,4)=sscanf(times,'%*6s %2d'); %records seconds
        time(t,5)=sscanf(times,'%*9s %3d'); %records milliseconds

time(t,6)=(time(t,2)/24)+(time(t,3)/1440)+(time(t,4)/86400)+(time(t,5)/
(1000*86400));   % converts all times to days
    elseif length(times) == 14
        time(t,2) = sscanf(times,'%2d'); %records hours
        time(t,3)=sscanf(times,'%*3s %2d'); %records minutes
        time(t,4)=sscanf(times,'%*6s %2d'); %records seconds
        time(t,5)=sscanf(times,'%*9s %3d'); %records milliseconds
```

```
time(t,6)=(time(t,2)/24)+(time(t,3)/1440)+(time(t,4)/86400)+(time(t,5)/
(1000*86400));   % converts all times to days
    elseif length(times) == 16
        time(t,2) = sscanf(times,'%*3s %2d'); %records hours
        time(t,3)=sscanf(times,'%*3s %*3s %2d'); %records minutes
        time(t,4)=sscanf(times,'%*3s %*6s %2d'); %records seconds
        time(t,5)=sscanf(times,'%*3s %*9s %3d'); %records milliseconds

time(t,6)=(time(t,2)/24)+(time(t,3)/1440)+(time(t,4)/86400)+(time(t,5)/
(1000*86400));   % converts all times to days
 end
 %END ALEX CODE

    while row<res(2)+1
        vid_inst(row,:,1)=((sscanf(fgets(fid),'%f')));
        row=row+1;
    end
    %moves pointer 3 rows down to next frame start
     for i=1:3
         a=fgets(fid);
     end
     %Finds temp profiles at each frame
     [im jm c]=size(vid_inst);
    for j=1:jm
        Tout(j,t)=vid_inst((fix((-0/520)*(j-1))+6),j,1);
        Tin(j,t)=vid_inst((fix((-0/520)*(j-1))+16),j,1);

    end
     t=t+1
end
frames=t-2;

display('ASCII text tile loaded into vid matrix')
save(fileout, 'Tin', 'Tout','time')
fclose(fid);
```

## A2.4: Visual  Video File Loader Function (ptwloader.m)

This function opened an ALTAIR binary output file (*.ptw*) and converts the data to video frames for visualization of the flow.  The file saved contains relative intensities, not actual temperatures from the camera, where the intensity is an integer in the range of 0 - 1,6384.

```
function [vid res]=ptwloader(filein,t,fileout)
%Reads ALTIAR binary output file and saves visual data
%as a MATLAB data file,  saved data is in relative intensity
```

```
%not actual temperatures

filename=filein;

[data, fileinfo,timet] = GetPTWFrame (filename,1);
w=fileinfo.m_cols;
h=fileinfo.m_rows;
res=[h w];

vid=zeros(h,w,t,'uint16');
vtime=zeros(t,4);
time=zeros(t,6);

for i=1:t
    [data, fileinfo,timet] = GetPTWFrame (filename,i);
    vid(:,:,i)=data(:,:);
    vtime(i,:)=timet;
    time(i,1)=i;
    time(i,2)=vtime(i,1);
    time(i,3)=vtime(i,2);
    time(i,4)=vtime(i,3);
    time(i,5)=vtime(i,4);

time(i,6)=(time(i,2)/24)+(time(i,3)/1440)+(time(i,4)/86400)+(time(i,5)/
(1000*86400));
    i=i
end
save(fileout, 'vid')
```

## A2.5: Implicit Finite Difference Solver Function (tubecond.m)

This function performed the analysis algorithm on the given input file name which must specify a set of temperature profiles (*temps_xx.mat*). Also required was a Matlab data file (*Tinfpoly_xx.mat*) that contained the tube temperature at infinity based on the zero heat flux calibration data. Outputs of this function were the true inside and outside tube temperature and heat flux.

```
function [ttemp tblack qflux]=tubecond(filein, fileout)
%function calculates true temp and heat flux on Si tube using
%temp profiles Tin and Tout
%Uses bandemitp() for faster calcs
%updated 11 AUG 11 at southwest airplane
%updated 14 aug, removed eint==0 relaced with clear eint
```

```
%updated 19 AUG --> variable dt allowed based on Time vector
%updated 28 SEP -->fix on improper formation of matrix 'C'
tic

%load the required input file (temps.mat)
load(filein)
%load the Tinf polynomial fit file
load Tinfpoly_11

stime=cputime; %used for computational time calc
%CONSTANTS
ksi=148
ka=0.2
kkap=0.12
rhosi=2330
rhoa=1
rhok=1
cpsi=712
cpa=1395
cpk=1547
%thickness of layers
dsi=.001
da=.000015
dk=.000015
sig=.0000000567
%emissivity of black surface
em=0.896
%absoptivity
abssi=8
absk=7110
%reflection constants
emsi=0.846545;
emka=0.6661;
tr=0.444812;
ref=.427243;
ct_out=0.616
ct_in=0.900
ct_out=1
ct_in=1
i=1

[im km]=size(Tin);
[imm kmm]=size(Tout);
%checks that inside and outside temps have same size
if im~=imm
    disp('matrix size mismatch')
end
if km~=kmm
    disp('matrix size mismatch')
end
im=578
%initialize temperature and heat flux output matrices to speed calc
ttemp=zeros(im,km);
qflux=zeros(im,km);
```

```
Tinf=20  %Tinf is set to a constant value only for calculating outside
temp

%calculate T black for all times (this is the outside tube temp)
for kk=1:km
        for ii=1:im
        [Ecam asd]=bandemitp(Tout(ii,kk),3.7,4.8);
        [Einf asd]=bandemitp(Tinf,3.7,4.8);
        err=1;
        Tg=Tout(ii,kk);
            %iterate to find Tblack
            while err>0.0001
            [emgu fg]=bandemitp(Tg,3.7,4.8);
            Tbb=((Ecam-(1-
(ct_out*em))*Einf)/(em*ct_out*fg*sig))^(0.25)-273.16;
            err=abs(Tbb-Tg);
            Tg=Tg+((Tbb-Tg)/2);
            end
        tblack(ii,kk)=Tbb;
        end
     kk=kk
end
toc

%number of nodes in each region (a,b,c)
nodea=20;
dxa=dsi/(nodea-0.5);
nodeb=20;
dxb=da/(nodeb);
nodec=20;
dxc=dk/(nodec-0.5);
nm=nodea+nodeb+nodec;

for ii=1:im  %loop for pixels
cptime=cputime; %cpu time for each pix

C(1:nm-2,1)=tblack(ii,1);%initialize all temps in all nodes to black
temp
%this is the initial condition for the implicit method

kk=1;
%TIME Loop
for kk=2:km
%calculate the time step based on Altair time data
dt=(time(kk,6)-time(kk-1,6))*24*3600;

%creates Matrix A in sparse form
A=sparse(nm-2,nm-2);
%insert proper values into matrix A for the finite difference problem
%each region has different thermo properties, and grid spacing
%region A matrix half (silicon layer)
Fosi=ksi*dt/(rhosi*cpsi*dxa*dxa);
for i=1:nodea-1
    for j=1:nodea
        if j==i
            A(i,j)=2*Fosi+1;
```

```
        end
        if j==i+1
            A(i,j)=-Fosi;
        end
        if j==i-1
            A(i,j)=-Fosi;
        end
    end
end
%node area b (adhesive layer)
Foa=ka*dt/(rhoa*cpa*dxb*dxb);
for i=nodea:nodea+nodeb-1
    for j=nodea-1:nodea+nodeb
        if j==i
            A(i,j)=2*Foa+1;
        end
        if j==i+1
            A(i,j)=-Foa;
        end
        if j==i-1
            A(i,j)=-Foa;
        end
    end
end
%node area c (kapton layer)
Fok=kkap*dt/(rhok*cpk*dxc*dxc);
for i=nodeb+nodea:nodea+nodeb+nodec-2
    for j=nodeb+nodea-1:nodea+nodeb+nodec-2
        if j==i
            A(i,j)=2*Fok+1;
        end
        if j==i+1
            A(i,j)=-Fok;
        end
        if j==i-1
            A(i,j)=-Fok;
        end
    end
end
%find the emmision due to the raw inside tube temp
[Ecam fgh]=bandemitp(Tin(ii,kk),3.7,4.8);
%Calcs Esi by integrating of length
clear eint
for n=2:nodea
    [emmis fgh]=bandemitp(C(n),3.7,4.8);
    eint(n)=emmis*abssi*exp(-abssi*(dxa*(n-1)))*dxa;
end
Esi=emsi*sum(eint);
%Calcs Ekap by integrating of length
clear eint
for n=nodea+1:nodea+nodeb
    [emmis fgh]=bandemitp(C(n),3.7,4.8);
    eint(n)=emmis*absk*exp(-absk*(dxb*(n-(nodea+.5))))*dxb;
end
Ekap=sum(eint);

%Calcs Ead by integrating of length
```

```
clear eint
for n=nodea+nodeb+1:nodea+nodeb+nodec-2
    [emmis fgh]=bandemitp(C(n),3.7,4.8);
    eint(n)=emmis*absk*exp(-absk*(dxc*(n-(nodeb+nodea+.5))))*dxc;
end
Ead=sum(eint);
Ekap=emka*(Ekap+Ead);
%Einf due to surroundings or based on Tinf_eff
 pinf=Tinfpoly(ii,:);
 Tinf=polyval(pinf,Tin(ii,kk));
Tinflist(ii,kk)=Tinf;
%this finds Tinf_eff by 3rd order approx of Tinfpoly
[emmis fgh]=bandemitp(Tinf,3.7,4.8);
Einf=emmis*ref;  %calcs Tinf based on reflection and set temp or...

Ebb=(Ecam-(Esi+Ekap+Einf))/(tr);

Tg=Tin(ii,kk);
err=1;
%interate to find Tin
    while err>0.0001
        [emgu fg]=bandemitp(Tg,3.7,4.8);
        Tbb=((Ebb/(em*sig*fg))^0.25)-273.16;

        err=abs(Tbb-Tg);
        Tg=Tg+((Tbb-Tg)/2);
    end

ttemp(ii,kk)=Tg; %stores true temp as updated Td (guess temp)

%sets constant temp BC
    C(1,1)=C(1,1)+Fosi*tblack(ii,kk);
    C(nm-2,1)=C(nm-2,1)+Fok*Tg;
B=(A^-1)*C;
C(:,1)=B(:,1);

qflux(ii,kk)=(C(nm-3,1)-C(nm-2))*kkap/dxc;

end %end of time loop
display(['Pixel number = ',num2str(ii)])
display(['time for last pixel (sec) = ',num2str(cputime-cptime)])
display(['time remaining (min) = ',num2str((cputime-cptime)*(im-
ii)/60)])

end

save(fileout, 'ttemp', 'qflux', 'tblack', 'time')
```

## A2.6: Band Emission Calculator (bandemitp.m)

This function calculated the energy emitted by a blackbody between two wavelengths according to Plank's law, Equation 3.1. Also calculated was the band emission factor, F, as defined by Equation 3.5. Because this function was called many thousands of times per time step by *tubecond.m*, it was desirable to minimize calculation time. Instead of performing the integral in Equation 3.5, a 5th order polynomial curve fit was performed over a limited range of temperatures and wavelengths. Maximum error between 20 and 90 °C and wavelengths of 3.7 to 4.8 microns was 6.0 x $10^{-4}$ %.

```
function [emmis f]=bandemitp(temp,landa1,landa2)

%function outputs emissivity and f based on a 5th order poly fit
%with fixed wavelengths of 3.7-4.8 um
%percent error from 20 - 90 C
% emission = 6e-4%
%f = 1.5e-4%

emmis=(-2.890517590241547e-11)*(temp^5)+(6.63142754616159e-
08)*(temp^4)+(9.65947365252665e-06)*(temp^3)+...

(0.001116090524310)*(temp^2)+(0.058629890499758)*(temp)+(1.349518805919
918);

f=(2.421174742299602e-14)*(temp^5)+(-2.670957576854183e-
11)*(temp^4)+(4.361802367261018e-09)*(temp^3)+...
    (1.255361781172065e-06)*(temp^2)+(1.251360688247466e-
04)*(temp)+(0.004262326991903);
```

# A2.7: sCedipFileInfo.m

This function was supplied by Altair and is required by *ptwloader.m* when converting binary output files.

```
function s = sCedipFileInfo(s)
% SEQUENCE :: SCEDIPFILEINFO
% Copyright (c) Alexander Dillenz 2000-2001
%
% for documentation see manuelrf.doc
```

```
fid=fopen(s.m_filename,'r');
if fid==-1
    error('fileopen');
end; %if

fseek(fid, 11, 'bof');
s.m_MainHeaderSize=fread(fid,1,'int32');
s.m_FrameHeaderSize=fread(fid,1,'int32');
fseek(fid, 27, 'bof');
s.m_nframes=fread(fid,1,'int32');
fseek(fid, 245, 'bof');
s.m_minlut=fread(fid,1,'int16');
s.m_maxlut=fread(fid,1,'int16');
if(s.m_maxlut==-1)
    s.m_maxlut=2^16-1;
end; %if
fseek(fid, 277, 'bof');
s.m_specialscale=fread(fid,1,'uint16'); % Special scale (Echelle
Speciale)
scaleunit='';
scaleunit=fread(fid,10,'char');
s.m_scalevalue=fread(fid,17,'float');
if(s.m_specialscale==0)
    s.m_unit='dl';                           % [dl T rad]
else
    s.m_unit=scaleunit;                      % [dl T rad]
end; %if

fseek(fid, 377, 'bof');
s.m_cols=fread(fid,1,'uint16'); % Columns
s.m_rows=fread(fid,1,'uint16'); % Rows
if s.m_rows==0
   s.m_rows=128;
end;%if
if s.m_cols==0
   s.m_cols=128;
end;%if
s.m_bitres=fread(fid,1,'uint16'); % bit resolution
fseek(fid, 403, 'bof');
s.m_frameperiode = fread(fid,1,'float'); % frame rate
s.m_integration =  fread(fid,1,'float'); % integration time

fseek(fid, 563, 'bof');
s.m_comment=fread(fid,1000,'char');

fseek(fid, 1563, 'bof');
s.m_calibration=fread(fid,100,'char'); % calibration file name

fseek(fid,s.m_MainHeaderSize,'bof'); %skip main header
fseek(fid,s.m_FrameHeaderSize,'cof'); %skip frame header
firstline = fread(fid, [s.m_cols, 1], 'uint16'); %read one line
% look if first line contains lockin information
if(firstline(1:4)==[1220,3907,1204,2382]')
    s.m_cedip_lockin=1;
    s.m_rows=s.m_rows-1;
```

```
else
    s.m_cedip_lockin=0;
end; %if
s.m_framepointer=1;
s.m_firstframe=1;
s.m_cliprect=[0 0 s.m_cols-1 s.m_rows-1];
s.m_lastframe=s.m_nframes;
s.m_FrameSize = s.m_FrameHeaderSize + s.m_cols * s.m_rows * 2;

fclose(fid); %close file
clear fid firstline scaleunit;
return;
```

## A2.8: sIndent.m

This function was supplied by Altair and is required by *ptwloader.m* when converting binary output files.

```
% SEQUENCE :: SIDENT
% identify sequence file
%
%   Copyright (c) Alexander Dillenz 2000-2001

function s = sident(s)

if (isempty(s.m_filename))
    error('file not assigned');
end; %if
fid=fopen(s.m_filename,'r');
info=fread(fid,11,'int8'); %skip the first 11 bytes
fclose(fid); %close file

switch(char(info(1:3))')
case 'AIO' %AGEMA
    s.m_format='agema';

case 'CED'
    s.m_format='cedip';
    s.m_unit='dl';
    s = sCedipFileInfo(s);

otherwise
    s.m_format='unknown';

end; %switch
return;
```

## A2.9: sLoadCedip.m

This function was supplied by Altair and is required by *ptwloader.m* when converting binary output files.

```
function [s time] = sLoadCedip(s)
% SEQUENCE :: SLOADCEDIP
% loadcedip reads a Cedip-PTW file into matrix result
%   Copyright (c) Alexander Dillenz 2000-2001
% for documentation see manuelrf.doc

% check filename
if (isempty(s.m_filename))
    error('file not assigned');
end; %if

% open file
fid=fopen(s.m_filename,'r');
if fid==-1
    error('file open');
end; %if

% skip main header
fseek (fid, s.m_MainHeaderSize,'bof');

if(s.m_cedip_lockin) % lockin -> skip first line
   fseek (fid, (s.m_framepointer-1) * (s.m_FrameSize + 2*s.m_cols),
'cof');
else
   fseek (fid, (s.m_framepointer-1) * (s.m_FrameSize), 'cof');
end; %if

%fseek(fid,s.m_FrameHeaderSize,'cof'); %skip frame header

timedata = fread(fid,s.m_FrameHeaderSize,'uint8');%read time frame
header
time(1)=timedata(82);
time(2)=timedata(81);
time(3)=timedata(84);
time(4)=(timedata(83)*10)+timedata(161);

s.m_data = fread(fid, [s.m_cols, s.m_rows],'uint16'); %read one frame
% if a special scale is given then transform the data
if(s.m_specialscale)
    low = min(s.m_scalevalue);
    high = max(s.m_scalevalue);
    s.m_data = s.m_data .* (high-low)./ 2^16 + low;
    clear low high;
end; %if
```

```
if(s.m_cedip_lockin) % lockin -> skip first line
    s.m_cliprect = [0 1 s.m_cols-1 s.m_rows];
end; %if
s.m_minval = min(min(s.m_data(1:s.m_cols,2:s.m_rows)));
s.m_maxval = max(max(s.m_data(1:s.m_cols,2:s.m_rows)));
fclose(fid); %close file
return;
```

# 9. References

[1] Hewitt, G. F. “Pheomenological Issues in Forced Convective Boiling.” Proceedings of Convective Flow Boiling. 1995.

[2] Bergles, A.E., Rohsenow, W.M. “Forced-Convection Surface-Boiling Heat Transfer and Burnout in Tubes of Small Diameter.” Technical Report for Massachusetts Institute of Technology. 1962.

[3] Jens, W.H., Lottes, P.A. “Analysis of Heat Transfer, Burnout, Pressure Drop and Density Data for High Pressure Water.” Argonne National Laboratory Technical Report. 1951.

[4] Sato, T., Matsumura, H. “On the Conditions of Incipient Subcooled-Boiling with Forced Convection.”Buliletin of JSME. 1964.

[5] Kandlikar, S.G. “Heat Transfer Characteristics in Partial Boiling, Fully Developed Boiling, and Significant Void Flow Regions of Subcooled Flow Boiling.” Journal of Heat Transfer.Vol 120, pp 395. 1998.

[6] Butterworth, D., Hewitt, G.F. “Two-Phase Flow and Heat Transfer.”Oxford Univ Press. New York. 1977.

[7] Thom, R.S. “Boiling in sub-cooled water during flow up heated tubes or annuli.”Proceedings Institiute of Mechanical Engineering, Vol 226, pp180. 1965.

[8] Cheng, S.C., Ng, W.W.L., Heng, K.T. “Measurements of Boiling Curves of Subcooled Water Under Forced Convective Conditions.” International Journal of Heat and Mass Transfer.Vol 21, pp. 1385-1392. 1978.

[9] Kandlikar, S.G. “A General Correlation for Saturated Two-Phase Flow Boiling Heat Transfer Inside Horizontal and Vertical Tubes.” Journal of Heat Transfer, Vol 112, [[ 219. 1990.

[10] Zhang, H., Mudawar, I., Hasan, M. (2007) “Assesment of dimensionless CHF correlations for subcooled flow boiling in microgravity and Earth gravity.” International Journal of Heat and Mass Transfer, Vol 50, pp. 4568-4580

[11] Zhang, H., Mudawar, I., Hasan, M. “Investigation of Interfacial Behavior during the flow Boiling CHF Transient.” International Journal of Heat and Mass Transfer, Vol 47, pp. 1275-1288. 2004.

[12] Zhang, H., Mudawar, I., Hasan, M. “Flow Boiling CHF in mircrogravity.” International Journal of Heat and Mass Transfer, Vol 48, pp. 3107-3118. 2005.

[13] Bowers, B.M., Mudawar, I. “High flux boiling in low flow rate, low pressure drop mini-channel and micro-channel heat sinks.” International Journal of Heat and Mass Transfer, Vol 37, pp. 321-332. 1994.

[14] Theofanous, T.G., et al. "Quantitative radiography for transient multidimensional, multiphase flows." Nuclear Engineering and Design, Vol 184, pp. 163-181. 1998.

[15] Takenaka, N. et al. "Three-dimensinoal visualization of void fraction distribution in steady two-phase flow by thermal neutron radiography." Nuclear Engineering and Design. Vol 184, pp 203-212. 1998.

[16] Kureta, M., et al. "Study on point of net vapor generation by neutron radiography in subcooled boiling flow along narrow rectangular channels with short heated length." International Journal of Heat and Mass Transfer, Vol 46, pp. 1171-1181. 2003.

[17] Hibiki, T., Situ, R., Mi, Y., Ishii, M. "Local flow measurements of vertical upward bubbly flow in an annulus." International Journal of Heat and Mass Transfer, Vol 46, pp. 1479-1496. 2003.

[18] Muwanga, R., and Hassan. I. "A flow boiling heat transfer investigation of FC-72 in a mircrotube using liquid crystal thermography." Journal of Heat Transfer. Vol 129, pp 977-987. 2007.

[19] Thome, J.R., Dupont, V., Jacobi, A.M. "Heat transfer model for evaporation in microchannels. Part I: presentation of the model." International Journal of Heat and Mass Transfer, Vol 47, pp. 3375-3385. 2004.

[20] Di Marzo, M., et al. "Evaporative cooling due to a gently deposited droplet." International Journal of Heat and Mass Transfer, Vol 36, pp. 4133-4139. 1993.

[21] Saito M., et al. “Boiling Two-Phase Flow Under Mircrogravity.” Nuclear Engineering and Design.Vol 146, pp451-461. 1994.

[22] Kim, J., Benton. “Highly subcooled Pool Boiling Heat Transfer at Various Gravity Levels.” International Journal of Heat and Mass Transfer, Vol 23, pp. 497-508. 2002.

[23] Ohta, H., Kawaji, M., Azuma, H., Kakehi, K., and Morita, T. S., 1998, “Heat transfer in nucleate pool boiling under microgravity condition,” Journal of Heat Transfer, Vol 2, pp. 401-406. 1998

[24] Raj, R., Kim, J. McQuillen, J. “Subcooled Pool Boiling in Variable Gravity Environments.”Journal of Heat Transfer.Vol 131. 2009

[25] Raj, R., Kim, J. McQuillen, J. “Gravity Scaling Parameter for Pool Boiling Heat Transfer.”Journal of Heat Transfer.Vol 132. 2010

[26] T.G. Theofanous, J.P. Tu, A.T. Dinh and T.N. Dinh, “The Boiling Crisis Phenomenon.” J. Experimental Thermal Fluid Science, Vol 26, pp 775-810. 2002.

[27] Gerardi, C. et al. “Study of bubble growth in Water Pool Boiling Through Synchronized, Infrared Thermometry and High Speed Video.” International Journal of Heat and Mass Transfer, Vol 53, pp. 4185-4192. 2010.

[28] Stephan, P., Schweizer, N.. "Experimental study of bubble behavior and local heat flux in pool boiling under variable gravitational conditions." Mulitphase Science and Technology, Vol 21, pp. 329-350. 2009.

[29] Carey, V.P. “Liquid Vapor Phase-Change Phenomena.” Taylor and Francis. 1992.

[30] Hsu, Y.Y., “On the size range of Active Nucleation Cavities on a heating surface.” Journal of Heat Transfer.Vol 84, pp. 207-216. 1962.

[31] Quinn, T.J. (1967) “Thermal radiation from partially transparent reflecting bodies.” Journal of the Optical Society of America, Vol. 40, No 6, pp. 376-380.

[32] Handbook of Chemistry and Physics. David R. Lide, editor. 87th Edition. 2006.

[33] DuPont Kapton HN Technical Data Sheet. DuPont High Performance Films, Inc. 2011.

[34] Lee, J., Kim, J., Kiger, K.T. “Time and space-resolved heat transfer characteristics of single droplet cooling using microscale heater arrays.” International Journal of Heat and Mass Transfer, Vol22, pp. 188-200. 2001.

[25] Bejan, Adrian.“Convection Heat Transfer” John Wiley and Sons, New York, 1995.

[26] Kays, William, Crawford, Michael, Weigand, Bernhard. “Convective Heat and Mass Transfer” Fourth Edition, McGraw Hill, New York, 2005

[37] Graetz, L. “On the thermal conductivity of liquids.” Part 1. Ann. Phys. Chem., Vol 18, 1883. Pp. 79-94. Part 2, Ann. Phys. Chem., Vol 25, 1885, pp 337-357.

[38] Sellers, J., Tribus, M., Klein, J.S., “Heat Transfer to Laminar FLow in a Round Tube or Flat Conduit: The Graetz Problem Extended.” Trans. ASME. 1956. Vol 78, pp 441-448.

[39] Ito, H. "Pressure Losses in Smooth Pipe Bends." Journal of Basic Engineering. March, 1960. pp 131-141.

[40] Raj, R. "Nucleate pool boiling heat transfer: parametric effects of gravity, heater size and dissolved gas." PhD dissertation Proposal, University of Maryland. 2009.

[41] Lazarek, G.M., Black, S.H. "Evaporative Heat Transfer, Pressure Drop and Critical Heat Flux in a Small Vertical Tube with R-113." International Journal of Heat and Mass Transfer, 1982. Vol 25, pp 945-960.

[42] Chen, J.C. "Correlation for Boiling Heat Transfer to Saturated Fluids in Convective Flow." Industrial Engineering Chemical Process Design and Delivery. 1966. Vol 5, pp 322-329.

[43] Gungor, K.E. and Winterton, R.H.S. "A General Correlation for Flow Boiling in Tubes and Annuli." International Journal of Heat and Mass Transfer, 1986. Vol 29, pp 351-358.

[44] Shah, M.M. "Chart Correlation for Saturated Boiling Heat Transfer: Equations and Further Study." ASHRAE Transactions, 1982. Vol 88, pp 185-196.